2018

TERRESTRIAL PLANET SERPENTINIZATION IN MELANGE SETTINGS

Roger Hart
University of Rhode Island, Rmhart2014@gmail.com

TERRESTRIAL PLANET SERPENTINIZATION IN MELANGE SETTINGS

BY

ROGER M. HART

A THESIS SUBMITTED IN PARTIAL FULFILLMENT OF THE

REQUIREMENTS FOR THE DEGREE OF

MASTER OF SCIENCE

DEPARTMENT OF GEOSCIENCES

UNIVERSITY OF RHODE ISLAND

2018

MASTER OF SCIENCE THESIS

OF

ROGER M. HART

APPROVED:

Thesis Committee:

Major Professor Dawn Cardace

Mark Stolt

Ying Zhang

Nasser H. Zawia
DEAN OF THE GRADUATE SCHOOL

UNIVERSITY OF RHODE ISLAND

2018

ABSTRACT

Mars and Earth have planetary crusts with exposures of mantle-derived ultramafic rocks dominated by pyroxene and olivine. These initial minerals transform to serpentine, brucite, magnetite, and other secondary phases via metamorphic hydration and other reactions. In this work, altered peridotites of the regionally extensive Coast Range Ophiolite (CRO), from localities in the UC-Davis McLaughlin Natural Reserve, Lower Lake, CA are compared and contrasted with serpentinites of the Nili Fossae, a mélange terrain located in the Syrtis Major quadrangle at approximately 22°N, 75°E, Mars. The habitability of serpentinizing systems is conveyed as a function of changing system parameters (such as temperature, Eh, pH, and activities of aqueous geochemical species), and provides insight into the biological prospects of serpentinization in mélange terrains in a general sense. Petrography of the serpentinized Jurassic age ultramafic unit in the Coast Range Ophiolite confirms the dominance of secondary phases (serpentine, other clays, carbonates, magnetite) and presence of relict primary minerals (olivine and pyroxene). Major element concentrations for crystals of olivine (from McL-239A and McL-329), show concentrations of MgO (avg: 48.9 wt%), SiO_2 (avg: 40.8 wt%) and high FeO (avg: 10.2 wt%) that are high relative to San Carlos, Olivine (standard). Backscatter electron images (BSE) of such crystals in McL-239A and McL-329 show relict olivine surrounded by a serpentine-rich matrix. The crystal chemistry of these representative samples of olivine from the CRO serve as an analog for the olivine-rich protolith that underwent serpentinization observed in the Nili Fossae.

Using CRO data to construct a model protolith reasonable for ultramafics of the Nili Fossae mélange (constrained by CRISM observations), I deduce evolving habitability as the model protolith reacts with feasible, co-occurring fluid chemistries. Major aqueous geochemical compositions are based on based on postulated planetary analog waters that are largely Na-Cl, Mg-Cl, or Ca-Cl solutions. The modeled water-rock reactions were performed at conditions associated with both CRO and the Nili Fossae mélange settings. Habitability was assessed using a Gibbs Free Energy minimization strategy, for serpentinization-driven methanogenesis (MG) and methanotrophy (MT). I show that the bioenergetic yields of fundamental methanogenetic and methanotrophic reactions progress favorably between -120 kJ/mol to a maximum of -400 kJ/mol as serpentinization progresses under different groundwater/hydrothermal conditions in mélange terrains.

ACKNOWLEDGMENTS

First and foremost, if it wasn't for my advisor, mentor, and professional role model, Dr. Dawn Cardace, I could not have finished my thesis if I didn't have her help. Without her understanding, dedication, and patience this thesis would have not been possible. She has guided me through the academic process, from initially applying to helping polish up this thesis draft. Thank you, Dawn, for everything! Without the support and flexibility of my thesis committee members Dr. Mark Solt and Dr. Ying Zhang, and Dr. Vinka Craver, my thesis committee chair I could not have graduated due to a constrained schedule due to working. Thank you for your support through this process.

I'd also like to thank the URI Department of Geosciences, from our weekly seminar meetings, chats in the office, and providing professional training. Specifically, I'd like to thank Dr. Brian Savage and Dr. Elizabeth Laliberte for serving as my teaching mentors while I served as a teaching assistant for their courses. The department overall has been an extremely supportive and positive environment, made me feel like home away from home (which at times, it was!). Many thanks to my fellow Cardace laboratory graduate students, Alexander Sousa, Mahrukh Shaikh, Meg Wilson, and Abigail Johnson. Thanks for all of the fun talks and adventures these past couple of years. Thanks, in general go to my fellow students in the Cardace laboratory team and in the department. Thanks to Ken Wilkinson, for his contribution for running most of the XRD samples. Thank you also to Laura Messier, Dr. Joeseph Boesenberg, Joe Orchardo, and David Murray, all at Brown University, without whom I could not have completed the geochemical analyses. Further thanks go to Homestake Mining Co. and UC Davis McLaughlin Natural Reserve for core samples and lodging during the sample collection

during the 2017 field season, along with Michael Kubo from NASA Ames for his advice.

Without the financial support from NASA RI Space Grant for a fellowship during the 2016-2017 year, I would not have been able to attend graduate school. In addition, analytical work for this thesis was also paid in part by the NASA Astrobiology Institute's Rock Powered Life initiative. Further, I was also funded by the University of Rhode Island, College of the Environment and Life Sciences and Department of Geosciences for helping provide support for attending both regional and international meetings. Thank you to Dr. Karen Kortz for connecting me with teaching at the Community College of Rhode Island (CCRI), which helped in part, pay for my educational expenses. Thanks also go out to the CCRI Physics Department who encouraged me to write. Finally, I am thankful for my family and friends who have supported me throughout this process. Thank you, Ilana, for all your unwavering commitment to me finishing this degree and contributing your organization skills to my life. Both my grandmothers, Shirley and Mary have always been there to help and talk, my two aunts, Bobbie and Julie and my uncle John have also helped me along this process, all working in STEM pushed me to pursue a career in science, and I am glad I listened. My brother Dylan helped with moving the samples when arriving back from California and has always been there to give a helping hand. I could not have gotten through this without their support. Most of all, more than words could describe, thank you Mom you are amazing.

PREFACE

This thesis is written in the manuscript format for the leading journal Chemical Geology, within the recommended framework of the Graduate School at the University of Rhode Island.

TABLE OF CONTENTS

LIST OF TABLES

LIST OF FIGURES

FIGURE PAGE

MANUSCRIPT—1

Terrestrial Planet Serpentinization in Mélange Terrains

Roger Hart[1] and Dawn Cardace[1]

[1]University of Rhode Island, Department of Geosciences, Kingston, RI

Corresponding Author:

Roger Hart

Department of Geosciences

University of Rhode Island

331 Woodward Hall

9 East Alumni Avenue

Kingston, RI, 02881, USA

Phone: +1 (508) 558-0856

Email: Roger_hart@my.uri.edu

This manuscript, R. Hart, & D. Cardace. (In preparation) Terrestrial Planet Serpentinization in Mélange Terrains. In Preparation. *Chemical Geology*., is in preparation for publication.

1. INTRODUCTION

In mélange environments, Mars and Earth have planetary lithospheres with exposures of mantle-derived ultramafic rocks (Longhi et al., 1992), the serpentinization of which contribute to thermodynamic habitability. Ultramafic igneous rocks are the Fe- and Mg-rich parent rocks to serpentinites; initial mineralogies in these parent rocks are dominated by pyroxene and olivine, and transform to serpentine, brucite, magnetite, and other minerals via hydration and other reactions (see Holm et al., 2015). More specifically, ultramafic rocks are chiefly composed of the silicate minerals of olivine ($(Mg,Fe)_2SiO_4$), orthopyroxene ($(Mg,Fe)SiO_3$), and clinopyroxene ($Ca(Mg,Fe)Si_2O_6$). Specific solid-phase geochemical atomic arrangements observed in terrestrial ultramafic rocks require that magnesium and iron occur in a compositional ratio of ~9:1 (Sleep et al., 2004). The end members of both the olivine group [forsterite (Mg_2SiO_4) and fayalite (Fe_2SiO_4)], and the pyroxene groups [enstatite ($MgSiO_3$) and ferrosilite ($FeSiO_3$), diopside ($FeCaSi_2O_6$) and hedenbergite ($FeCaSi_2O_6$)] can undergo hydrolysis reactions to form serpentine and other metamorphic minerals, through serpentinization reactions (Table 1.) Though the net reaction (reaction 1) leaves a serpentine-dominated assemblage, multiple stepwise intermediate reactions have mineralogically distinct paths: pyroxene alters to serpentine (reaction 2), pyroxene and olivine alter to serpentine (reaction 3) (Moody, 1976), and additional similar reactions also occur (reactions 4 & 5). Specifically, with the oxidation of Fe^{2+} in olivine coupled to the reduction of hydrogen in H_2O to free H_2, biologically useful hydrogen is produced, and multiple known

microbial metabolisms can be powered. Methanogenesis, methanotrophy, and metal reduction reactions coupled to hydrogen oxidation are key among them. These are likely to be common reactions in (bio)geochemical systems in ultramafic rocks, given the presence of liquid water.

On Earth, varied tectonic environments produce ultramafic rock assemblages. Mantle minerals undergo hydrolysis at temperature, pressure, and compositional conditions present in the crust and upper mantle. This location, where Earth's pressures and temperatures are in the constrained range of less than the pressure-temperature resulting in the instability of antigorite, a serpentine mineral polymorph stable to approximately 950K and 5.0 Gpa (Wunder et al., 2001), provides a lithospheric limit on habitability of serpentinization. Serpentinization is considered on Earth to be a possible geological driver of the establishment of life on Earth (Schulte et al., 2006; Sleep et al., 2011) and there is a diversity of deep life tied to serpentinites in the terrestrial seabed (Schrenk et al., 2013) and low-temperature hydrothermal vents, as at Lost City Hydrothermal Vent Field (Kelley et al., 2005). At this site, observed seawater and upper mantle peridotite react and produce serpentine polymorphs, accessory minerals, and biologically relevant aqueous species dissolved in the fluids (Kelley et al., 2005). Biological diversity at this location is significant (Brazelton et al., 2006). In continental serpentinization systems, impacts of the same class of water-rock reactions can be observed in groundwater ecosystems where there is biological diversity tied to the aqueous species and minerals produced (Crespo-Medina et al., 2014). Observations of the Mars have identified serpentinization-related rocks and mineral deposits (e.g., Ehlmann et al., 2010), underscoring the possibility of biotic processes on Mars, and

renewing interest in ocean worlds with subsurface silicates. Serpentinization also holds promise in understanding extraterrestrial environments where biotic processes can possibly occur. Modeling and experimental work on serpentinization across pressure and temperature ranges of up to 500 bar and 700K have indicated that production of abiotic CH_4, H_2, and heat (via exothermic reactions) are to be expected (cf. McCollom and Seewald, 2001; Allen and Seyfried Jr., 2003; Seyfried Jr. et al., 2007). Biological utility of selected gases and aqueous species is central to understanding the role of serpentinization in the origin of life on early Earth and the case for the establishment of life on other rocky celestial bodies (Ehlmann et al., 2010; Boye Nissen et al., 2015). Ultramafic rocks are common rock units among the terrestrial celestial lithospheres, such as Mars, Earth, and the Moon. This makes terrestrial planet lithospheres likely candidates to support astrobiological chemistries and exhibit non-equilibrium characteristics that present an interesting location for biological processes and even organisms to exist (Carnevale et al., 2011). In addition, rocky planets are large energy and chemical reservoirs to drive astrobiology and specifically, are sites where fluid-rock interactions can occur and be used to understand the habitability conditions of these interactions through specific thermodynamic constraints (see Scambelluri et al., 2004). There is exciting scientific discussion regarding serpentine formation in terrestrial planets and icy satellites across multiple hypotheses and current research, in both terrestrial analogs (Preston & Dartnell 2014; Foing et al., 2011) and extraterrestrial environments for favorable conditions for serpentinization. These research foci include questions such as the presence of ultramafic rocks interacting with sub-ice oceans in icy-satellite systems of Enceladus and Europa (Russell et al., 2014), the interaction of

Martian ultramafics with an aqueous phase in the production of serpentine minerals (Holm et al., 2015; Ehlmann et al., 2010), and serpentinization reactions on small-bodies, such as asteroids (Nathues et al., 2014) and comets (Holm et al., 2015). In the Coast Range Ophiolite Microbial Observatory (CROMO) in the McLaughlin Natural Reserve, California, ophiolite-hosted peridotite has undergone serpentinization (Cardace et al., 2013), and is present in a mélange composed of serpentinite blocks, disordered exotic and country rock clasts and inclusions, surrounded in a fragmentary and fine grain matrix (Moody, 1976; Hopson et al., 1981; Shervais & Kimbrough, 1985) gabbro and marine sedimentary sequences are regionally common also. The CROMO serpentinites are useful extraterrestrial analogs for altered ultramafic material in planetary mélange terrains because of the appropriate mineral assemblages and complicated tectonic and geological history of the location, resulting in a varied petrology and structure.

Mars has long been a target of astrobiological research focusing on the emplacement of ultramafic rock units undergoing serpentinization (Schulte et al., 2006; Michalski et al., 2013). Ehlmann et al. (2010) provided analysis of serpentine deposits detections based on Compact Reconnaissance Imaging Spectrometer for Mars (CRISM) data for the Martian surface. The CRISM observations, at resolutions of 18-40 m/pixel (Murchie et al., 2009; Ehlmann et al., 2010), identified serpentine in three distinct geological setting across the surface of Mars: mélanges, features of impact craters, and in rocks with high concentrations of olivine. Mélange terrains that exhibit serpentine on Mars are from the Noachian, at two primary localities the Claritas Rise and the Nili Fossae (Ehlmann et al., 2010). During this time period, Mars exhibited different

planetary environmental conditions than today; Mars was wetter, as indicated by the significant phyllosilicate deposits and geomorphic signatures such as drainage channels and fans formed by flowing liquid, likely water, systems (Moore et al., 2003; Fassett & Head, 2008). In the Claritas Rise (Figure 1), mineralogy includes serpentine, chlorite, kaolinite, and illite or muscovite (Ehlmann et al., 2010). Near the Nili Fossae (Figure 1 and 2), the dominant mineralogies are serpentine, smectite, kaolinite, low-Ca pyroxene, and olivine. Other observed serpentine deposits have been identified in a small amount of impact craters, in the morphological features of the walls, ejecta, and the central peaks, in the Chia crater (Ehlmann et al., 2010). These deposits are also temporally correlated to the Noachian period of the planet's geological history, with minerals present including chlorite and smectite (Ehlmann et al., 2010). In addition, serpentine has been observed in geological settings that are very olivine-rich. These sites are located in a location where there is Early Hesperian Syrtis Major volcanic activity, representing the unit of high levels of olivine--and the underlying stratum is Noachian, with co-occurring olivine, carbonates, and serpentine (Ehlmann et al., 2010). Furthermore, the carbonate has a distinctive absorption feature of magnesium carbonate (Ehlmann et al., 2008). The prevalence of olivine rich units along with low-Ca pyroxene indicate that the Nili Fossae is likely an ultramafic hosted rock unit (Ehlmann et al., 2010), however specific geochemistry of this area is unavailbe at the resolution necessary associated with localized habitability. To provide a first order approximation for modeling of the habitability of the Nili Fossae, lherzolitic shergottites are used to represent the geochemistry of the Martian ultramafic, olivine rich, units (Mikouchi and Kurihara, 2008).

This thesis considers serpentinization and post-serpentinization weathering reactions in mélange terrains similar to those on Earth and Mars, based on Coast Range Ophiolite observations, with particular application to the Nili Fossae region on Mars. This work investigates how serpentinites in mélange settings contribute to the near-surface localized habitability tied to simple microbial metabolisms. The specific geochemistry of heavily serpentinized ultramafic rocks at the Coast Range Ophiolite at the McLaughlin Natural Research Reserve and the specific provenance of the ultramafic rocks, with respect to the large-scale geodynamic model of the region is the first objective. The Nili Fossae is a mélange jumble with abundant olivine and serpentine in the rock units in this region provide a caveat, Earth based tectonics that result in olivine rich units with serpentine in mélange settings are ophiolite based, usually in active continental margins, and Mars does not have significant evidence of plate tectonic processes. Current investigations and theories concerning Martian plate tectonic models do not describe large scale surface physiographic structures, like the hemispheric dichotomy and no large expanses of felsic continental crust and are likely formed from analogous subduction unrelated processes, such as mantle plume processes, and mid-ocean ridge settings with magnetic anomalies, which have been identified on Mars (e.g., Breuer and Spohn, 2003). I hypothesize that there is analogous large scale tectonic geochemical signatures indicating a depleted mantle source at McLaughlin Natural Reserve in the serpentinized ultramafics. Using major element chemistries of the altered rock, I expect the major element chemistry to be enriched MgO with respect to SiO_2 and TiO_2 weight percent as opposed to subduction-related tectonic settings which cluster 5-20 weight percent lower than subduction

unrelated tectonic settings, such as mid-ocean ridges or plume settings (Choi et al., 2008). Furthermore, Coast Range Ophiolite at McLaughlin and the Nili Fossae both are sites of geobiolocal and astrobioloical research, respectively. Manipulating conditions associated with serpentinization such as energy factors for reactions and life, the available mineralogy for reactants and products, and the properties of aqueous solutions of serpentinization zones in the mélange geophysical settings containing serpentinites can influence localized habitability. Prior work using Gibbs Free Energy (Amend & Shock, 2001) indicates that biochemical metabolisms, such as methanogenesis, are habitable at specific geophysical conditions relevant to earth and planetary environments. To analyze the habitability of serpentine rich units in mélange geophysical settings, the specific geochemistry of mélange terrain rocks is necessary. Geochemical analysis of the mélange rocks is necessary to derive ultramafic, localized, habitability, and thus the drivers that result in the formation of the mélange jumble. Using the physical and chemical properties of the changing rock, I infer evolving habitability conditions using numerical simulations coupled with thermodynamic modeling, particularly based on changing gas and liquid loads in the system as it evolves through the solid phase transformations. Using the reaction quotients and stoichiometric coefficient, does the solid phase geochemical changes and inferred chemistries of fluids passing through serpentinites change the serpentinite bulk geochemistry and mineralogy over the extent of the reaction progress, and does this alter localized habitability conditions? I interpret results of this habitability model in the context of available geophysical and geochemical data on extraterrestrial serpentinization systems such as appropriate for Nili Fossae, Mars. I show that the

production of astrobiologically relevant chemical species (i.e., CH_4) via serpentinization changes under different geophysical and geochemical conditions that simulate specified environments on Mars and Earth.

2. GEOLOGICAL SETTING

2.1 The Coast Range Ophiolite: terrestrial site of serpentinization.

The Coast Range Ophiolite, California, USA has been the subject of diverse geophysical, geochemical, and geological studies (e.g., Hopson et al., 1981; Shervais et al., 2004; Choi et al., 2008). Over the past four decades, investigating the underlying geodynamics of the Coast Range Ophiolite (CRO) has resulted in three theories to explain its formation. First, the units of the CRO have been proposed as sourced from a mid-ocean ridge, based largely on stratigraphy (Hopson et al., 1981). Second, the CRO has been proposed as a product of back-arc basin development, based on regional structural geology (Ingersoll, 2000). Third, CRO units have been interpreted as formed in a supra-subduction zone setting, specifically due to active fore-arc spreading, based on whole rock and mineral geochemistries (Choi et al., 2008) (Figure 5). Taken as a whole, the formation of the CRO remains controversial: different units of the ophiolite have different geochemical signatures. Major igneous and metamorphic lithologies are described in detail in Choi et al., (2008); there are juxtaposed exposures of gabbro, diorite, basalt, andesite, and serpentinized peridotite in this area. Basalt units exhibit island arc volcanism signatures (Shervais 1990; Giaramita et al., 1998; Choi et al., 2008), dikes and sills represent very similar chemical signatures to mid-ocean ridge basalt (MORB), and ultramafic mantle-derived rocks display supra-subduction zone setting chemistries. The exposed ultramafic peridotites have been nearly fully serpentinized in northern California (Figure 6), and

are now undergoing weathering processes, generating serpentine-rich mineral soils and gradients in shallow subsurface groundwater geochemistry (Cardace et al., 2013).

The rocks of interest here are part of the regionally extensive Coast Range Ophiolite, sampled in the UC-Davis McLaughlin Natural Reserve locality in Lower Lake, CA. These are predominantly altered peridotite, and consist mainly of relict primary minerals (olivine and pyroxene) and secondary phases (serpentine and other clays, carbonates, and magnetite). CRO peridotites are from the Jurassic period and have likely been exposed to and are reacting with Cretaceous seawater trapped in the rocks the prior to uplift plus some meteoric water inputs in this geographical location (Cardace et al., 2013, 2014). Pressures and temperatures of the Coast Range Ophiolite are variable within near Earth-surface conditions, between approximately 0-100ºC (273 K-373 K) 1-35 bar (up to 0.35 GPa) in the location of CROMO, using the first order pressure equation (Hart & Cardace, 2017).

2.2 Nili Fossae Mars

Olivine units with an expanse of approximately 30,000 km^2 with high FeO compositions, ranging from solid solutions of 30-70 percent fayalite (Fe_2SiO_4) was identified by Hoefen et al. (2003) using the Mars Global Surveyor's Thermal Emission Spectrometer (Figure 7) at the Nili Fossae (Hoefen et al. 2003). The Nili Fossae is a large mélange terrain depression (elevation -0.6 km) that is located in the Syrtis Major quadrangle at approximately 22°N, 75°E. Prior work completed by Christensen et al. (2000; 2001) initially showed the presence of olivine in Martian surface rocks, primarily the darker regions noting to basaltic lithologies. Further investigations into the olivine in the Nili Fossae region using the OMEGA spectrometer on Mars Express

(Mustard et al., 2005; 2007) has also identified phyllosilicate deposits (Bribring et al., 2005; Mangold et al., 2007). Serpentine detection has since been confirmed (Ehlmann et al., 2010). In the tectonically complex region of the Nili Fossae, the horst blocks contain serpentine and phyllosilicate accessory minerals of chlorite, kaolinite, and illite (Ehlmann et al., 2010). At the observational resolution of 5 m/pixel, no localized stratigraphy could be inferred, yet the spectral evidence of serpentine is highest in the horst block material and in the adjacent grabens where there is weathering of the horst block material (Ehlmann et al., 2010). Based on stratigraphic analysis of the nearby impact basin of the Isidis Planitia indicate that the Fe-rich olivine was underlain by surface regolith and were thus emplaced on the surface of the region by the impactor (Hoefen et al, 2003). The geological age of these serpentine-rich units are of early to mid-Noachian age between 4.00 Ga and 3.85 Ga, during the period of the Late Heavy Bombardment and the origin of life on our planet. Structurally, there are three distinct rock units observed in this locality, an altered cap rock of elevated silica and an olivine-poor lithographic unit, overlaying an olivine rich unit with magnesium carbonates (Ehlmann et al., 2008), serpentine (Ehlmann et al., 2010), and talc (Brown et al., 2010), with the basement unit being limited in olivine and phyllosilicates including magnesium and iron smectite, potentially nontronite or saponite (Michalski et al., 2015; Peretyazhko et al., 2016). The aqueous alteration of the units in the Nili Fossae are a primary concern for astrobiological investigations, with recent studies on the production of methane from this region (Mumma et al., 2009), more specifically, the prospects of analog sites for serpentinization (Amador et al., 2017). Pressures and temperatures of the Nili Fossae are variable, but lower than near Earth-surface

conditions hosting the serpentinization of similar rocks on Earth. Mars has lower pressure and lower temperature. These geophysical constraints affect the stability of volatile substances, such as water. Water in liquid phase is thermodynamically unstable on the surface of Mars, with mean surface temperatures on the order of -53^{o}C (220 K) and pressures around 0.006 bar (600 pascals); water is typically in the form of permafrost (Feldman et al., 2004; Oze & Sharma, 2005). Furthermore, habitability on Earth is closely tied to the stability diagram of water, specifically the liquid phase of water through 273 K to 373 K, thus appropriate biological constraints are in the subsurface. Given a reasonable Martian lithosphere geothermal gradient of 5-20 K/km (McGovern et al., 2002) and disregarding pressure issues, habitable temperatures may occur at ~3 (hotter gradient) and ~11 (cooler gradient) km below surface, but get too hot for stable liquid water by ~8 or ~31 km, depending on gradient. In the Nili Fossae, minerals identified were serpentine, smectite, kaolinite, low-Ca pyroxene, and olivine; with a mean density of 3000 kg/m^3 appropriate for first order approximations for Martian subsurface serpentinization investigations (Oze & Sharma, 2005). At depths greater than ~5 m of surficial mantle exposures, pressure and temperature conditions will be analogous to Earth-surface conditions, since the Nili Fossae experiences Martian equatorial climate (McEwen et al. 2011), and temperatures measured by Thermal Emission Imaging System (THEMIS) (Christensen et al., 2001) are between ~250-300 K, which is in the range of the freezing point of a 3-5% salt water solution with an approximate density of 1035 kg/m^3. Thus, the subsurface ultramafic rock unit at the Nili Fossae (below ~5 meters' depth) has enough radiation shielding to allow life. At this depth, cells and biological debris would be beyond the incident

electromagnetic and energized particle irradiated zone, which would ionize biological molecules and render the environment sterilized (Hassler et al., 2013). The current depth of this sterilization is computed between 2-4 meters of depth beneath the Martian regolith, depending on the density of the overlying material; the maximum depth depends on assumptions regarding near-surface Martian felsic soil properties and a deeper ultramafic unit (Hassler et al., 2013).

3. MATERIALS AND METHODS

3.1 Sample Collection

Serpentinite samples (N=41) were obtained from the Coast Range Ophiolite in the McLaughlin Natural Reserve. Of the 41 samples, 13 samples were obtained from between 72.85 m to 103.63 m below land surface, sourced from archival core material drilled by Homestake Mining Company Co. (now Barrick Gold Corp., M81-313 drilling project). Drilling specifications are available for 19 samples from two coring localities, QV 1_1 (N=9) and CSW 1_1 (N=10), which were obtained in August 2011 by the Cardace drilling team (Cardace et al., 2013). The drilling company contracted was Cascade Drilling, who employed a 96 mm outer diameter, Central Mine Equipment Company (CME) model 75 auger rig using purified, 1-micron filtered water as the drilling fluid (Cardace et al., 2013) culminating in the establishment of 8 aqueous geochemical and microbiological monitoring wells as the Coast Range Microbial Observatory (CROMO). QV 1_1 and CSW 1_1 drill core samples from the Cardace drilling team were cataloged and curated after best practices outlined by the Integrated Ocean Drilling Program (IODP) (Cardace et al., 2013). Cores were described, photographed, and placed in combusted aluminum foil for this work. In addition, surface mini-cores were obtained at three, geographically distinct, outcrops of serpentinized ultramafic units in the McLaughlin Natural Reserve in 2017 (N=9). Site 1 (N=3), 2 (N=3), and 3 (N=3) were obtained on fresh rock surfaces at a depth between 10-15 cm, drilled perpendicular to the rock surface using a Makita Electric Core Drill Model DE-T3, equipped with a 3-cm I.D. core barrel (McL_Site_1, McL_Ste_2, McL_Site_3).

Samples were then stored in sterile, 50 ml conical polypropylene centrifuge tubes (Thermo Scientific™ Nunc™) for mineral chemistry mineralogical, and geochemical analyses. All samples were investigated using traditional optical petrography for textural analysis, x-ray diffraction (XRD) for bulk mineralogy, and inductively coupled plasma atomic emission spectroscopy (ICP-AES) for bulk geochemistry. Subsamples of cored material were analyzed via electron microprobe analysis (EMPA); specifically, one surface sample collected in the Cardace drilling team (August, 2011 McL_CROMO_Surface) and three Homestake Mining Company Co. cored samples (M81-313-239A, M81-313-329, M81-313-356).

3.2 Analytical Methods

3.2.1 Thin Section Petrography

Traditional optical petrography was employed to identify major mineral phases, to assess degree of alteration and deformation (if any), and to screen samples for relict olivine minerals in McLaughlin serpentinites (see figures 4-53). Samples were professionally prepared as highly polished, electron microprobe analysis grade thin sections, by Spectrum Petrographics, Inc. (www.petrography.com). Samples were ground, fixed in a clear resin, mounted to a petrographic slide using acrylic, polished and finished to a final thickness of 30 μm using 0.5 μm grit diamond abrasive. Thin section analysis was completed on an Olympus BH-2 petrographic microscope in plane-polarized, cross-polarized, and using the gypsum plate (530 nm) at magnifications from 2X-40X and representative thin sections were photographed on a fixed Olympus DP73 digital camera. Analysis of thin section samples were completed using the Stream Essentials 1.9 image analysis software in conjunction with the Michel-Lévy Interference

Color Chart. Modal estimates were calculated through utilizing the same magnification, thus thin section surface area, point count of mineral phases based on Winter (2013).

3.2.2 X-Ray Powder Diffraction

Samples were analyzed for semi-quantitative, bulk mineralogy, using x-ray powder diffraction (XRD) (see figures 54-97). Sample preparation followed standard procedures outlined by Cardace et al. (2013). In brief, samples were powdered with a percussion mortar (URI Dept. of Geosciences) and/or a mortar and pestle. Powders were then passed through a 150 μm pore size sieve, until approximately 15.0 mg of sample was collected, and transferred into the XRD sample chamber. Samples were analyzed on an Olympus Terra portable x-ray diffractometer with a Cobalt (Co) X-Ray tube with a charge-coupled detector (CCD) (Blake et al., 2012). The Co anode instrument parameters during analyses (10 W, 30 kV, and between 5-25 keV) were maintained throughout 1000 exposures. The diffractograms were interpreted using XPowder software, which references databases for mineral peak d-space identification, and allows for peak characterization. XRD diffractograms of clay minerals, including serpentine and kaolinite, exhibt 7-angstrom spacing which can cause major peak overlap, when interpreting the identification of the diffractogram, thus it is necessary to utilize more than one peak in the identification process using the XRD diffractogram.

3.2.3 Inductively Coupled Plasma Atomic Emission Spectroscopy

Serpentinites were prepared for analysis on the Thermo Scientific iCAP 7400 DUO ICP-AES using the flux fusion method after Murray et al. (2000) ODP Technical note 29; analysis was conducted at the Brown University Environmental Chemistry Facility (Providence, RI). 100 mg of unweathered McLaughlin sample were ground and

dried. Samples were thoroughly mixed with lithium metaborate flux (Aldrich #25428-2), in a flux to sample ratio of 4:1, approximately 0.16 g (±0.05) of lithium metaborate flux to 0.0400 g (±0.005g) of sample. The samples and flux, were heated and melted in a graphite crucible (SPEX/Certiprep #7152HP) in a furnace for 10 minutes at 1050^{o}C and then the fused-glass sample bead was poured into a previously prepared (ACS grade) 10% nitric acid solution. Samples were agitated for 45 minutes and underwent a dilution of 4000 x and filtration through a 0.45 micron Gelman filter attached to a syringe before samples were analyzed by the ICP-AES. The ICP-AES analytical run was completed in both radial and axial modes for most elements, except in some samples, Ca and Mg were too saturated and thus oversaturated the detector. Thermo Scientific Qtegra software, across wavelengths ranging 166-847 nm was used for selecting elements of interest (44 elements in total). Internal standards (5) at the Brown University facility and external standards from the University of Rhode Island (9) as standard reference materials (SRMs), and 3 flux blanks were analyzed to constrain any geochemical signals contributed by the flux. Samples were also selected for triplicate analysis to assess variability through the analytical run. A drift solution was also prepared to monitor instrument drift through the analytical run. Concentrations of elements of interest in serpentinites were obtained by processing wavelength counts and relating the wavelength counts of each element against the published values of the standards, as in Murray et al. (2000).

3.2.4 Electron Microprobe Analysis

Electron microprobe analysis (EMPA) was conducted at Brown University in Providence, RI on a Cameca SX-100 electron microprobe analyzer to identify major

mineralogical phases and identify specific mineral chemistries for relict and neoformed (via metamorphism) grains (N=4). In situ, non-destructive analysis of the mineral veins was also carried out. Standard probe analysis was used for the system parameters of a 1-μm, 15 nA beam aperture at an accelerating voltage of 15 kV (after Elkins-Tanton et al., 2007). San Carlos Olivine was utilized as the mineral standard in the calibration of the Cameca SX-100 microprobe. Sub-samples for analysis were chosen using the scanning mode of the Cameca SX-100 microprobe, which functions as a scanning electron microscope (SEM) with semi-quantitative, chemical-based, mineralogical identification tool using energy dispersive spectroscopy (EDS). Backscatter electron images (BSE) were obtained of sites of interest. Once viable locations were determined using EDS, mineral chemistry analyses used wavelength dispersive analysis (WDS). Data correction followed standard procedures, using Olivine, NMNH 111312-44 as the standard reference material for analysis (as in Elkins-Tanton et al., 2007). Values for major mineral chemistries were obtained as oxide weight percent and converted to atomic mass fractions, post analysis.

3.2.5 Data Validation and Statistical Approaches

For the ICP-AES and electron microprobe analyses, data obtained were normalized through the goodness of fit of calibration curves using linear regression and R^2 values to determine the relation between standardized values and observed values of both the bulk and mineral chemistry values (Rollinson, 2014). In addition, the mean of drift and blank count intensity values were utilized in the ICP-AES data reduction and correction. Regarding XRD data, conventional use of XPowder peak-matching software allowed background subtraction and peak identification. Use of the semi-quantitative modeling

tool in XPowder further allowed modeling of diffractograms as mixtures of ideal mineral endmembers; for internally consistent sample comparisons, XRD profiles were considered as model mixtures of selected reference olivine, pyroxene, lizardite, antigorite, etc. Modeled semi-quantitative abundances were then plotted in Excel.

3.2.6 Modeling Framework

To model the water-rock reaction paths located at the geophysical sites of serpentinization, I used The Geochemist's Workbench (www.gwb.com), 10th Edition, which is a commercially available geochemical modeling software that predicts equilibrium compositions and provides activity calculations. This software calculates solute activity using the extended Debye-Huckel "B-dot equation", which is useful for ionic strengths of 0.3 molal to 3 molal for NaCl-dominated solutions through 273 K to 573 K (Helgeson, 1969; Bethke, 2011). A major limitation in the Geochemist's Workbench for planetary geochemical modelling is the set system parameter of pressure, in that different planetary environments exhibit different pressures, both on the surface and the interior, but cannot be perfectly modeled. The current thermodynamic database for the default setting at 1.013 bar in the thermo.tdat is not effective for non-Earth surface water-rock interactions such as the bottom of the seafloor and rock pore-fluid capillary pressure, or subsurface oceans underneath masses of ice reacting with rocky substrate. In these scenarios, common to terrestrial planetary bodies, pressures often exceed 1.013 Bar and extend upwards to hundreds of gigapascals. Thus, the thermodynamic database needed to be altered to accommodate end-member pressure ranges of this investigation between 1.013 Bar and 75 bar, reasonable pressures for both the Coast Range Ophiolite at CROMO (Cardace et al.,

2013) and the Nili Fossae on Mars (Achille & Hynek, 2010; Michalski et al., 2013). I utilized a modified thermodynamic database from thermo.com.V8.R6+.tdat, distributed at https://www.gwb.com/data/thermo.com.V8.R6+.tdat (Oelkers et al., 2009; Parkhurst and Appelo, 2013), modifying the SUPCRT92 pressure then following the pressure curve of water after the vapor point. I did not introduce new species into the thermodynamic dataset of 81 elements, 82 basis species, 183 redox couples, 1503 aqueous species, 1122 minerals, 93 gases, and 42 oxides. Temperatures of the reactants and waters were kept invariant to keep computational times within a reasonable range (all simulations were performed on a Dell Inspiron 780). Our simulations were completed with using the geophysical constraints of temperature and pressure appropriate in the mélange terrains while allowing the system to change in terms of water-rock ratio, pH, and redox activity of the aqueous solution. Initial system mineralogies and aqueous species were based on the mineral and chemical properties of a model protolith [Coast Range Serpentinite] analytically determined using petrography, X-ray diffraction (XRD), and electron microprobe (EMP)], major element concentrations (weight %) were obtained across two crystals of olivine (A.2 & A.3) from McL-239A and McL-329. Other values for further constraints on serpentinization reaction on Mars was modeling the aqueous alteration and serpentinization of the lherzolitic shergottites, Y000027, Y000047, and Y000097 (Mikouchi & Kurihara, 2008) which exhibit similar olivine weight percent values to CROMO olivine. Based on lherzolitic shergottites, major element chemistries for olivine were averaged as well as their major modal mineralogies and then were modeled in a water-rock reaction pathway. All mineralogies in the simulations were

imputed as weight percent values of olivine and bulk mineralogy was maintained during the initial start of the reaction progress. Output files were complied and although fine scale reaction progress steps, x_i, were available, I analyzed activity data for every tenth of x_i space through the simulations for the thermodynamic Gibbs Energy calculations.

Two mineral species, brucite and ilmenite, could not be modeled due to simulation failure at test, so values were converted to wt% Mg, O, Fe, and TiO_2 based on atomic formula units. The Na-Cl seawater ocean is based on modeling computations also followed carbon dioxide partial pressure of 0.0003 averaged from terrestrial ocean chemistry from Hem (1985). The Mg-Cl ocean is based on Mg values common in an Mg brine in an icy-sealed lake in Antarctica (Murray et al., 2012). The Ca-Cl ocean is based on Ca values common in an Ca brine in a hydrothermal calcium-rich brines of Death Valley and Bristol Dry Lake, California (Lowenstein & Risacher, 2009). These are reasonable, Earth-based aqueous phases hypothesized to have existed on Mars during the Noachian geological period (Michalski et al., 2013).

Bioenergetic modeling (as in Amend and Shock, 2001; Cardace et al., 2015) utilizes model outputs from Geochemist's Workbench REACT modeling to constrain the ion activity product (Q) needed to solve for Gibbs Free Energy (G). When the thermodynamic system is at constant temperature and pressure, the Gibbs Free Energy for a chemical reaction in the system depends on the extent of the chemical reaction, Xi or ξ, and at system chemical equilibrium the change in Gibbs Free Energy over the extent of reaction equals zero. Of a reaction system, the equation to result at a G value, used in this work, is

$$\left(\frac{dG}{d\xi}\right) = dG_r^o + RT \ln Q.$$

In this way, the thermodynamic feasibility of selected reactions can be determined, with a negative value resulting in a spontaneous reaction. Here, the methanogenesis (MG) reaction and the methanotropy (MT) reaction are considered. The Gibbs Free Energy metabolic reaction modeling utilized here examines chemical activities of steps of Xi=0.1, until Xi=1.0, when the reaction in the GWB REACT simulation achieves equilibrium. Modeling the water to rock ratios as 1:10, 1:1, and 10:1, resulted in slight changes in the activities of water and aqueous species in the metabolic reactions of methane cycling, when employing significant figure rules, differences were on the nano-scale, which is smaller than the resolution of the thermodynamic reaction path modeling software, thus computations were performed on the mean values. Using descriptive statistics, in this case the mean values of the activities, did not affect the results for the species investigated.

4. RESULTS

4.1 Thin Section Petrography

Representative thin sections (N=16; Table 4) were analyzed using modal estimates, methods from Choi et al. (2008) by point counting. Surface samples included collected hand samples and mini-core 10-cm-long samples (Figure 3). Core samples were subsampled from the CROMO cores (CSW and QV; Figure 4) and the Homestake core (M81-313; Figure 5). Mean mineralogies were compiled to determine qualitative differences between sample sites. Lizardite and antigorite, serpentine polymorphs, are not distinguishable in thin section. However, chrysotile, the fibrous, elongated phase is readily identifiable. Serpentine appears tan to light green in plane polarized light and exhibits first order interference colors. Samples exhibit fracturing of primary minerals and overgrowth by the serpentinization reaction, resulting in sparse, fragmented olivine grains, possibly translated from initial locations. Serpentinized olivine and orthopyroxene were distinguished based on retained crystal structure: serpentinized olivine retains a rounded grain mass, and orthopyroxene retains lamellae. Further, in terms of birefringence, olivine exhibits second order interference colors and orthopyroxene exhibits first order interference colors (figure 4a). Clinopyroxene was determined through structure and birefringence, with coarse lamellae and higher order interference colors, with respect to orthopyroxene. Magnetite was identified as an opaque phase that retains its opacity using cross polarization and in plane polarized light. Clay minerals were identified as thin sheets

that could not be individually identified at the resolution of the petrologic investigation.

The hand samples exhibited metamorphosed mineral phases of olivine and orthopyroxene, with only McL-3 exhibiting deformed clinopyroxene. Magnetite was between 5-15% abundance in the thin section view, with McL-3 containing clinopyroxene exhibiting the lowest amount of magnetite grains. The amounts of clay in the samples was variable, between 0-15%, where the McL-3 mini core exhibiting no evidence of clays. Overall, relict minerals still displaying primary mineral textures were <5%, almost entirely replaced by serpentine.

Of the representative core samples analyzed, between the two drilling operations, the Homestake cores showed elevated amounts of relict primary minerals. The CROMO cores exhibited 60-70% olivine-textured serpentine and 5-10% relict minerals that have yet to become serpentinized. Orthopyroxene-derived textures and relict minerals were observed between 5-20%. Clinopyroxene was not observed in the CROMO cores at the resolution of the analysis. Magnetite and clay minerals were also present in these samples, where magnetite was present in volume percent of 5-25% and 5-15% volume was reported as clay mineralogies. The Homestake cores exhibited higher percentages of olivine and serpentinized olivine structures than most of the CROMO cores and included more relict primary olivine and orthopyroxene crystals. Clinopyroxene was observed in only two of the representative core samples, identified with lamellae and second-order blue interference colors. The Homestake cores also contained 10% magnetite and between 0-10% clay minerals.

Mean mineralogies were calculated for major rock type determination, in addition to the analyzed slides, using the peridotite-pyroxenite ternary phase diagram. The representative samples plot in the lherzolite stability field predominantly, with one sample (CSW1,1_15_12-5) determined as a harzburgite-lherzolite. McL-2 mini core and McL-1 mini also was on the harzburgite-lherzolite, however both were greater than 75% within the stability field of lherzolite.

4.2 X-Ray Powder Diffraction

Representative samples were (N=40) were analyzed using X-ray powder diffraction. Diffractograms from the surface and cores from the M81-313 Homestake were analyzed for major mineral phases present in the sample. The most common minerals identified in the samples were polymorphs of serpentine, in 38 samples. Between the polymorphs identified of serpentine ($Mg_3Si_2O_5(OH)_4$), antigorite was identified in 10 samples and lizardite was identified in 28 samples. Other minerals identified in the diffractograms of the samples were accessory minerals in the serpentinization reaction progress, with 5 detections of portlandite, ($Ca(OH)_2$).

Relict minerals of primary peridotite were also identified in the representative diffractograms. Olivine ($(Mg, Fe)_2SiO_4$) was identified in 16 samples, with fayalitic olivine (Fe_2SiO_4) populating XRD peak-matching with 4 samples. Minerals include spinel group minerals (AB_2X_4) with varieties of magnetite (Fe□O□), with 7 samples, of magnesioferrite ($Mg(Fe^{3+})_2O_4$) with 2 samples, and two samples show the rarer magnesioferrite, which is associated with platinum group elements ($(Fe_{.447}Mg_{.417}Ru_{.115}Ir_{.021})_2(Fe_{.771}Mg_{.229})O_4$). Other alteration minerals include minerals from the chlorite group, including 5 identification peaks of chamosite

($(Fe^{2+},Mg)_5Al(AlSi_3O_{10})(OH)_8$, 5 samples have clinochlore ($Mg_5Al(AlSi_3O_{10})(OH)_8$, representing the iron and magnesium end members of the chlorite solid solution. There were also 5 samples of unspecified chlorite ($(Mg,Fe)_3(Si,Al)_4O_{10}$).

4.3 Inductively Couple Plasma Atomic Emission Spectroscopy

Representative subsamples of altered peridotite from the Coast Range Ophiolite surface samples, CROMO drilling cores, and the M81-313 Homestake core at McLaughlin were analyzed via ICP-AES for major elements (Al, Ca, Cr, Fe, K, Mg, Mn, Na, Ni, P, Si, Ti). These values were obtained in counts per second and were converted to concentration (Table 4) and then finally, represented at major element oxides (Table 9). There is great variability amongst the samples, particularly in the MgO and SiO_2 values. Aluminum oxide concentration values were between 0.831 wt% and 16.79 wt%, with CSW 25.3 and QV 137 being the highest and lowest values, respectively (s.d., 4.731), with a mean value of 5.43 wt%. Calcium oxide concentration values were between 1.17 wt% and 18.03 wt%, with samples Qv 122 and 2.2 being the highest and lowest values, respectively (s.d., 4.401), with a mean value of 2.27 wt%. Chromium oxide concentration values were between 1.19 wt% and 6.02 wt%, with samples 328 (depth in ft.) and 326 (depth in ft.) being the highest and lowest values, respectively (s.d., 0.9466), with a mean value of 2.311 wt%. Iron oxide concentration values were between 3.13 wt% and 24.9 wt%, with samples 328 (depth in ft.) and 326 (depth in ft.) being the highest and lowest values, respectively (s.d., 4.267), with a mean value of 8.17 wt%. Potassium oxide concentration values were between 0.11 wt% and 6.43 wt%, with samples QV 121 and 1.1 being the highest and lowest values, respectively (s.d., 1.277), with a mean value of 3.87 wt%. Magnesium

oxide concentration values were between 0.01 wt% and 37.9 wt%, with samples 337 (depth in feet) and QV 128 being the highest and lowest values, respectively (s.d., 11.80), with a mean value of 25.0 wt%. Manganese oxide concentration values were between 0.05 wt% and 0.259 wt%, with samples CV1 121 and QV 137.1 being the highest and lowest values, respectively (s.d., 0.052), with a mean value of 0.117 wt%. Sodium oxide concentration values were between 0.002 wt% and 10.6 wt%, with samples QV 128.1 and CSW 17 being the highest and lowest values, respectively (s.d., 2.600), with a mean value of 1.16 wt%. Nickel oxide concentration values were between 0.003 wt% and 0.395 wt%, with samples 328 (depth in ft.) and QV 128 being the highest and lowest values, respectively (s.d., 0.0978), with a mean value of 0.134 wt%. Phosphorous oxide concentration values were between 0.139 wt% and 0.248 wt%, with samples QV 121 and 325 (depth in ft.) being the highest and lowest values, respectively (s.d., 0.0349), with a mean value of 0.175 wt%. Silicon dioxide concentration values were between 21.1 wt% and 52.7 wt%, with samples QV 128 and QV 122 being the highest and lowest values, respectively (s.d., 6.821), with a mean value of 36.1 wt%. Titanium dioxide concentration values were between 0.437 wt% and 2.56 wt%, with samples CSW 17.2 and QV 135 being the highest and lowest values, respectively (s.d., 0.5825), with a mean value of 0.844 wt%. Concentration and standard calibration, dilutions, blank, corrections, and drift are in appendix. Magnesium oxide values were plotted against silicon dioxide values to geochemically infer tectonic setting. There is great variability amongst the samples, particularly in the MgO and SiO2 values (Figure 107) showing the placement of various geochemically derived tectonic settings associated with ophiolites. Values are sparsely located but

fall generally in a depleted silica and enriched magnesium zone. Few points plot in the supra-subduction zone (SSZ) is backarc to forearc (Backarc to Forearc), forearc (SSZ Forearc), oceanic backarc (SSZ Oceanic Backarc), and continental backarc (SSZ Continental Backarc). Mean values plot in a significantly lower silica zone than these representative types.

4.4 Electron Microprobe Analysis

Four samples from the M81-313 Homestake core at McLaughlin were analyzed via Electron Microprobe Analysis for the major elements (Al, Ca, Cr, Fe, K, Mg, Mn, Na, Ni, P, Si, Ti) of specific mineral grains (Tables 5-8). These values were obtained in weight percent oxides and were converted to atomic cation values (Table 7). Major mineral chemistry from relict peridotite mineral grains from the Coast Range ophiolite, California spanning a surface sample (McL-surface), and three M81-313 cores (McL-239A, McL-329, and McL-356) of olivine, clinopyroxene, spinel, andradite garnet, and orthopyroxene have limited input from volatiles based on the total weight % values. Further examination of olivine and spinel were performed.

4.4.1 Olivine

Olivine was identified by the high relief crystal structure and the zonation of metamorphism to serpentine, and characterized using energy dispersive spectroscopy (EDS). Olivine (N=7, point analyses on McL_329) exhibited an aluminum oxide concentration values between 0.00 wt% and 5.89 wt%, (s.d., 2.05), with a mean value of 5.89 wt%. Calcium oxide concentration values were between 0.01 wt% and 0.02 wt%, (s.d., 0.0090), with a mean value of 0.0257 wt%. Chromium oxide concentration values were between 0.02 wt% and 0.86 wt%, (s.d., 0.2987), with a mean value of

0.12 wt%. Iron oxide concentration values were between 3.65 wt% and 23.73 wt%, (s.d., 6.126), with a mean value of 10.3 wt%. Potassium oxide concentration values were between 0.0 wt% and 0.02 wt%, (s.d., 0.00452), with a mean value of 0.0257 wt%. Magnesium oxide concentration values were between 24.3 wt% and 49.2 wt%, (s.d., 8.842), with a mean value of 43.1 wt%. Manganese oxide concentration values were between 0.03 wt% and 0.4 wt% (s.d., 0.1118), with a mean value of 0.151 wt%. Sodium oxide concentration values were between 0.0 wt% and 0.02 wt%, with (s.d., 0.007), with a mean value of 0.0043 wt%. Nickel oxide concentration values were between 0.04 wt% and 0.47 wt%, (s.d., 0.1322), with a mean value of 0.354 wt%. Sulfur dioxide concentration values were between 0.0 wt% and 0.03 wt%, (s.d., 0.0116), with a mean value of 0.017 wt%. Silicon dioxide concentration values were between 34.7 wt% and 43.7 wt%, (s.d., 2.552), with a mean value of 40.5 wt%. Titanium dioxide concentration values were between 0.0 wt% and 0.17 wt% (s.d., 0.0257), with a mean value of 0.026 wt%. The mean calculated values of forsterite (Fo) and fayalite (Table 9) are $Fo_{87.4}$ and $Fa_{12.6}$, slightly enriched in fayalite with respect to mean Earth olivines.

4.4.2 Clinopyroxene

Clinopyroxene (N=3, point analyses on McL_239A) was identified in one of four samples using cleavage, relief, crystal structure showing laminae, and EDS. Clinopyroxene exhibited an aluminum oxide concentration values between 0.00 wt% and 0.01 wt%, (s.d., 0.00471), with a mean value of 0.007 wt%. Calcium oxide concentration values were between 14.5 wt% and 19.1 wt%, (s.d., 1.9435), with a mean value of 16.4 wt%. Chromium oxide concentration values were between 0.0

wt% and 0.02 wt%, (s.d., 0.0.00943), with a mean value of 0.007 wt%. Iron oxide concentration values were between 13.47 wt% and 13.76 wt%, (s.d., 0.12223), with a mean value of 13.6 wt%. Potassium oxide concentration values were between 0.05 wt% and 0.13 wt%, (s.d., 0.03559), with a mean value of 0.1 wt%. Magnesium oxide concentration values were between 12.6 wt% and 16.9 wt%, (s.d., 2.0508), with a mean value of 14.0 wt%. Manganese oxide concentration values were between 0.25 wt% and 0.45 wt% (s.d., 0.08219), with a mean value of 0.357 wt%. Sodium oxide concentration values were between 0.5 wt% and 0.7 wt%, with (s.d., 0.03560), with a mean value of 0.5 wt%. Nickel oxide concentration values were between 0.0 wt% and 0.02 wt%, (s.d., 00943), with a mean value of 0.007 wt%. Sulfur dioxide concentration across any of the clinopyroxene was not reported. Silicon dioxide concentration values were between 47.41 wt% and 50.62 wt%, (s.d., 1.4000), with a mean value of 48.7 wt%. Titanium dioxide concentration values were between 0.6 wt% and 2.3 wt% (s.d., 0.7930), with a mean value of 1.21 wt%.

4.4.3 Spinel

Spinel, $MgAl_2O_4$, (N=10-point analyses on McL_329) was identified by using energy dispersive spectroscopy (EDS). Spinel exhibited an aluminum oxide concentration values between 53.1 wt% and 57.7 wt%, (s.d., 1.201), with a mean value of 56.1 wt%. Calcium oxide concentration values were between 0.0 wt% and 0.04 wt%, (s.d., 0.0129), with a mean value of 0.009 wt%. Chromium oxide concentration values were between 0.49 wt% and 11.6 wt%, (s.d., 0.491), with a mean value of 11.63 wt%. Iron oxide concentration values were between 11.7 wt% and 13.5 wt%, (s.d., 0.670), with a mean value of 12.6 wt%. Potassium oxide concentration values

were between 0.0 wt% and 0.01 wt%, (s.d., 0.00471), with a mean value of 0.003 wt%. Magnesium oxide concentration values were between 18.7 wt% and 20.6 wt%, (s.d., 0.558), with a mean value of 19.2 wt%. Manganese oxide concentration values were between 0.1 wt% and 0.16 wt% (s.d., 0.00166), with a mean value of 0.141 wt%. Sodium oxide concentration values were between 0.0 wt% and 0.02 wt%, with (s.d., 0.008), with a mean value of 0.007 wt%. Nickel oxide concentration values were between 0.33 wt% and 0.37 wt%, (s.d., 0.1342), with a mean value of 0.345 wt%. Sulfur dioxide concentration values were between 0.0 wt% and 0.01 wt%, (s.d., 0.0041), with a mean value of 0.022 wt%. Silicon dioxide concentration values were between 0.02 wt% and 0.06 wt%, (s.d., 0.0063), with a mean value of 0.05 wt%. Titanium dioxide concentration values were between 0.04 wt% and 0.06 wt% (s.d., 0.00629), with a mean value of 0.05 wt%.

4.4.4 Andradite Garnet

Andradite garnet, $Ca_3Fe_2Si_3O_{12}$, (N=3-point identifications, one at McL_356 and two on the surface, McL_surface) was identified by using energy dispersive spectroscopy (EDS). Andradite garnet exhibited an aluminum oxide concentration values between 1.18 wt% and 1.98 wt%, (s.d., 0.3659), with a mean value of 1.46 wt%. Calcium oxide concentration values were between 31.7 wt% and 33.2 wt%, (s.d., 0.671), with a mean value of 32.7 wt%. Chromium oxide concentration values were between 0.43 wt% and 2.16 wt%, (s.d., 0.7172), with a mean value of 1.46 wt%. Iron oxide concentration values were between 13.5 wt% and 24.2 wt%, (s.d., 4.659), with a mean value of 20.0 wt%. Potassium oxide concentration across any of the andradite garnet was not reported. Magnesium oxide concentration values were between 0.09

wt% and 0.93 wt%, (s.d., 0.3766), with a mean value of 0.40 wt%. Manganese oxide concentration values were between 0.04 wt% and 0.12 wt% (s.d., 0.0334), with a mean value of 0.07 wt%. Sodium oxide concentration values were between 0.0 wt% and 0.02 wt%, with (s.d., 0.009), with a mean value of 0.007 wt%. Nickel oxide concentration values were between 0.0 wt% and 0.01 wt%, (s.d., 0.005), with a mean value of 0.007 wt%. Sulfur dioxide concentration values were between 0.0 wt% and 0.01 wt%, (s.d., 0.0041), with a mean value of 0.003 wt%. Silicon dioxide concentration values were between 27.6 wt% and 34.2 wt%, (s.d., 3.0764), with a mean value of 32.0 wt%. Titanium dioxide concentration values were between 0.95 wt% and 11.5 wt% (s.d., 4.713), with a mean value of 5.0 wt%.

4.4.5 Orthopyroxene

Orthopyroxene was identified by using energy dispersive spectroscopy (EDS) at McL_239A (N= 3-point identifications). Orthopyroxene exhibited an aluminum oxide concentration values between 2.36 wt% and 5.26 wt%, (s.d., 0.0047), with a mean value of 3.65 wt%. Calcium oxide concentration values were between 14.5 wt% and 19.1 wt%, (s.d., 1.944), with a mean value of 16.4 wt%. Chromium oxide concentration values were between 0.0 wt% and 0.01 wt%, (s.d., 0.005), with a mean value of 0.007 wt%. Iron oxide concentration values were between 13.5 wt% and 13.8 wt%, (s.d., 0.1222), with a mean value of 13.6 wt%. Potassium oxide concentration values were between 0.05 wt% and 0.13 wt%, (s.d., 0.0356), with a mean value of 0.10 wt%. Magnesium oxide concentration values were between 12.6 wt% and 17.0 wt%, (s.d., 2.051), with a mean value of 14.0 wt%. Manganese oxide concentration values were between 0.25 wt% and 0.45 wt% (s.d., 0.0822), with a mean value of 0.36

wt%. Sodium oxide concentration values were between 0.39 wt% and 0.70 wt%, with (s.d., 0.1417), with a mean value of 0.5 wt%. Nickel oxide concentration values were between 0.0 wt% and 0.02 wt%, (s.d., 0.0094), with a mean value of 0.007 wt%. Sulfur dioxide concentration values across any of the orthopyroxenes was not reported. Silicon dioxide concentration values were between 47.4 wt% and 51.0 wt%, (s.d., 1.4000), with a mean value of 48.7 wt%. Titanium dioxide concentration values were between 0.0 wt% and 0.02 wt% (s.d., 0.0094), with a mean value of 1.2 wt%.

4.4.6 Serpentine

Serpentine was identified by using energy dispersive spectroscopy (EDS) at McL_356, McL_329, and McL_surface (N=55-points of identification). Serpentine exhibited an aluminum oxide concentration values between 0.0 wt% and 8.8 wt%, (s.d., 2.338), with a mean value of 2.62 wt%. Calcium oxide concentration values were between 0.0 wt% and 0.2 wt%, (s.d., 0.0375), with a mean value of 0.06 wt%. Chromium oxide concentration values were between 0.0 wt% and 4.63 wt%, (s.d., 0.7052), with a mean value of 0.4 wt%. Iron oxide concentration values were between 2.4 wt% and 12.7 wt%, (s.d., 2.708), with a mean value of 7.0 wt%. Potassium oxide concentration values were between 0.0 wt% and 0.02 wt%, (s.d., 0.007), with a mean value of 0.007 wt%. Magnesium oxide concentration values were between 30.0 wt% and 40.5 wt%, (s.d., 2.569), with a mean value of 35.8 wt%. Manganese oxide concentration values were between 0.0 wt% and 0.39 wt% (s.d., 0.0653), with a mean value of 0.12 wt%. Sodium oxide concentration values were between 0.0 wt% and 0.05 wt%, with (s.d., 0.1189), with a mean value of 0.007 wt%. Nickel oxide concentration values were between 0.0 wt% and 0.52 wt%, (s.d., 0.1529), with a mean

value of 0.14 wt%. Sulfur dioxide concentration values were between 0.0 wt% and 0.6 wt%, (s.d., 0.086), with a mean value of 0.04 wt%. Silicon dioxide concentration values were between 33.9 wt% and 44.1 wt%, (s.d., 2.010), with a mean value of 40.2 wt%. Titanium dioxide concentration values were between 0.0 wt% and 0.61 wt% (s.d., 0.1560), with a mean value of 0.08 wt%.

Geochemical Plots of CRO Rocks

The MgO vs SiO_2 plot (Figure 42) shows geochemically-derived signatures of tectonic settings associated with ophiolites and how these are related to CRO McLaughlin rocks. Values are sparsely located but fall generally in a depleted silica and enriched magnesium zone. Few points plot in the supra-subduction zone (SSZ), backarc to forearc (Backarc to Forearc), forearc (SSZ Forearc), oceanic backarc (SSZ Oceanic Backarc), and continental backarc (SSZ Continental Backarc), which are mean values from Dilek & Furnes (2011). Mean values plot in a significantly lower silica zone than these representative types. Furthermore, these samples also plot lower in silica than depleted mantle (Depleted Mantle) and mantle plume. The MgO vs TiO_2 plot shows the placement of various geochemically derived tectonic settings associated with ophiolites. Values are sparsely located but fall in two generalized patters. The supra-subduction zone (SSZ), backarc to forearc (Backarc to Forearc), forearc (SSZ Forearc), oceanic backarc (SSZ Oceanic Backarc), and continental backarc (SSZ Continental Backarc) are defined by mean values in Dilek & Furnes (2011). CRO values of samples QV 135, 337, QV 137, 326, QV 137.1, 335 all plot near the primitive mantle zone and other samples plot above the SSZ Forearc and populate regions of the backarc to forearc (Backarc to Forearc), forearc (SSZ Forearc),

oceanic backarc (SSZ Oceanic Backarc), and continental backarc (SSZ Continental Backarc). Spinel and Fo (Figure 43) content of coexisting olivine showing major zones of abyssal peridotites and supra-subduction zone peridotites from Choi et al. (2008). CRO rocks from McLaughlin plot variably, with few samples plotting in the abyssal peridotite zone.

4.5 Geochemical Modeling

Mélange terrains exhibiting olivine minerals with major element distributions in the high Mg, moderate Fe wt. % (CRO rocks and lherzolitic shergottite Mars Nili Fossae analog) react with different chemical compositions of seawater analogs generate serpentinization with different proportions of mineralogical, fluid, and pH values. Across all modeled scenarios, pH values were basic, with values between ~8.6 and ~12.1, which is consistent with other works and builds on the thermodynamic modeling of Oze and Sharma (2005). The changing of the initial rock assemblage from Coast Range Ophiolite ultramafics and Martian lherzolite meteorites was monitored to evaluate how the abundance of mineralogical and activity of aqueous species change through the reaction progress. In addition, using the temperature regime of 273 K and 373 K enabled tracking the mineralogy and fluid composition in temperature end members to evaluate the effect temperature plays in the species present through the reaction progress and at equilibrium. The changing seawater chemistries provides insight into how seawater major element chemistries effect the speciation of specific astrobiological aqueous species and how minerals persist through the reaction progress. These results were interpreted finally in the context of hyperspectral imaging available on Mars from the orbital data.

Initial solid-phase inputs

Rigorous data for specific major element compositions in Nili Fossae rocks are not available. Therefore, it is useful to reference Mars lherzolite meteorites, which are hypothesized to be mantle-derived meteorites sourced from Mars. The mean major element values of olivine from lherzolitic shergottites (Y000027, Y000047, and Y000097; Mikouchi & Kurihara, 2008) were used to determine reasonable Mars olivine analogs. MgO values utilized were 35 wt%, CaO 0.29 wt%, MnO 0.55 wt%, FeO 26.2 wt%, SiO_2 37.6 wt%. Other values were imputed as below detection limit for the EMP analysis (10^{-9} wt%). CRO olivines were modeled as mean major element values obtained in the EMP analysis.

Initial seawater inputs

Terrestrial-based seawaters reaction were constrained by two boundary conditions; temperature (273 K and 373 K) and pressure schemes (1 bar and 75 bar). The water to rock ratios were constrained as 1:10, 1:1, and 10:1. The seawater chemistry is based on modeling computations with carbon dioxide partial pressure fugacity of 0.0057 and an oxygen partial pressure fugacity 0.000876, representing the Martian major atmospheric constituents important in this modeling calculated through the partial pressures based on pressure from De Pater and Lissauer (2015). For CRO habitability in Earth-based rocks, seawater ocean is based on modeling computations with carbon dioxide partial pressure of 0.0003, averaged from ocean chemistry (Hem, 1985).

Serpentinization of CRO olivine with Na-Cl Seawater

The CRO olivine reacting with Na-Cl seawater solution generated methane aqueous species value of 44.50 mg/kg solution at 373 K (Figure 57). Reactions were also modeled for the seawater solution at 273.15K for the entire reaction, a temperature common on Mars' surface and a methane aqueous species value of 42.83 mg/kg sol (Figure 56). Indicating that CRO olivine deposits that underwent serpentinization would have produced more methane if the olivine was reacting with a higher system temperature, either higher fluid or a higher mineral reactant temperature. Major mineralogies produced in both simulations was antigorite, magnetite, and brucite, with minor amounts of greenalite and tephroite, and many possible minerals in abundance of less than .1% weight percent abundance.

Serpentinization of olivine lherzolitic shergottites with Na-Cl Seawater

For mean olivine lherzolitic shergottites reacting with the model Na-Cl seawater (Figure 60), results in aqueous methane at 41.46 mg/kg solution, with a log methane activity of -2.5707 at 273 K. Aqueous hydrogen was 1153 mg/kg sol, with a log activity of -0.258. Gases were also produced, resulting in H_2 gas and CH_4 gases being the dominant species with a fugacity of 607.2 and 1.033, respectively. Major mineralogical species (Figure 62) produced in the reaction from highest abundance to lowest were antigorite, magnetite, FeO-bearing phase, magnetite, greenalite ($(Fe^{2+},Fe^{3+})_{2-3}Si_2O_5OH_4$), manganese brucite ($Mn(OH)_2$), and andradite garnet ($Ca_3Fe_2(SiO4)_3$). For mean olivine lherzolitic shergottites reacting with the model Na-Cl seawater at 373 K (Figure 61), results show aqueous methane at 41.59 mg/kg solution, with a log methane activity of -2.5689. Aqueous hydrogen was 1865 mg/kg sol, with a log activity of -0.0164. Gases were also produced, resulting in H_2 gas and

CH_4 gases being the dominant species with a fugacity of 1206 and 3.085, respectively. Major mineralogical species (Figure 63) produced in the reaction from highest abundance to lowest were antigorite, magnetite, FeO-bearing phase, magnetite, tephroite (Mn_2SiO_4), greenalite ($(Fe^{2+}, Fe^{3+})_{2-3}Si_2O_5OH_4$), and andradite garnet ($Ca_3Fe_2(SiO4)_3$). This suggests that mélange terrain olivine, reacting with Na-Cl based on lherzolitic olivine rock deposits that undergo serpentinization, would have produced more methane if the olivine was reacting with seawater at higher temperatures. Manganese brucite is only produced in the lower-temperature serpentinization system at 273 K.

Serpentinization of olivine lherzolitic shergottites with Ca-Cl Seawater

For mean olivine lherzolitic shergottites reacting with the model Ca-Cl seawater (Figure 64), results show aqueous methane at 41.47 mg/kg solution, with a log methane activity of -2.5770 at 273 K. Aqueous hydrogen was 1179 mg/kg sol, with a log activity of -0.2225. Gases were also produced, resulting in H_2 gas and CH_4 gases being the dominant species with a fugacity of 611.8 and 1.018, respectively. Major mineralogical species (Figure 66) produced in the reaction from highest abundance to lowest were antigorite, magnetite, FeO-bearing phase, magnetite, greenalite ($(Fe^{2+},Fe^{3+})_{2-3}Si_2O_5OH_4$), manganese brucite ($Mn(OH)_2$), and andradite garnet ($Ca_3Fe_2(SiO4)_3$). For mean olivine lherzolitic shergottites reacting with the model Ca-Cl seawater at 373 K (Figure 65), results show aqueous methane at 41.61 mg/kg solution, with a log methane activity of -2.5752. Aqueous hydrogen was 1907 mg/kg sol, with a log activity of -0.0133. Gases were also produced, resulting in H_2 gas and CH_4 gases being the dominant species with a fugacity of 1214 and 3.041,

respectively. Major mineralogical species (Figure 67) produced in the reaction from highest abundance to lowest were antigorite, magnetite, FeO-bearing phase, magnetite, tephroite (Mn_2SiO_4), greenalite ($(Fe^{2+}, Fe^{3+})_{2-3}Si_2O_5OH_4$), and andradite garnet ($Ca_3Fe_2(SiO4)_3$). This suggests that mélange terrain olivine, reacting with Ca-Cl based on lherzolitic olivine rock deposits that undergo serpentinization, would have produced more methane if the olivine was reacting with seawater at higher temperatures. Manganese brucite is only produced in the lower-temperature serpentinization system, as in the Na-Cl seawater system.

Serpentinization of olivine lherzolitic shergottites with Mg-Cl Seawater

For mean olivine lherzolitic shergottites reacting with the model Mg-Cl seawater (Figure 68), results show aqueous methane at 41.46 mg/kg solution, with a log methane activity of -2.5820 at 273 K. Aqueous hydrogen was 1200 mg/kg sol, with a log activity of -0.2196. Gases were also produced, resulting in H_2 gas and CH_4 gases being the dominant species with a fugacity of 615.9 and 1.006, respectively. Major mineralogical species (Figure 70) produced in the reaction from highest abundance to lowest were antigorite, magnetite, FeO-bearing phase, magnetite, greenalite ($(Fe^{2+}, Fe^{3+})_{2-3}Si_2O_5OH_4$), and manganese brucite ($Mn(OH)_2$). For mean olivine lherzolitic shergottites reacting with the model Mg-Cl seawater at 373 K (Figure 69), results in aqueous methane at 41.60 mg/kg solution, with a log methane activity of -2.5802. Aqueous hydrogen was 1941 mg/kg sol, with a log activity of -0.0104. Gases were also produced, resulting in H_2 gas and CH_4 gases being the dominant species with a fugacity of 1222 and 3.006, respectively. Major mineralogical species (Figure 71) produced in the reaction from highest abundance to lowest were

antigorite, magnetite, FeO-bearing phase, magnetite, tephroite (Mn_2SiO_4), and greenalite ($(Fe^{2+}, Fe^{3+})_{2-3}Si_2O_5OH_4$). This suggests that mélange terrain olivine, reacting with Ca-Cl based on lherzolitic olivine rock deposits that undergo serpentinization, would have produced more methane if the olivine was reacting with seawater at higher temperatures, and the production of andradite is not present in the Mg-Cl seawater reactions.

Bioenergetic Modeling

Bioenergetic modeling (as in Amend and Shock, 2001; Cardace et al., 2015) was based on from outputs from Geochemist's Workbench REACT modeling, and leveraged the Gibbs Free Energy equation of the methanogenesis (MG) and methanotrophy (MT) reactions, $CO_{2(aq)} + 4H_{2(aq)} = CH_{4(aq)} + 2H_2O_{(l)}$ and $CH_{4(aq)} + 2H_2O_{(l)} = CO_{2(aq)} + 4H_{2(aq)}$, respectively. MG was favored ($\Delta G_r<0$) across all conditions. MT favorability was variable, with more negative ΔG_r values resulting from reaction of model rock with Mg-Cl type ocean. In general, the low temperature, 273 K system exhibited early reaction spontaneity with respect to the system at 373 K which initial reaction thermodynamics results in the starting conditions being favorable.

Bioenergetic modeling at 273 K and 373 K Coast Range Ophiolite and Na-Cl seawater systems of MG (Figure 72) and MT (Figure 73) using the Gibbs Free Energy equation of the MG reaction being less favorable early in the reaction progress and MT was more favored, relative to MG, early in the reaction progress, with both bioenergetic pathways reaching equilibrium at approximately -200 kJ/mol. At

Xi=0.2000, the colder temperature, 273 K, became more favorable than the higher 373 K temperature, in MG.

Bioenergetic modeling at 273 K and 373 K Martian lherzolite shergottite and Na-Cl seawater systems of MG (Figure 74) and MT (Figure 75) using the Gibbs Free Energy equation of the MG reaction being less favorable early in the reaction progress and MT was more favored, relative to MG, early in the reaction progress, with both bioenergetic pathways reaching equilibrium at approximately -200 kJ/mol. At Xi=0.2000, the colder temperature, 273 K, became more favorable than the higher 373 K temperature. Between the 273 K and 373 K Martian lherzolite shergottite reaction with Ca-Cl seawater, the MG reaction (Figure 76) was less thermodynamically favored early in the reaction progress with respect to MT (Figure 77) and both bioenergetic pathways reached equilibrium at approximately -200 kJ/mol. The specific temperatures, 273 K and 373 K, had different minimum and maximum Gibbs Free Energy values, with the warmer temperature, 373 K, being more favorable for both MG and MT. The modeling at 273 K and 373 K Martian lherzolite shergottite and Mg-Cl seawater systems using the Gibbs Free Energy equation of the MG (Figure 78) reaction being less favorable early in the reaction progress and MT (Figure 79) was more favored, relative to MG, early in the reaction progress, with both bioenergetic pathways teaching equilibrium at approximately -200 kJ/mol. The specific temperatures, 273 K and 373 K, had different minimum and maximum Gibbs Free Energy values, with 373 K being more favorable for both MG and MT in the Mg-Cl system, also.

5. DISCUSSION

5.1 McLaughlin Natural Reserve Mélange Terrain: ultramafic rock provenance puzzle

Expanses of ophiolite sequences span diverse spatial and temporal settings that are associated with major orogenies and the exact nature of the specific tectonic and magmatic formation of ophiolites and, more broadly oceanic lithosphere, has been investigated structurally, stratigraphically, and geochemically (see Dilek & Furnes (2011) for a comprehensive review on ophiolites). Ophiolites have two major generalized geodynamic formation strategies, pathways that are subduction related and those that are not subduction related. Tracing the geodynamic source and degree of structural and metamorphic alteration can be complex, requiring multiple lines of evidence to decouple ophiolite phenomena and provide more resolution to these events. Using the evolution of the physical condition of these units across space and time, through structural and stratigraphic relationships, coupled with analog comparisons of rock geochemistry, one can establish the specific tectonic and magmatic processes that plausibly explain a given serpentinite site. Processes tied to ophiolite formation/emplacement and subsequent alteration through time all contribute to modern rock geochemistry. In California, the Coast Range Ophiolite has been well studied, through structural, stratigraphic, and geochemical signatures over the past four decades, investigating the underlying geodynamics of the Coast Range Ophiolite is still controversial. Through this thesis, application of multiple geochemical metrics for determining provenance of ultramafic rocks did not provide a unique interpretation

of the data; a single tectonic setting cannot explain the geochemical diversity observed at the McLaughlin Natural Reserve locality. Prior work has proposed three distinct formation models for the Coast Range Ophiolite. A mid-ocean ridge setting has been based largely on stratigraphy (Hopson et al., 1981), a back-arc basin setting has been based on regional structural geology (Ingersoll, 2000), and a supra-subduction zone setting with active fore-arc spreading has been based on unit-by-unit rock geochemistry (Choi et al., 2008). For this previously undescribed field locality, no single provenance can be argued. However, in broad strokes, Coast Range Ophiolite samples from the McLaughlin Natural Reserve locality share some geochemical similarity with associated serpentinized peridotites in the region, as determined by the spinel and olivine mineral chemistries. The major elements, determined by ICP-AES suggest a deeper mantle source with the MgO/SiO_2 ratio. The values of MgO suggest a subduction signature with the lower SiO_2 values, as continental margin and mid-ocean ridge ophiolite systems exhibit SiO_2 values between 55 to 70% with MgO values of 0-20% (see Dilek & Furnes, 2011). Based on the MgO/SiO_2 ratio, the ultramafic source indicates a heterogenous mantle source through the different samples. One point of future work will include determining the silca loss associated with the serpentinization process and determine the amount of silica loss on determining the geodynamics of serpentinized ultramafic hosted rock units in mélange settings. Although tectonics-based research has suggested island arc petrogenesis (Choi et al. 2008), and prior work on serpentinized ultramafic units has suggested a supra-subduction setting (Choi et al. 2008), new data from this study suggest that McLaughlin Natural Reserve locality ultramafics are SiO_2-poor and MgO-enriched, thus suggesting depleted mantle source

and/or mantle plume. Further geochemical analysis and modeling resolution are required to determine the mantle source. A broader sample set could provide richer data for the major element and REE chemistry to clarify whether these rocks have a greater affinity for island arc or supra-subduction zone tectonic settings, or whether they represent a chaotically mixed landscape that integrates rocks of similar mineralogy but sourced from discrete tectonic settings. Future work on the subsurface at the CROMO site is also required, using structural and near-surface geophysical techniques to better characterize the subsurface habitability of mélange terrain

5.2 Serpentinization-fueled Habitability of CRO and Nili Fossae ultramafics: variable through time, and reliant on planetary ocean chemistry

CRO through time

CRO, Jurassic age emplaced oceanic lithosphere, has been reacting with Na-Cl seawater resulting in heavily serpentinized peridotite. Model results for the reaction of CRO olivine with terrestrial ocean (Na-Cl type ocean) show that through time, more olivine reacts with the terrestrial ocean, resulting in a habitable environment for methanotrophic organisms. Microbial life that undergoes methanogenesis and methanotrophy would have spontaneous metabolic biochemistries in the water-rock conditions modeled. The Coast Range Ophiolite and Na-Cl seawater systems of MG (Figure 72) and MT (Figure 73) distinct habitability changes occur in the rocks, as represented by the minerals present such that when the system transitions between 0.1 and 0.3 Xi, the mineral phases present decrease and the mineral wt% plateaus, increasing only very slightly towards equilibrium. This is marked in the 373 K simulation with the production and dissolution of hematite. Antigorite, magnetite, and

brucite are the major mineral species in both simulated temperature regimes with minor amounts of greenalite and tephroite. The lack of observed brucite in thin sections and XRD results at CROMO can indicate the section of ophiolite is located in a zone where there has been continued hydrothermal fluid interaction, resulting in complete serpentinization, leaving only serpentine and magnetite (Sonzogni et al., 2017) or the chemical weathering of brucite out of the CRO rocks, transforming both talc and brucite to more serpentine minerals (Bach et al., 2004). Thus, the degree of serpentinization in the CRO ultramafics, the initial mineralogical compositions of the rock unit, the physical and chemical parameters of the reaction fluid, and the presence of secondary reactions such as reactions containing brucite, magnetite, and hydrogen, control serpentinite localized habitability. The components in the fluid as highlighted by the selected aqueous phases pertinent to methane cycling organisms, shows a stable path to equilibrium after 0.2 Xi. When fayalite and forsterite undergo serpentinization, the products of serpentine group minerals and magnetite, there is the production of hydrogen in both the 273 K (Figure 72) and 373 K (Figure 73), and is the dominant aqueous phase in the fluid, relevant to methanotrophs and methanogens. The Gibbs Free Energy at 273 K and 373 K Coast Range Ophiolite and Na-Cl seawater systems of MG (Figure 72) and MT (Figure 73) follows the pattern of the aqueous species activities from which the Gibbs Free Energy values were derived. The MT reaction in the 273 K reaction system is more favorable than the reaction at 373 K, but the reaction favorability quickly changes beyond 0.1 Xi, having initially very favorable Gibbs Energy values reported at ~-375 kJ/mol, early in the reaction progress, with both bioenergetic pathways reaching equilibrium at approximately -200 kJ/mol. MG

starts the reaction progress at Xi=0.0, at ~-20 kJ/mol and ~-45 kJ/mol in the 373 K and 273 K systems. The favorability changes for the 273 K system where at Xi=0.10, the system decreases in favorability for MG to a Gibbs Free Energy value of ~-25 kJ/mol and subsequently the 373 K becomes more favorable at ~-45 kJ/mol. Both temperature bioenergetic pathways reaching equilibrium at approximately -190 kJ/mol. The CRO McLaughlin Reserve site is like most continental serpentinizing systems, such that it occurs at lower temperatures >473 K. For methanogenesis, lower temperatures beneath 373 K are more thermodynamically favorable and methanotrophy is more favored in the 373 K temperature, versus the 273 K system. The low temperature fluid causing the ongoing serpentinization at the CRO site is likely distinct from the modeled terrestrial ocean, such that it has high pH, enrichment in dissolved organic carbon (DOC) and nutrients, with respect to mean terrestrial seawater values (Crespo-Medina et al., 2014). Further work is underway on modeling different ocean chemistries, such as Jurassic and Cretaceous seawater chemistries, and available fluid chemistry from groundwater at CROMO observation wells (Crespo-Medina et al., 2014) to better evaluate the context of the serpentinization of these ultramafic rocks in continental ophiolites. Cretaceous seawater, enriched in Cl^- and Ca^{2+}(Lowenstein et al., 2001), could change the thermodynamics of the ultramafic rock-seawater in the reaction simulations and thus change the habitability of the fluids flowing through the serpentine veins. Future work will also look at the serpentinization at another hypothesized location of the Coast Range Ophiolite, the Cedars ultramafic mass, located in Sonoma, California (Suzuki et al., 2013), specifically the solid-phase geochemistry and mineralogies, in the context of habitability.

Nili Fossae through time (a shergottite-based analysis)

The lherzolitic shergottites reacting with the model Na-Cl seawater at 273 K (Figure 60) and 373 K (Figure 61), results in aqueous and gas production of H_2 and CH_4, with H_2 being the dominant species. The dominant mineralogical species in the 273 K system (Figure 62) produced in the reaction show the production of phyllosilicates of antigorite and greenalite, oxides of magnetite, FeO-bearing phase, manganese brucite, an iron sulfide mineral troilite, and a silicate, andradite garnet. In contrast, the higher temperature simulations (Figure 63) show similar aqueous species activity, the mineralogy changed with respect to the oxide manganese brucite, where tephroite, the manganese olivine variety was thermodynamically favored. This suggests that tephroite detection can provide insight in the temperatures of the serpentinization system. Coinciding with the formation of brucite in the 373 K simulation, there is a decrease in the Gibbs Energy values, suggesting the lack of observed brucite results in complete serpentinization, leaving only serpentine and magnetite (Sonzogni et al., 2017) or the thermodynamic favorability of serpentine minerals over brucite in the shergottites, due to the chemical weathering of both talc and brucite to more serpentine minerals (Bach et al., 2004). Aqueous methane produced in the 273 K, 41.46 mg/kg solution and methane produced in the 373 K system 41.59 mg/kg solution suggests lherzolitic olivine rock deposits that undergo serpentinization, would have produced more methane if the olivine was reacting with seawater at higher temperatures. Furthermore, aqueous hydrogen production also increased between the 273 K and 373 K system from 1153 mg/kg solution to 1865 mg/kg solution, respectively. In the gas phase, the fugacity of hydrogen nearly

doubled in the changing temperature regime, with 273 K hydrogen gas having a fugacity of 607.2 and the 373 K hydrogen gas having a fugacity of 1206. Methane gas released also increased in fugacity between the 273 K and 373 K system, going from a methane fugacity of 1.033 to 3.085, respectively. Bioenergetic modeling at 273 K and 373 K Martian lherzolite shergottite and Na-Cl seawater systems of MG (Figure 74) and MT (Figure 75) using the Gibbs Free Energy equation of the MG reaction being less favorable early in the reaction progress and MT was more favored, relative to MG, early in the reaction progress, with both bioenergetic pathways reaching equilibrium at approximately -200 kJ/mol. At Xi=0.2000, the colder temperature, 273 K, became more favorable than the higher 373 K temperature.

The lherzolitic shergottites reacting with the model Ca-Cl seawater at 273 K (Figure 64) and 373 K (Figure 65), results in aqueous and gas production of H_2 and CH_4, with H_2 being the dominant species, like the Na-Cl seawater reaction. The dominant mineralogical species in the 273 K system (Figure 66) produced in the reaction show the production of phyllosilicates of antigorite and greenalite, oxides of magnetite, FeO-bearing phase, manganese brucite, an iron sulfide mineral troilite, and a silicate, andradite garnet. In contrast, the higher temperature simulations (Figure 67) show similar aqueous species activity, the mineralogy changed with respect to the oxide manganese brucite, where tephroite, the manganese olivine variety was thermodynamically favored, which is also is exhibited in the Na-Cl seawater reaction systems. Aqueous methane produced in the 273 K system, 41.47 mg/kg solution, and in the 373 K system 41.61 mg/kg solution, and aqueous hydrogen produced in the 273 K system, 1179 mg/kg solution, and 373 K system, 1907 mg/kg solution, suggests

lherzolitic olivine rock deposits that undergo serpentinization in a Ca-Cl seawater, would have produced more methane and hydrogen if the olivine was reacting with seawater at higher temperatures, as in the Na-Cl seawater system. As in the Na-Cl seawater system, the fugacity of hydrogen increased in the changing temperature regime, with 273 K hydrogen gas having a fugacity of 611.8 and the 373 K hydrogen gas having a fugacity of 1214. Methane gas released also increased in fugacity between the 273 K and 373 K system, going from a methane fugacity of 1.018 to 3.041, respectively, which is less than the Na-Cl system. This could be due to the thermodynamic favorability of the aqueous system being a preferred phase for hydrogen and methane in the Ca-Cl seawater system. Gibbs Free Energy values between the 273 K and 373 K Martian lherzolite shergottite reaction with Ca-Cl seawater, the MG reaction (Figure 76) was less thermodynamically favored early in the reaction progress with respect to MT (Figure 77) and both bioenergetic pathways reached equilibrium with the 273 K system being ~40 kJ/mol less than the 373 K system. Since there is more aqueous activity in the 373 K, the increased favorability is expected.

The lherzolitic shergottites reacting with the model Mg-Cl seawater at 273K (Figure 68) and 373K (Figure 69), results in aqueous and gas production of H2 and CH4, with H2 being the dominant species, like the Na-Cl seawater reaction. The dominant mineralogical species in the 273K system (Figure 70) produced in the reaction show the production of phyllosilicates of antigorite and greenalite, oxides of magnetite, FeO-bearing phase, manganese brucite, and iron sulfide mineral troilite. Notably, brucite is not thermodynamically favorable across the entire reaction at 273

K. In the higher temperature simulations (Figure 71) show similar aqueous species activity, the mineralogy changed with respect to tephroite, the manganese olivine variety was thermodynamically favored, which is also is exhibited in the Na-Cl and Mg-Cl seawater reaction systems. Aqueous methane produced in the 273K system, 41.46 mg/kg solution, and in the 373K system 41.60 mg/kg solution, and aqueous hydrogen produced in the 273K system, 1200 mg/kg solution, and 373K system, 1941 mg/kg solution, suggests lherzolitic olivine rock deposits that undergo serpentinization in a Mg-Cl seawater, would have produced more methane and hydrogen if the olivine was reacting with seawater at higher temperatures, as in the other seawater system. As in the other seawater system, the fugacity of hydrogen increased in the changing temperature regime, with 273K hydrogen gas having a fugacity of 615.9 and the 373K hydrogen gas having a fugacity of 1222. Methane gas released also increased in fugacity between the 273K and 373K system, going from a methane fugacity of 1.006 to 3.006, respectively. The modeling at 373 K Martian lherzolite shergottite and Mg-Cl seawater systems using the Gibbs Free Energy equation of the MG (Figure 78) early on in the reaction progress (>0.1= Xi) is unfavorable at 373 K transitioning to habitable to ~-225 kJ/mol. MT (Figure 79) was more favored, relative to MG, early in the reaction progress, with both bioenergetic pathways reaching equilibrium at approximately -200 kJ/mol, from starting at -375 kJ/mol for the 273 K system and ~-450 kJ/mol for the 373 K system. The specific temperatures, 273 K and 373 K, had different minimum and maximum Gibbs Free Energy values, with 373 K being more favorable for both MG and MT in the Mg-Cl system, also.

Overall, the Gibbs Free Energy modeling (as in Amend and Shock, 2001; Cardace et al., 2015) of the metabolic equations of the methanogenesis (MG) and methanotrophy (MT) reactions, $CO_{2(aq)} + 4H_{2(aq)} = CH_{4(aq)} + 2H_2O_{(l)}$ and $CH_{4(aq)} + 2H_2O_{(l)} = CO_{2(aq)} + 4H_{2(aq)}$, showed that MG was favored ($\Delta G_r<0$) across all conditions, which is expected due to the production of hydrogen through the dissolution of fayalite tied to the Fo:Fa values of the olivine in both the CRO ultramafics and the lherzolitic shergottites. MT favorability was variable, with more negative ΔG_r values resulting from reaction of model rock with Mg-Cl type ocean, which is likely influenced by the high Fo values in the initial inputs and the products of the serpentinization reaction, such as the secondary mineral phases of the Mg-phyllosilicates, which dominate the mineralogical systems. In general, the low temperature, 273 K system exhibited early reaction spontaneity with respect to the system at 373 K which initial reaction resulted in the starting conditions being thermodynamically favorable.

A significant difference in the CRO ultramafics and the lherzolitic shergottites is that in the CRO system, the 273 K temperature is more thermodynamically favored with respect to the 373 K system, whereas broadly the 373 K system results in more favorable conditions as the serpentinization reaction progresses toward equilibrium in both MG and MT for the Nili Fossae ultramafic analog of the lherzolitic shergottites.

CONCLUSION

Olivine-bearing mélange terrains in the presence of liquid water can undergo the metamorphic reaction of serpentinization, and thus can generate reliable, long-lived, habitable niches for dark life in a planetary subsurface. Using natural serpentinite samples from the Coast Range Ophiolite, McLaughlin Natural Reserve locality in Lower Lake, CA, I show that new data for surface and sub-surface mineralogy and fine scale geochemical data can serve as appropriate model inputs for evaluation of the habitability of a specific Mars site. This work considers a low-Fe planetary analog to the mélange terrain located in the Syrtis Major quadrangle on Mars: the Nili Fossae. Calculations of the Gibbs free energy available to drive MG and MT in the modeled system show that there is strong drive for MG and MT. Since the serpentinization reaction can, through secondary reaction pathways produce methane, deeper modeling to probe the controls on MG and MT, including identifying threshold levels of ambient methane required to tip the system in MG- or MT-dominant schemes, is needed. The activity of CO_2 may be a factor in the decrease in methanogenesis as CO_2 is the reactant for the particular microbial metabolism considered here.

The surface and near-surface of contemporary Mars is overwhelmingly dry, frozen, oxidized, and irradiated. In the past, Mars likely had habitable conditions that could have had the potential to sustain life (McKay & Stoker 1990; McKay 2010). Between 3.5 and 3 billion years ago in Martian history, encompassing the middle to late Noachian Era and the early Hesperian Era (McKay 1998; McKay 2010), there is evidence that the planet was geologically much more active and had liquid water (Mitchell & Wilson 2003; McKay 2010; Bibring et al. 2006). Evidence of past

geological activity includes abundant volcanism (recall that the planet has the largest volcano in the solar system, Olympus Mons, Mitchell & Wilson, 2003). Having a geologically active planet with vigorous hydrothermal flow may be a necessary condition for origin of life (Martin & Russell 2007; Kargel et al., 2000; McKay 2010), but hydrothermalism is also important for other reasons associated with the existence of life. A geologically active Early Mars would have had ore minerals, some rich in iron and nickel, which would have produced a magnetic field around Mars due to the planetary processing of these metals (Hill & Dessler 1991; Mitchell & Wilson 2003). Early Mar's core was warmer, due to radioactive decay, which generated a more powerful magnetosphere; the higher temperature core would have also caused volcanism and outgassing (Mitchell & Wilson 2003). This magnetosphere preserved the atmosphere (preventing loss, being blown away by cosmic radiation and that atmosphere), and likely eventually led to a warmer and wetter planet (Mitchell & Wilson 2003). Liquid water is also very important to the origin and sustenance of life; water provides the medium for chemical and biochemical reactions that are required for life (Schulze-Makuch et al. 2005). Water was abundant in its liquid phase in various forms such as lakes and small seas early in Mars' history (McKay et al. 1992; Bibringet al. 2006; Bistop et al. 2008). This liquid water, identified by the various lines of evidence exhibited on the surface of Mars—such as the minerals hematite and jarosite, the evidence of sedimentary rocks and strata and the evidence of frozen water, trapped in the ice caps of the polar region (McKay et al. 1992; Bibring et al. 2006; Bistop et al. 2008). With both the hydrothermal vents and geothermal hot springs providing the necessary chemical compounds necessary for life and the geochemical energy to

undergo those reactions, along with liquid water form a conducive environment for the origination of Martian life.

Salts are a significant component of planetary habitability in regolith materials and has been identified on Mars and has been modeled across Mg or Ca dominant cation species with chlorine and sulfate as major anions (Benton et al., 1981; Knauth & Burt, 2002; Chevrier and Valentin, 2012). Focusing on Earth based analogs, Mg, Ca, and Na were modeled to evaluate likely ocean chemistries or groundwater systems as chloride salts have been modeled to represent Mars Reconnaissance Orbiter observations of seasonal slope lineae (Chevrier and Valentin, 2012). The modeled fluids plausible were Mg, Ca, and Na based systems, with eutectic temperatures of Na-Cl at 252.2K, Mg-Cl at 239.5 K, and Ca-Cl at 223.2 K (Chevrier and Valentin, 2012).

The Nili Fossae region contains extensive olivine-rich units with a high percentage of fayalite, relative to Earth based Fo-Fa values (Hoefen et al. 2003). This work shows that the chemical energy driven by serpentinization of specific units in the Martian lithosphere corresponds to enhanced potential for microbial methanogenesis, and to a lesser extent, methanotrophy; both metabolisms were (at least sporadically) thermodynamically favored under modeled conditions. This analysis shows that although the rocks in the Nili Fossae are Noachian (~4 Ga) in age, and evidence of alteration in Martian rocks exists into the early Hesperian (~3.7 Ga) when the salty ocean could have been present on Mars, there is a possibility that brine-seawater salinity groundwater systems are possible, though the likelihood is debated (Michalski et al., 2013). This work shows that if seawater-like ionic solutions existed in the past of are stable in the modern lithosphere, serpentinization-fueled microbial niches, based on

methanogenesis and methanotrophy are feasible. Where altering ultramafic lithologies persist on Mars, habitability is possible. Measurements of methane gas abundance at the Nili Fossae, obtained by the infrared spectrometers on three ground-based telescopes in Hawaii, are in the order of magnitude of ~25-40 ppb (Mumma et al., 2009). At the Nili Fossae, these plumes are associated with the Mars' northern summer near the equator, which can have temperatures as high as 308 K (McEwen et al. 2011; Christensen et al., 2001) indicating the change in Mars' seasonal climate may induce a more thermodynamically favorable environment for the production of gaseous hydrogen and methane through serpentinization, thus effecting seasonal serpentinization-driven habitability. This work also confirms the Nili Fossae as a habitability candidate along with the Hellas Basin, which was investigated in a similar fashion in Oze and Sharma (2005).

Future work will look at impact-driven serpentinization, since the Nili Fossae site is characterized stratigraphically and there are serpentine minerals associated with craters, such as Chia crater (Ehlmann et al., 2010), as this locality shows structural evidence that the Fe-rich olivine was underlain by surface regolith and were then emplaced on the surface of the region by the impactor (Hoefen et al, 2003).

APPENDICES

Appendices: Tables

Major Mineralogical and Aqueous Species involved in Serpentinization	*Reaction Number*
$2(Mg, Fe)_2SiO_4 + 3H_2O = (Mg, Fe)_3Si_2O_5(OH)_4 + Mg(OH)_2$	Reaction 1
$6(Mg, Fe)SiO_3 + 3H_2O = (Mg, Fe)_3Si_2O_5(OH)_4 + (Mg, Fe)_3Si_4O_{10}(OH)$	Reaction 2
$(Mg, Fe)_2SiO_4 + (Mg, Fe)SiO_3 + 2H_2O = (Mg, Fe)_3Si_2O_5(OH)_4$	Reaction 3
$18Mg_2SiO_4 + 6Fe_2SiO_4 + 26H_2O + CO_2 = 12Mg_3Si_2O_5(OH)_4 + 4\,Fe_3O_4 + CH_4$	Reaction 4
$6Fe_2SiO_4+7H_2O=3Fe_3Si_2O_5(OH)4+Fe_3O_4+H_2$	Reaction 5

Table 1: Showing the major reaction involved in serpentinization that result in the production of astrobiologically relevant chemical species.

Major Aqueous Species	***Seawater Na-Cl Ocean[4] mg/kg***	***Mg-Cl Ocean[2] mg/kg***	***Ca-Cl Ocean[3] mg/kg***
Cl-	1.94E+04	1.94E+04	1.94E+04
Na+	1.01E+04	1.08E+03	1.08E+03
SO4--	2.71E+02	2.71E+02	2.71E+02
Mg++	1.29E+03	1.29E+04	1.29E+03
K+	3.90E+02	3.90E+02	3.90E+02
HCO3-	1.40E+02	1.40E+02	1.40E+02
$SiO2_{(aq)}$	5.00E+00	5.00E+00	5.00E+00
Fe++	1.00E-09	1.00E-09	1.00E-09
Mn++	1.00E-09	1.00E-09	1.00E-09
Ni++	1.00E-09	1.00E-09	1.00E-09
Al+++	1.00E-09	1.00E-09	1.00E-09
Ca++	4.11E+02	4.11E+02	4.10E+03
HPO4--	1.00E-09	1.00E-09	1.00E-09
CrO4--	1.00E-09	1.00E-09	1.00E-09
$Ti(OH)4_{(aq)}$	1.00E-09	1.00E-09	1.00E-09
Ti+	1.00E-09	1.00E-09	1.00E-09
SeO3--	1.00E-09	1.00E-09	1.00E-09
Cu++	1.00E-09	1.00E-09	1.00E-09
Zn++	1.00E-09	1.00E-09	1.00E-09
$O2_{(g)}$ *swap* $O2_{(aq)}$	0.200 fugacity	0.000876 fugacity	0.000876 fugacity
$CO2_{(g)}$ *swap* *H+*	-3.50 fugacity	0.0057 fugacity	0.0057 fugacity

Table 2 : Showing the model inputs for the water-rock reactions and habitability.[1] Initial water compositions for Na-Cl ocean were based on Glein et al. (2015) for pH and activity of carbon dioxide ($a_{CO2}=10^{-9}$). [4]The Na-Cl seawater ocean is based on modeling computations with carbon dioxide partial pressure of 0.0003, averaged from ocean chemistry (Hem, 1985). [2] The Mg-Cl ocean is based on Mg values in an Mg brine in an icy-sealed lake in Antarctica (Murray et al., 2012). [3] The Ca-Cl ocean is based on Ca values in a hydrothermal calcium rich brine of Death Valley and Bristol Dry Lake, California (Lowenstein & Risacher, 2009).

Sample	Estimated Rock type	Phase Estimates (vol.%) of Relict & Deformed (retained structure)					% Serpentine	% Relict minerals
		Olivine	Orthopyroxene	Clinopyroxene	Magnetite	Clay	Total	Total
CROMO Surface								
McL_surface	Serp. lherzolite	70	10	No ID	15	5	80	<5
McL_1	Serp. lherzolite	70	10	No ID	10	10	80	<5
McL_2	Serp. lherzolite	75	10	No ID	15	5	85	<5
McL-3	Serp. lherzolite	65	15	5	10	5	85	<5
McL-1 mini core	Serp. lherzolite	65	10	No ID	10	15	75	<5
McL-2 mini core	Serp. lherzolite	75	10	No ID	10	5	85	<5
McL-3 mini core	Serp. lherzolite	75	15	5	5	No ID	90	<5
CROMO Cores								<5
CSW 1,1_10_0-5	Serp. lherzolite	60	10	No ID	5	15	70	<5
CSW 1,1_14_5-8	Serp. lherzolite	60	5	No ID	25	10	65	<5
CSW 1,1_15_12-5	Serp. lhz-hzb*	70	20	No ID	10	No ID	85	5
QV 1,1_122_90-97	Serp. lherzolite	75	5	No ID	15	5	75	5
Homestake Cores								
M81_313_356	Serp. lherzolite	80	10	No ID	10	No ID	55	15
M81_313_239	Serp. lherzolite	70	10	5	10	No ID	52.5	10
M81_313_329	Serp. lherzolite	70	10	5	10	No ID	85	20
Mean Mineralogy								
CROMO Surface	Serp. lherzolite	70.71	11.43	5	10.71	7.5	82.86	>5
CROMO Cores	Serp. lherzolite	66.25	10	No ID	13.75	10	73.75	5
Homestake Cores	Serp. lherzolite	73.33	10	5	10	No ID	64.17	15
	*lhz-hzb=Lherzolite-Harzburgite							

Table 3: Representative thin section analysis of samples in this study showing the three expeditions, hand samples collected at the surface (CROMO surface) which include hand samples and mini-cores at 10cm, subsurface cores down to approximately 35 meters (CROMO cores), and mining cores (Homestake cores) at a maximum depth of 108 meters. Phase estimates were obtained through point counting minerals in the sample using the 2x objective and then confirmed at the 10x objective. The use of a 530-nanometer retardation plate and crossed-polar light was essential to identify minerals.

Sample ID	Major Elements in w.t. %											
	Al 396.152	***Ca 317.933***	***Cr 267.716***	***Fe 259.940***	***K 766.490***	***Mg 285.213***	***Mn 257.610***	***Na 589.592***	***Ni 231.604***	***P 178.229***	***Si 251.611***	***Ti 308.803***
drift1	0.186115	0.805130095	-0.025794729	-1.804798427	-11.07009948	-2.269672441	-0.000314133	-8.284564109	0.037764697	0.044542	-1.997417338	0.258905
Blk-1	0.218894	0.844572406	-0.017219434	-1.784242744	-0.013380965	-2.261088127	-0.001813418	0.081170236	0.035293973	0.06626	-1.940554989	0.264348
Blk-2	0.225076	0.837985466	-0.017887454	-1.78584404	-0.013380965	-2.263782963	-0.00133442	0.081170236	0.039655199	0.067174	-1.945001513	0.259617
DTS-1	0.319657	0.917376068	3.296582583	6.15921225	0.374942338	30.80162648	0.09746154	0.117966617	0.300153409	0.065042	19.04213577	0.262246
BIR-1	7.189874	9.682560995	4.316217998	8.603361895	0.250310983	4.609368745	0.141726517	1.676194166	0.029791023	0.070887	22.26411522	0.770456
BBM-1	7.574326	5.051224022	2.942520684	5.310496863	13.80023044	1.339216247	0.094873279	2.901186742	0.014820352	0.273763	22.0323299	0.981242
PCC-1	0.540101	1.21303881	3.225809802	5.989564094	0.89884385	27.44619656	0.093693239	-0.044100387	0.344704942	0.064745	19.93910623	0.267264
GSM-1	8.309031	8.376309926	4.525954741	9.106118057	0.216037588	0.581712084	0.110920479	1.253680008	0.014064684	0.074819	18.63727654	0.907005
TS Dunite	0.406669	0.91232111	2.968348746	5.372408845	-0.104059881	30.28229335	0.080352625	0.087330172	0.469230573	0.070833	17.95405104	0.267395
1.1	0.766039	0.849143008	3.302918825	6.174400741	0.091881468	21.65263728	0.087322986	0.71870563	0.286090407	0.065648	17.10593983	0.273472
1.2	1.688521	1.309004122	3.346318103	6.278432367	-1.571364778	20.30565366	0.095592078	0.335129048	0.193599542	0.068329	18.02935827	0.298403
drift2	0.186115	0.805130095	-0.025794729	-1.804798427	-11.07009948	-2.269672441	-0.000272881	-8.244654109	0.037764697	0.044542	-1.997417338	0.258905
1.3	1.563919	1.733428592	2.636177802	4.576167871	-3.401731795	18.81058571	0.085249911	0.053434013	0.308105025	0.066864	16.65317471	0.302031
2.1	1.062495	0.849106175	2.730866545	4.803144547	-3.579836336	17.41351884	0.079669678	0.033268459	0.207986913	0.067587	13.51341157	0.28536
2.2	1.244878	0.841874397	2.782204287	4.926205322	-3.459930886	21.23361613	0.089185405	0.124696259	0.221361852	0.068241	16.89780263	0.294417
2.3	1.310159	0.854503123	2.699973292	4.72909089	-3.164696642	20.71051656	0.058244781	0.228024516	0.272064243	0.065583	16.37182642	0.283236
3.1	1.124922	0.839941171	2.601181226	4.49227821	-2.999084552	20.760285	0.052520423	0.32418831	0.256562421	0.065355	16.69933898	0.276705
3.2	0.955109	0.838306204	2.494490239	4.236531172	-3.146400148	20.61676958	0.058612974	0.295428961	0.195387429	0.070804	16.51973674	0.290222
3.3	1.034795	0.850458465	2.686425471	4.696615652	-2.972065963	20.20480784	0.066632338	0.310368663	0.268896323	0.065548	16.14555333	0.291466
BHVO-2	5.992577	7.785008943	4.268654331	8.489347888	-3.50310693	2.318541379	0.107633012	1.315460289	0.023295569	0.128786	20.47702358	1.560691
DTS2b	0.40781	0.917399742	2.810597432	4.994266018	-4.022525556	28.25204733	0.067163835	-0.34711144	0.308500261	0.066479	16.61284794	0.269366
MCL3.22	0.888283	0.84126247	2.284780564	3.733839896	-3.53821219	18.64168453	0.052067761	-0.051319751	0.178426268	0.069566	14.9358382	0.288561
drift3	0.186115	0.805130095	-0.025794729	-1.804798427	-11.07009948	-2.269672441	-0.000179768	-8.244654109	0.037764697	0.044542	-1.997417338	0.258905
339	6.457457	2.148984758	4.669578448	9.450395851	-4.203475576	13.33983352	0.178426787	-0.466368579	0.024794519	0.09856	11.88707935	1.083502
422	0.759177	0.912366633	2.680042083	4.681314148	-3.085843687	18.83146291	0.072766788	0.041833322	0.188372398	0.065135	16.11002607	0.270497
328	0.785335	1.694090022	8.802920341	19.35835509	-3.158502593	14.06401129	0.054683957	-0.045119793	0.503063145	0.069574	11.81998907	0.286338
335	0.645078	0.927940246	2.70231419	4.734702213	-2.565240071	21.44912326	0.052096482	0.069300206	0.260387463	0.066978	17.83386711	0.269761
413	1.733081	1.064496419	2.369153929	3.936089766	-2.560576579	21.38386435	0.063558996	-0.035498514	0.262410299	0.065045	17.79389394	0.273533
326	0.907485	0.933017685	1.742430618	2.433782632	-2.826582796	22.06532306	0.058481421	-0.067325008	0.09977123	0.066649	17.86746421	0.266146
325	0.969806	4.579721644	3.350712653	6.288966463	-2.815924389	19.09087724	0.068357734	-0.046642557	0.357454233	0.060647	18.07465077	0.30024
340	1.07706	1.287699348	2.751376515	4.852308626	-2.947038256	20.68006078	0.064720782	-0.09419846	0.244492474	0.065962	17.8981657	0.307755
334	2.910124	1.553796463	3.577786348	6.833280717	-3.085383177	19.6130931	0.082973983	-0.018490423	0.265252157	0.065506	17.29621901	0.346333
337	0.564888	0.927408499	2.729042855	4.798773014	-3.229948308	22.83145945	0.063025665	-0.063844585	0.320987527	0.069115	19.55739889	0.265086
drift4	0.186115	0.805130095	-0.025794729	-1.804798427	-11.07009948	-2.269672441	-0.000167254	-8.244654109	0.037764697	0.044542	-1.997417338	0.258905
CSW 11	2.154573	6.030940197	2.537064902	4.338586129	-1.597872783	12.53067699	0.083699701	0.829223096	0.102378364	0.075178	20.03107148	0.451596
CSW 28	5.460268	4.264114996	4.461328278	8.951203129	-3.924284848	13.00644067	0.120078803	0.223409201	0.027889474	0.070483	17.68364417	0.644767
418	1.231828	0.927676634	1.890852037	2.789560936	-3.909810164	21.24986847	0.075077508	-0.345810092	0.298481877	0.067996	17.40531053	0.274861
QV 135	0.526359	0.861449403	3.245838858	6.037575382	-3.934759114	22.64672502	0.05496575	-0.377032575	0.369969989	0.071974	17.53760841	0.26198
QV 128	6.359147	2.49002903	2.370749933	3.939915518	-0.729659505	0.048837589	0.091849325	-7.684248671	0.007781904	0.10675	23.56734565	0.623898
QV 121	3.221343	2.966199542	3.907635103	7.623955215	-5.337926865	10.48392581	0.178873392	-0.561464002	0.092969093	0.108284	11.36862157	1.274076
QV 124	4.511781	3.835918768	2.759288543	4.871274407	-3.410212369	8.110311809	0.100531013	1.900648013	0.051308011	0.100759	17.78099923	0.599344
QV 122	0.961584	12.90985293	1.795953328	2.562080953	-3.781988236	11.11713724	0.075626267	-0.268949264	0.156616497	0.063139	9.859906563	0.284234
QV 137	0.440351	0.925830664	3.110461662	5.713065151	-3.374167612	22.06902144	0.046367177	-0.08806484	0.250537061	0.066857	16.87612922	0.26527
QV 128	6.90393	2.696251171	2.727642877	4.795417151	2.311259131	0.346133115	0.101970861	-7.454011783	0.004207303	0.104779	24.62158165	0.628664
drift5	0.186115	0.805130095	-0.025794729	-1.804798427	-11.07009948	-2.269672441	-0.000152903	-8.244654109	0.037764697	0.044542	-1.997417338	0.258905
QV 128.1	6.045082	2.769145296	2.444413573	4.1164933	0.916560633	-0.010581827	0.093639968	-7.853068711	0.006005325	0.10287	22.28242999	0.594443
QV 137.1	0.468727	0.854097589	2.504265878	4.259964179	-3.855940207	18.20211098	0.038265053	-0.196389024	0.222233835	0.063757	13.85098557	0.2671
CSW 17	5.334983	2.552589319	5.923301699	12.45567322	-4.756464451	9.030220231	0.149099515	0.001754697	0.027899853	0.091856	11.79602743	1.348871
CSW 17.2	6.19458	2.791948233	7.06715772	15.19758984	-4.616647096	10.72470387	0.177051204	0.034418664	0.025150683	0.10127	13.78730224	1.536283
CSW 25	7.503973	9.028936903	4.126857117	8.149448346	-3.313297691	1.108467413	0.096796956	1.121318881	0.016937753	0.085707	14.43516371	0.630413
CSW 25.2	7.023961	8.712117002	3.935870322	7.691637347	-3.153670292	0.939647262	0.095900467	1.097063153	0.015818285	0.080455	13.78211406	0.603638
CSW 15	1.18669	0.910744555	2.746639292	4.840953116	-3.561921096	20.43268832	0.067282979	-0.283466229	0.235641346	0.066972	17.31280741	0.275337
CV1 121.2	3.673169	3.194695669	4.626659936	9.347516661	-4.496673016	14.99161515	0.20026172	-0.260668723	0.156779982	0.107412	15.58436124	1.336282
CSW 28.2	5.150687	3.902767503	4.162528169	8.234954782	-3.876845233	12.01390886	0.10355619	0.170558641	0.027974615	0.062049	16.01045536	0.583691
CSW 11	2.170765	6.868846636	2.782310236	4.926459291	-3.673849873	13.89779743	0.087175687	0.126905128	0.100298015	0.068562	23.25826574	0.423369
drift6	0.186115	0.805130095	-0.025794729	-1.804798427	-11.07009948	-2.269672441	-0.00013723	-8.244654109	0.037764697	0.044542	-1.997417338	0.258905
CSW 25.3	8.887161	10.48041469	4.906247782	10.01771164	-2.955818135	1.781889195	0.116268666	1.480941029	0.007588996	0.088125	17.95225093	0.685674
339.2	6.910726	2.112460108	4.89869094	9.999597269	-5.089479385	14.00718245	0.17820148	-0.480749339	0.0209835	0.096246	12.59930131	1.104891
U2.3	1.387879	0.845720979	2.822382928	5.022516817	-4.076821063	21.45217736	0.056698372	-0.398992496	0.277706956	0.061802	17.39396376	0.284467
U3.1	1.212472	0.848545933	2.743546663	4.83353983	-4.505535899	21.78302794	0.049244133	-0.399611234	0.268238967	0.065534	17.79819592	0.279707
U1.3	1.48178	1.52643902	2.578292218	4.437411382	-4.285073125	18.71368974	0.073614503	-0.416500624	0.292068421	0.067929	16.37689688	0.29065
drift7	0.186115	0.805130095	-0.025794729	-1.804798427	-11.07009948	-2.269672441	-0.000134772	-8.244654109	0.037764697	0.044542	-1.997417338	0.258905

Table 4: Major elements in Coast Range Ophiolite samples in wt% elements calculated in excel.

Sample no.	Site of XPS Analysis		Mineral type	SiO_2	FeO*	MnC	MgO	CaO	Na_2O	K_2O	NiO	TiO_2	Al_2O_3	Cr_2O_3	SO_2	Total
	x axis coordinaty	axis coordinate														
Coast Range Ophiolite																
Relic Minerals																
McL_329	-23416	-29034	**Olivine**	40.55	10.15	0.16	48.63	0.03	0	0.01	0.38	0	0	0.02	0.01	99.94
McL_329	-23322	-28974	**Olivine**	40.57	10.18	0.14	48.68	0.02	0	0	0.4	0	0	0	0.01	100.01
McL_329	-22801	-28861	**Olivine**	40.87	10.25	0.13	49	0.01	0	0	0.36	0.01	0	0	0	100.64
McL_329	-22791.1	-28854.1	**Olivine**	41.06	10.2	0.15	49.2	0.03	0	0	0.42	0	0	0	0.01	101.07
McL_329	-22781.2	-28847.2	**Olivine**	43.66	4.13	0.05	41.04	0.04	0.01	0	0.47	0	0.09	0	0.03	89.51
McL_329	-22771.3	-28840.3	**Olivine**	41.9	3.65	0.03	41.09	0.03	0	0.01	0.41	0	0.11	0.02	0.03	87.28
McL_329	-17831.3	-29919.8	**Olivine**	34.74	23.73	0.4	24.28	0.02	0.02	0	0.04	0.17	5.89	0.86	0.03	90.18
McL_239A	-9446	64	**Clinopyroxene**	47.41	13.47	0.25	12.56	15.61	0.7	0.12	0	2.33	0.01	0.02	0	99.94
McL_239A	-9446	64	**Clinopyroxene**	47.97	13.76	0.37	16.94	14.48	0.39	0.13	0.02	0.6	0.01	0	0	100.01
McL_239A	-9446	64	**Clinopyroxene**	50.62	13.68	0.45	12.62	19.05	0.41	0.05	0	0.7	0	0	0	100.64
McL_329	-17751.7	-29765.1	**Spinel**	0.05	11.72	0.1	19.36	0.04	0	0	0.36	0.05	56.11	12.23	0	100.03
McL_329	-17746	-29754	**Spinel**	0.02	11.88	0.14	19.2	0.01	0.02	0	0.37	0.05	55.89	12.77	0	100.36
McL_329	-17537	-29808	**Spinel**	0.03	11.97	0.14	19.38	0.01	0.02	0	0.35	0.06	57.04	11.52	0.01	100.53
McL_329	-17535	-29940	**Spinel**	0.05	11.94	0.16	19.33	0	0	0	0.34	0.05	57.71	11.38	0	100.96
McL_329	-11884.1	-24312	**Spinel**	0.04	13.06	0.14	18.68	0	0	0.01	0.35	0.04	56.11	11.6	0	100.02
McL_329	-11863.7	-24304	**Spinel**	0.06	13.23	0.14	18.7	0	0	0.01	0.33	0.04	55.96	11.33	0	99.81
McL_329	-11843.2	-24296	**Spinel**	0.03	13.19	0.14	18.84	0	0.01	0	0.35	0.05	56.71	11.4	0	100.7
McL_329	-11822.8	-24288	**Spinel**	0.04	13.53	0.16	18.82	0	0	0	0.33	0.05	56.61	11.29	0	100.84
McL_329	-11802.3	-24280	**Spinel**	0.11	12.91	0.15	20.59	0.02	0.01	0.01	0.33	0.04	53.13	11.21	0.01	98.53
McL_356	12292	21989	**Andradite Garnet**	34.06	24.23	0.06	0.09	33.21	0	0	0.01	0.95	1.98	0.43	0.01	95.04
McL_Surface	-21867	14617	**Andradite Garnet**	34.19	22.17	0.04	0.18	33.11	0.02	0	0	2.24	1.23	2.16	0	95.35
McL_Surface	-12889	31548	**Andradite Garnet**	27.6	13.48	0.12	0.93	31.74	0	0	0.01	11.53	1.18	1.56	0	88.14
McL_239A	19968	-9446	**Orthopyroxene**	47.41	13.47	0.25	12.56	15.61	0.7	0.12	0	2.33	3.33	0.01	0	95.8
McL_239A	20005.3	-9446	**Orthopyroxene**	47.97	13.76	0.37	16.94	14.48	0.39	0.13	0.02	0.6	5.26	0.01	0	99.93
McL_239A	20042.5	-9446	**Orthopyroxene**	50.62	13.68	0.45	12.62	19.05	0.41	0.05	0	0.7	2.36	0	0	99.93

Table 5: Major mineral chemistry from relict peridotite mineral grains from the Coast Range ophiolite, California spanning a surface sample (McL-surface), and three M81-313 cores (McL-239A, McL-329, and McL-356)

Sample no.	Site of XPS Analysis		Mineral	SiO_2	FeO*	MnO	MgO	CaO	Na_2O	K_2O	NiO	TiO_2	Al_2O_3	Cr_2O_3	SO_2	Total
	x axis	y axis														
Coast Range Ophiolite																
Serpentinized Minerals																
McL_356	12580	21944	**Serpentine**	42.75	3.52	0.06	35.07	0.05	0.03	0	0.06	0	1.41	0.05	0.01	83.01
McL_356	12292	22136	**Serpentine**	41.51	5.87	0.12	36.42	0.17	0	0.01	0.12	0.04	2.95	0.58	0	87.79
McL_356	12272	22171	**Serpentine**	40.85	5.73	0.12	36.62	0.16	0	0.01	0.11	0.03	2.87	0.6	0.02	87.13
McL_329	-23332.5	-28980.7	**Serpentine**	38.84	8.92	0.29	30.17	0.07	0.01	0	0.53	0	0.04	0.02	0.04	78.93
McL_329	-17536.6	-29837.3	**Serpentine**	33.86	8.7	0.14	30.83	0.02	0.01	0.01	0.1	0.01	8.82	4.63	0.02	87.15
McL_329	-23405.6	-29027.3	**Serpentine**	42.95	11.03	0.39	29.94	0.06	0.04	0.02	0.52	0	0	0	0.02	84.97
McL_329	-19184	-29599	**Serpentine**	42.66	5.91	0.06	35.12	0.05	0	0.02	0.35	0	0.46	0.02	0.02	84.66
McL_329	-19100	-29626	**Serpentine**	41.54	8.31	0.1	33.04	0.04	0	0	0.41	0.01	0.4	0	0.02	83.87
McL_329	-17842.6	-29941.9	**Serpentine**	37.6	7.72	0.17	34.18	0.04	0	0	0.09	0.47	5.64	1.04	0.04	87
McL_329	-17808.5	-29875.6	**Serpentine**	36.09	11.93	0.14	30.33	0.03	0	0.01	0.02	0.01	7.89	0.05	0.02	86.51
McL_329	-17819.9	-29897.7	**Serpentine**	37.93	7.66	0.18	34.73	0.04	0.01	0	0.05	0.47	5.5	0.99	0.06	87.62
McL_329	-11741	-24256	**Serpentine**	35.95	10.13	0.26	32.28	0.02	0.01	0.02	0.07	0.09	8.56	0.66	0.01	88.05
McL_329	-23374.2	-29007.3	**Serpentine**	42.12	2.35	0	40.11	0.02	0	0	0.36	0	0	0	0.02	84.99
McL_329	-17535.9	-29881.3	**Serpentine**	38.59	7.28	0.06	35.32	0.05	0.01	0.01	0.02	0	4.7	0.08	0.6	86.72
McL_329	-23353.3	-28994	**Serpentine**	41.92	4.77	0.11	38.1	0.03	0.01	0	0.27	0	0.15	0.01	0.09	85.47
McL_329	-17848.3	-29953	**Serpentine**	37.44	8.61	0.19	34.28	0.06	0.01	0	0.1	0.49	5.86	1.07	0.06	88.18
McL_329	-17791.5	-29842.4	**Serpentine**	40.8	7.78	0.16	35.22	0.04	0	0.01	0.05	0.05	1.61	0.01	0.05	85.76
McL_329	-17814.2	-29886.6	**Serpentine**	37.87	8.06	0.11	35.03	0.04	0	0	0.05	0.5	4.27	1.01	0.02	86.96
McL_329	-17837	-29930.8	**Serpentine**	37.81	7.67	0.12	35.56	0.04	0	0	0.06	0.48	5.77	1.11	0.01	88.63
McL_329	-17763.1	-29787.2	**Serpentine**	37.47	10.09	0.23	33.15	0.18	0	0.01	0.06	0.23	6.98	0.92	0.03	89.34
McL_329	-17854	-29964	**Serpentine**	37.03	9.76	0.23	33.54	0.05	0.02	0	0.08	0.61	5.77	1.07	0.06	88.21
McL_329	-17825.6	-29908.7	**Serpentine**	40.25	6.44	0.13	36.99	0.09	0	0	0.01	0.14	3.41	0.06	0.04	87.57
McL_329	-23363.8	-29000.7	**Serpentine**	40.92	5.92	0.12	37.63	0.05	0	0	0.46	0	0.08	0.01	0.05	85.24
McL_329	-11925	-24328	**Serpentine**	38.56	5.54	0.1	38.05	0.03	0.01	0	0.39	0.01	2.73	0.05	0.25	85.72
McL_329	-19186	-29563	**Serpentine**	42.05	8.71	0.18	34.88	0.04	0	0	0.39	0	0.24	0.01	0.01	86.51
McL_329	-17785.8	-29831.4	**Serpentine**	41.14	9.11	0.13	34.56	0.04	0	0.01	0.04	0.07	2.03	0.01	0.07	87.2
McL_329	-17535.5	-29910.7	**Serpentine**	40.64	9.09	0.14	34.65	0.05	0.01	0	0.04	0.06	1.96	0.09	0.03	86.76
McL_329	-17535.7	-29896	**Serpentine**	40.75	8.98	0.15	34.77	0.05	0	0	0.01	0.05	1.8	0.09	0.04	86.71
McL_329	-17768.7	-29798.2	**Serpentine**	39.21	9.91	0.1	34.28	0.04	0	0.01	0.02	0.01	4.23	0.06	0.01	87.88
McL_329	-17535.2	-29925.3	**Serpentine**	40.85	9.1	0.21	35.16	0.04	0	0	0.11	0.05	1.81	0.2	0.02	87.55
McL_329	-19124	-29625	**Serpentine**	39.82	11.76	0.15	32.9	0.07	0	0	0.5	0.01	0.85	0	0.02	86.1
McL_329	-17536.3	-29852	**Serpentine**	40.67	8.31	0.1	36.54	0.05	0.02	0.01	0.02	0.02	3.19	0.1	0	89.02
McL_329	-19363	-29583	**Serpentine**	40.28	5.54	0.08	39.34	0.03	0	0	0.24	0.01	0.23	0.01	0.12	85.89
McL_329	-19363	-29583	**Serpentine**	40.28	5.54	0.08	39.34	0.03	0	0	0.24	0.01	0.23	0.01	0.12	85.89
McL_329	-19161	-29590	**Serpentine**	41.31	4.61	0.07	40.43	0.04	0.01	0.01	0.36	0.01	0.2	0	0.03	87.08
McL_329	-17536.1	-29866.7	**Serpentine**	39.29	12.47	0.15	32.66	0.03	0	0.01	0	0.01	3.99	0.07	0.06	88.75
McL_329	-17774.4	-29809.3	**Serpentine**	40.4	11.54	0.16	33.69	0.02	0	0	0	0.04	2.55	0.06	0.03	88.49
McL_329	-17780.1	-29820.3	**Serpentine**	39.39	12.67	0.16	32.67	0.02	0.02	0.01	0	0.01	4.42	0.01	0.01	89.4
McL_329	-19351	-29573	**Serpentine**	41.57	4.96	0.05	40.49	0.02	0	0	0.32	0.01	0.12	0	0.03	87.57
McL_329	-19351	-29573	**Serpentine**	41.57	4.96	0.05	40.49	0.02	0	0	0.32	0.01	0.12	0	0.03	87.57
McL_surface	-12889	31524	**Serpentine**	39.32	3.28	0.07	36.31	0.04	0	0	0.07	0.03	1.78	0.97	0.01	81.87
McL_surface	-12889	31524	**Serpentine**	39.32	3.28	0.07	36.31	0.04	0	0	0.07	0.03	1.78	0.97	0.01	81.87
McL_surface	-12991	31605	**Serpentine**	40.23	4.15	0.11	36.22	0.06	0.05	0.01	0.11	0.01	0.71	0.05	0.02	81.72
McL_surface	-12991	31605	**Serpentine**	40.23	4.15	0.11	36.22	0.06	0.05	0.01	0.11	0.01	0.71	0.05	0.02	81.72
McL_surface	-13345	18793	**Serpentine**	42.77	3.95	0.07	36.56	0.06	0	0.02	0.18	0	1.19	0.15	0.02	84.97
McL_surface	-22590	14962	**Serpentine**	40.51	5.28	0.09	35.91	0.12	0.01	0.01	0.07	0.03	3.47	0.92	0.01	86.42
McL_surface	-22590	14962	**Serpentine**	40.51	5.28	0.09	35.91	0.12	0.01	0.01	0.07	0.03	3.47	0.92	0.01	86.42
McL_surface	-22739	14833	**Serpentine**	42.6	3.87	0.09	37.5	0.06	0	0.01	0.02	0.01	1.22	0.13	0.01	85.52
McL_surface	-21803	14620	**Serpentine**	42.57	3.43	0.06	38.39	0.05	0	0.02	0.12	0	1.73	0.94	0.01	87.33
McL_surface	-22738	14852	**Serpentine**	42.93	3.97	0.08	37.9	0.06	0.02	0.01	0.05	0.01	1.21	0.13	0	86.36
McL_surface	-22564	15048	**Serpentine**	40.57	5.29	0.1	36.66	0.13	0	0.02	0.03	0.03	3.47	0.83	0.01	87.12
McL_surface	-22564	15048	**Serpentine**	40.57	5.29	0.1	36.66	0.13	0	0.02	0.03	0.03	3.47	0.83	0.01	87.12
McL_surface	-12910	31504	**Serpentine**	41.63	4.16	0.11	38.25	0.05	0	0	0.06	0	0.62	0.07	0	84.96
McL_surface	-12910	31504	**Serpentine**	41.63	4.16	0.11	38.25	0.05	0	0	0.06	0	0.62	0.07	0	84.96
McL_surface	-13282	19002	**Serpentine**	44.09	4	0.13	38.57	0.03	0.01	0.01	0.06	0.01	0.42	0.05	0	87.38

Table 6: Major mineral chemistry from serpentine mineral grains from the Coast Range ophiolite, California spanning a surface sample (McL-surface), and three M81-313 cores (McL-239A, McL-329, and McL-356)

Mean Coast Range Ophiolite Olivine Chemistry McL-329

Oxide (wt%)	***McL-329***	***San Carlos Olivine***
Al_2O_3	0.000	0.020
CaO	0.005	0.100
Cr_2O_3	0.005	0.017
FeO	10.200	9.900
K_2O	0.005	0.000
MgO	48.900	49.000
MnO	0.150	0.137
Na_2O	0.010	0.017
NiO	0.390	0.387
SiO_2	40.800	40.700
SO_2	0.000	0.000
TiO_2	0.000	0.000
Total	**100.000**	**100.000**
Cations (per formula unit)	***McL-329***	***San Carlos Olivine***
Al	0.000	0.003
Ca	0.001	0.016
Cr	0.001	0.002
Fe	1.254	1.218
K	0.001	0.000
Mg	10.710	10.742
Mn	0.019	0.017
Na	0.003	0.005
Ni	0.046	0.046
Si	5.996	5.987
S	0.000	0.000
Ti	0.000	0.000
Total	**18.029**	**18.036**

Table 7: Representative olivine mineral chemistry as major cations (per formula unit) for McL-329.

Slide	*x*	*y*	***Fo***	***Fa***
McL_329	-23416	-29034	89.37049	10.62951
McL_329	-23322	-28974	89.37128	10.62872
McL_329	-22801	-28861	89.378576	10.621424
McL_329	-22791.1	-28854.1	89.444303	10.555697
McL_329	-22781.2	-28847.2	94.595161	5.404839
McL_329	-22771.3	-28840.3	95.216481	4.7835189
McL_329	-17831.3	-29919.8	64.203638	35.796362

Table 8: Forsterite and fayalite values of olivine mineral chemistry obtained via microprobe and calculated in excel.

Sample ID													
	Major Elements in w.t. %												
	Al2O3	CaO	Cr2O3	FeO	K2O	MgO	MnO	Na2O	NiO	P2O5	SiO2	TiO2	Total
DTS-1	0.603925	1.284301	2.255616	7.923855	0.451683	51.08064	0.125838	0.159006	0.235877	0.149008	40.73184	0.437442	105.439
BIR-1	13.58374	13.55531	2.95328	11.06826	0.301543	7.644061	0.182991	2.259326	0.023411	0.162399	47.62378	1.285165	100.6433
BBM-1	14.31008	7.071572	2.013357	6.831978	16.62478	2.220922	0.122496	3.910482	0.011647	0.627178	47.12798	1.636768	102.5092
PCC-1	1.020405	1.69822	2.207191	7.705602	1.082814	45.51608	0.120973	0.059442	0.270888	0.148327	42.65049	0.445812	102.9262
GSM-1	15.69815	11.7266	3.096787	11.71506	0.260255	0.964697	0.143216	1.689823	0.011053	0.171407	39.86583	1.512936	86.85582
TS Dunite	0.768314	1.277224	2.031029	6.911629	0.125358	50.21939	0.103748	0.117712	0.368747	0.162276	38.40439	0.446029	100.9358
1.1	1.447268	1.188776	2.259951	7.943395	0.110687	35.90819	0.112748	0.968737	0.224825	0.150396	36.59025	0.456167	87.36138
1.2	3.190102	1.832569	2.289646	8.077232	1.892983	33.67438	0.123424	0.451717	0.152141	0.156537	38.56547	0.497753	90.90396
1.3	2.954693	2.426751	1.803748	5.887261	4.097978	31.195	0.110071	0.072023	0.242126	0.153182	35.62176	0.503804	85.0684
2.1	2.007359	1.188725	1.868537	6.179267	4.312536	28.87814	0.102866	0.044842	0.163447	0.154839	28.90569	0.475997	74.28225
2.2	2.351933	1.178601	1.903664	6.337586	4.168089	35.21329	0.115152	0.168077	0.173958	0.156336	36.14503	0.491104	88.40283
2.3	2.475268	1.19628	1.847399	6.083997	3.812428	34.3458	0.075203	0.307352	0.213803	0.150247	35.01995	0.472453	86.00018
3.1	2.125301	1.175894	1.779802	5.779336	3.61292	34.42833	0.067812	0.43697	0.201621	0.149725	35.72051	0.46156	85.93979
3.2	1.804475	1.173605	1.706801	5.450317	3.790387	34.19033	0.075678	0.398206	0.153546	0.162208	35.33634	0.484107	84.726
3.3	1.955026	1.190618	1.838129	6.042217	3.580371	33.50714	0.086033	0.418343	0.211313	0.150168	34.53594	0.486182	84.00149
BHVO-2	11.3217	10.89879	2.920735	10.92158	4.220102	3.845011	0.138971	1.773096	0.018307	0.295042	43.80112	2.603321	92.75779
DTS2b	0.77047	1.284334	1.923091	6.425146	4.845832	46.85248	0.086719	0.467868	0.242436	0.1523	35.5355	0.449318	99.0355
MCL3.22	1.678221	1.177744	1.563312	4.803602	4.262393	30.9149	0.067228	0.069173	0.140217	0.159371	31.94832	0.481335	77.26581
339	12.19999	3.008518	3.195059	12.15798	5.063818	22.12244	0.230377	0.628614	0.019485	0.225796	25.42691	1.807342	86.08633
422	1.434303	1.277288	1.833761	6.022532	3.717436	31.22962	0.093953	0.056387	0.148033	0.149222	34.45995	0.451204	80.87369
328	1.483723	2.371679	6.023209	24.90461	3.804966	23.3234	0.070605	0.060817	0.395334	0.159391	25.2834	0.477629	88.35877
335	1.218737	1.29909	1.849	6.091216	3.090278	35.57069	0.067265	0.093409	0.204627	0.153443	38.14731	0.449977	88.23504
413	3.274289	1.490265	1.621043	5.063797	3.08466	35.46246	0.082065	0.047848	0.206216	0.149016	38.06181	0.456268	88.99973
326	1.714501	1.306199	1.192221	3.131072	3.405111	36.59258	0.075509	0.090747	0.078406	0.15269	38.21917	0.443946	86.40215
325	1.832243	6.411482	2.292653	8.090784	3.392271	31.65983	0.08826	0.062869	0.280907	0.13894	38.66235	0.500817	93.41341
340	2.034876	1.802743	1.88257	6.242517	3.550221	34.29529	0.083565	0.126969	0.192136	0.151116	38.28485	0.513354	89.1602
334	5.498062	2.175272	2.448024	8.791047	3.716881	32.52586	0.107132	0.024923	0.20845	0.15007	36.99726	0.577703	93.22068
337	1.067235	1.298346	1.867289	6.173643	3.891035	37.86312	0.081376	0.086056	0.25225	0.15834	41.83401	0.442178	95.01487
CSW 11	4.070608	8.443147	1.735932	5.581611	1.924916	20.78056	0.108069	1.117702	0.080455	0.172228	42.84721	0.753288	87.61573
CSW 28	10.31602	5.969642	3.052568	11.51576	4.727484	21.56955	0.15504	0.301131	0.021917	0.161473	37.82598	1.075507	96.69207
418	2.327278	1.298721	1.293775	3.588783	4.710047	35.24025	0.096937	0.466114	0.234563	0.155775	37.23061	0.458484	87.10133
QV 135	0.994444	1.206005	2.220896	7.767368	4.740103	37.55676	0.070969	0.508199	0.290743	0.164888	37.5136	0.436998	93.47097
QV 128	12.01426	3.485971	1.622135	5.068719	0.879002	0.080991	0.118592	10.35753	0.006115	0.244559	50.41143	1.040697	85.33
QV 121	6.086045	4.152596	2.673715	9.808253	6.430462	17.38628	0.230953	0.756792	0.07306	0.248073	24.31791	2.125231	74.28937
QV 124	8.524053	5.370179	1.887984	6.266917	4.108195	13.44994	0.129801	2.561865	0.040321	0.230834	38.03422	0.99974	81.60405
QV 122	1.816709	18.07343	1.228843	3.296129	4.556063	18.43638	0.097645	0.362514	0.123078	0.144648	21.09071	0.474118	69.70027
QV 137	0.831949	1.296137	2.128267	7.349884	4.064772	36.59871	0.059867	0.118702	0.196886	0.153166	36.09867	0.442485	89.3395
QV 128	13.04351	3.774676	1.866331	6.169326	2.784314	0.574018	0.13166	10.04719	0.003306	0.240043	52.66648	1.048647	92.34951
QV 128.1	11.4209	3.876726	1.672538	5.295887	1.104157	0.017549	0.120904	10.58508	0.004719	0.235669	47.66295	0.991564	82.98864
QV 137.1	0.88556	1.195713	1.71349	5.480463	4.645151	30.18592	0.049406	0.264711	0.174643	0.146065	29.62778	0.445537	74.81444
CSW 17	10.07932	3.573554	4.052892	16.02428	5.72999	14.97549	0.192511	0.002365	0.021925	0.210438	25.23214	2.249994	82.3449
CSW 17.2	11.70334	3.908649	4.835551	19.55177	5.561555	17.78558	0.228601	0.046393	0.019765	0.232004	29.49156	2.562607	95.92737
CSW 25	14.17716	12.64026	2.823713	10.4843	3.991444	1.838254	0.12498	1.511415	0.013311	0.196349	30.87736	1.051564	79.73011
CSW 25.2	13.27028	12.19672	2.693035	9.895327	3.799145	1.558287	0.123822	1.478721	0.012431	0.184319	29.48046	1.006902	75.69945
CSW 15	2.241998	1.275017	1.879329	6.227908	4.290954	33.88506	0.086873	0.382081	0.18518	0.15343	37.03274	0.459278	88.09985
CV1 121.2	6.939673	4.472484	3.165693	12.02562	5.417026	24.86172	0.258569	0.351353	0.123206	0.246075	33.33553	2.228994	93.42594
CSW 28.2	9.73113	5.463765	2.848121	10.59431	4.670335	19.92356	0.133707	0.229894	0.021984	0.142152	34.24696	0.97363	88.97955
CSW 11	4.1012	9.616193	1.903736	6.337912	4.431213	23.04776	0.112557	0.171054	0.07882	0.157073	49.7503	0.706203	100.414
CSW 25.3	16.7904	14.67229	3.356995	12.88783	3.560798	2.95504	0.150121	1.996146	0.005964	0.20189	38.40054	1.143744	96.12176
339.2	13.05635	2.957385	3.351824	12.86453	6.131164	23.22916	0.230086	0.647997	0.01649	0.220495	26.95038	1.843021	91.49888
Average	5.432614	3.930707	2.311266	8.174674	3.871803	24.97232	0.117333	1.163786	0.133612	0.17554	35.56885	0.844026	86.69654
Median	2.714981	2.273475	1.885277	6.254717	3.94124	30.55041	0.107601	0.329352	0.150087	0.156805	36.12185	0.499285	87.48855
Mode	16.7904	18.07343	6.023209	24.90461	6.430462	37.86312	0.258569	10.58508	0.395334	0.248073	52.66648	2.562607	100.414
Range	0.831949	1.173605	1.192221	3.131072	0.110687	0.017549	0.049406	0.002365	0.003306	0.13894	21.09071	0.436998	69.70027

Table 9: Major elements in Coast Range Ophiolite samples in oxide wt% elements calculated in excel.

Appendices: Figures

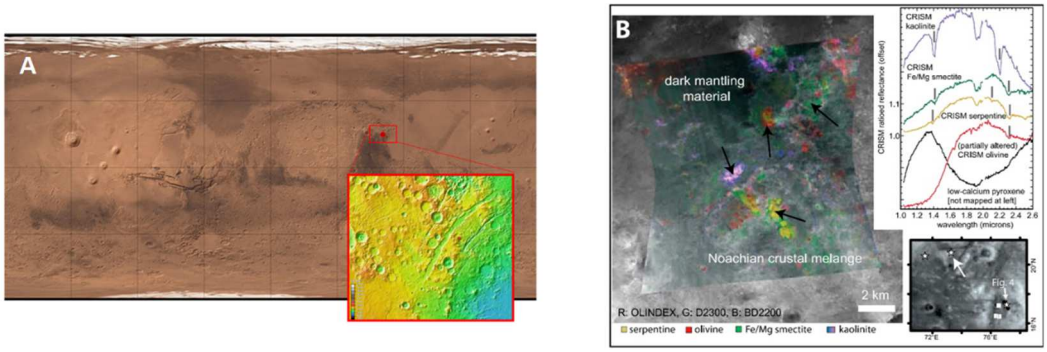

Figure 1. (A) Map projection (R. Hart, using Google Mars/NASA tools) shows Nili Fossae with respect to the planetary surface; elevation relief zoom box shows features of the Nili Fossae mélange terrain. (B) Modified from Ehlmann et al., (2010), CRISM image FRT0000ABCB of the Nili Fossae region displays the distribution of minerals in Mars mélange terrain with serpentine, olivine, Fe/Mg smectite, and kaolinite in Noachian ultramafic rock units.

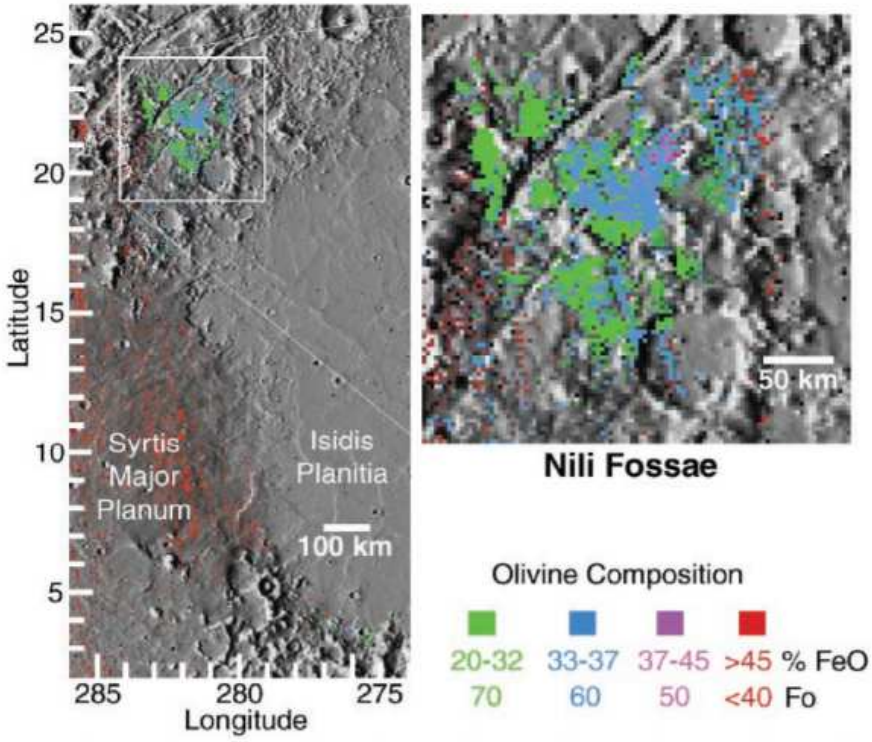

Figure 2. Modified from Hoefen et al., (2010), Mars Global Surveyor (MGS) using the Thermal Emission Spectrometer, of the Nili Fossae region displays the distribution of olivine in Noachian ultramafic rock units.

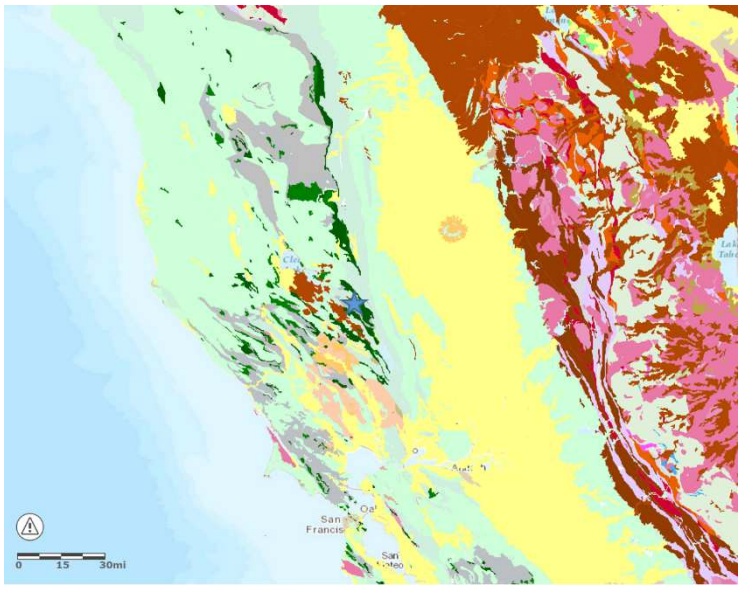

Figure 3. Geological map of California in ArcGIS10.5, with ultramafic rocks shaded dark green. Other mélange units occur between the Coast Range Ophiolite units and the Pacific Coast. Sacramento Valley and Sierra Nevada units are colored yellow and red. Blue star indicates the serpentinite locality in the UC-Davis held McLaughlin Natural Reserve (http://nrs.ucdavis.edu/mcl/). Samples obtained from this site included drill cores, outcrop samples, shallow manually obtained mini-cores. We present preliminary data on three different cored specimens.

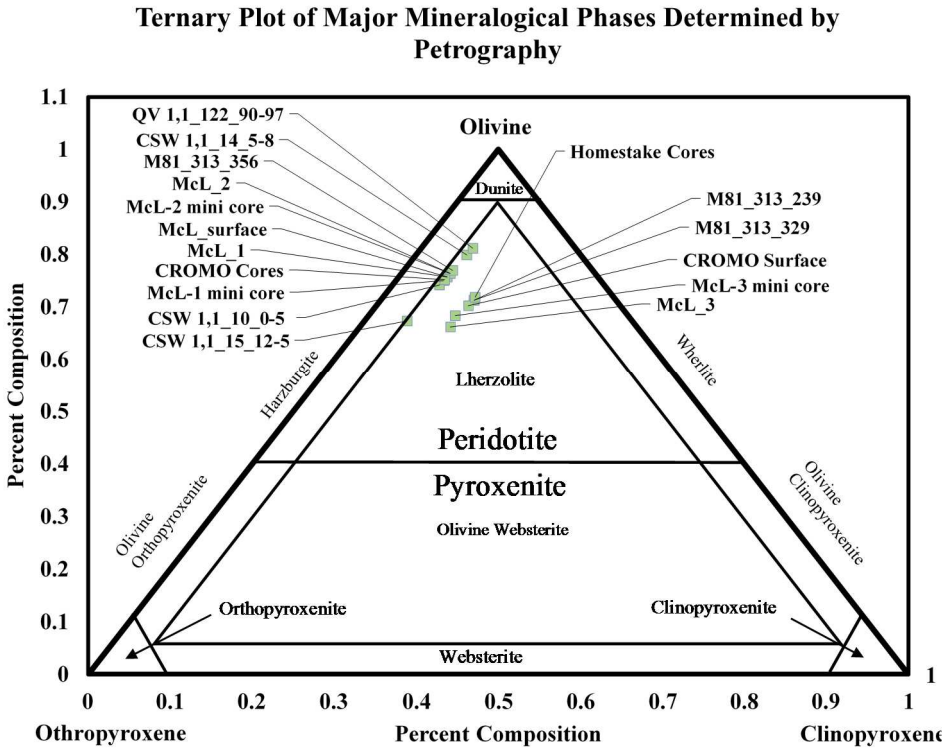

Figure 4. Mean mineralogies calculated for major rock type determination, using the peridotite-pyroxenite ternary phase diagram. The representative samples plot in the lherzolite stability field predominantly, with one sample (CSW1,1_15_12-5) determined as a harzburgite-lherzolite. McL-2 mini core and McL-1 mini also was on the harzburgite-lherzolite, however both were greater than 75% within the stability field of lherzolite.

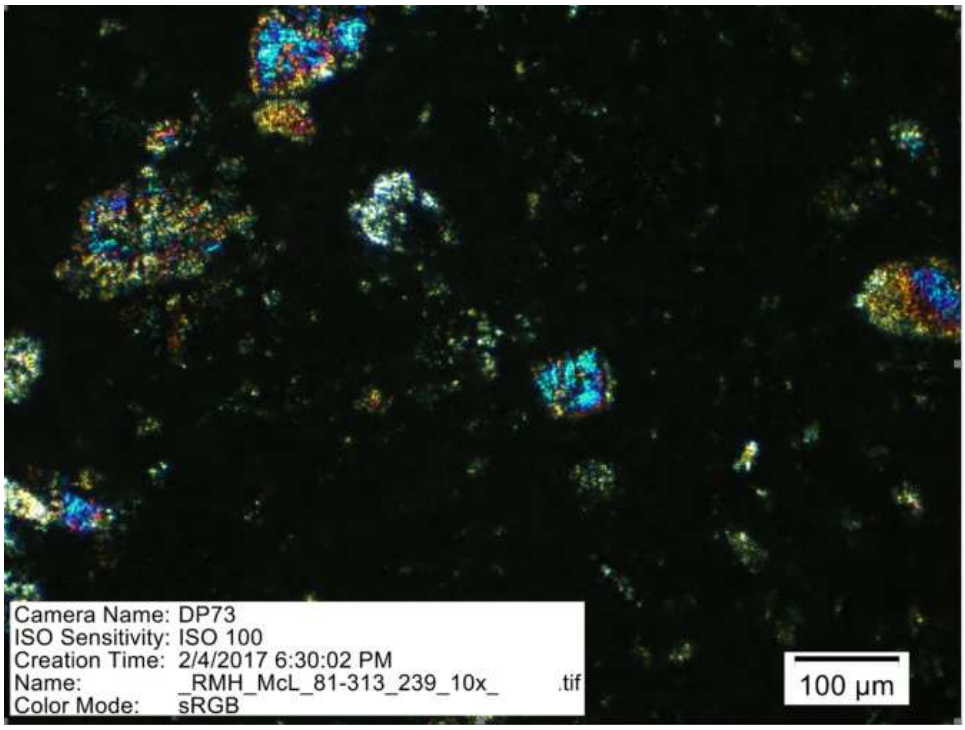

Figure 5. Representative photomicrograph of McL_239 at 10x under cross polarized light, consisting of largely serpentinized peridotite with second order interference colors from relict olivine grains the Coast Range Ophiolite obtained at the McLaughlin Natural Research Reserve.

Figure 6. Representative photomicrograph of McL_239A at 2x, under cross polarized light, consisting of largely serpentinized peridotite with low second order interference colors from relict olivine grains the Coast Range Ophiolite obtained at the McLaughlin Natural Research Reserve.

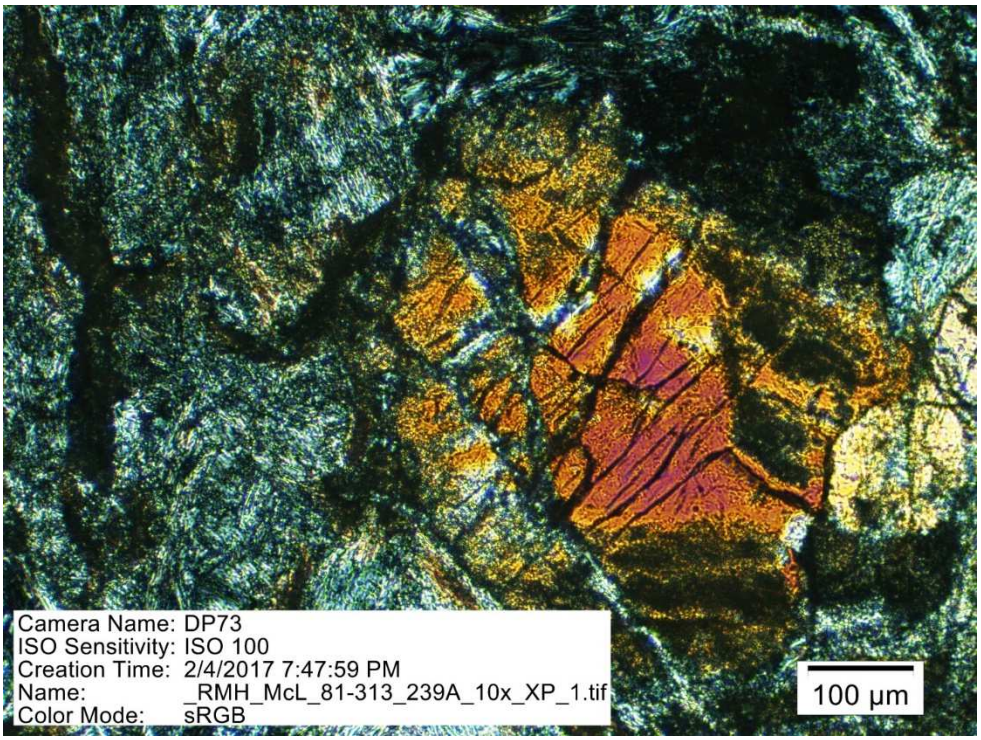

Figure 7. Representative photomicrograph of McL_239A under cross polarized light, consisting of largely serpentinized peridotite with low second order interference colors from relict olivine grains the Coast Range Ophiolite obtained at the McLaughlin Natural Research Reserve.

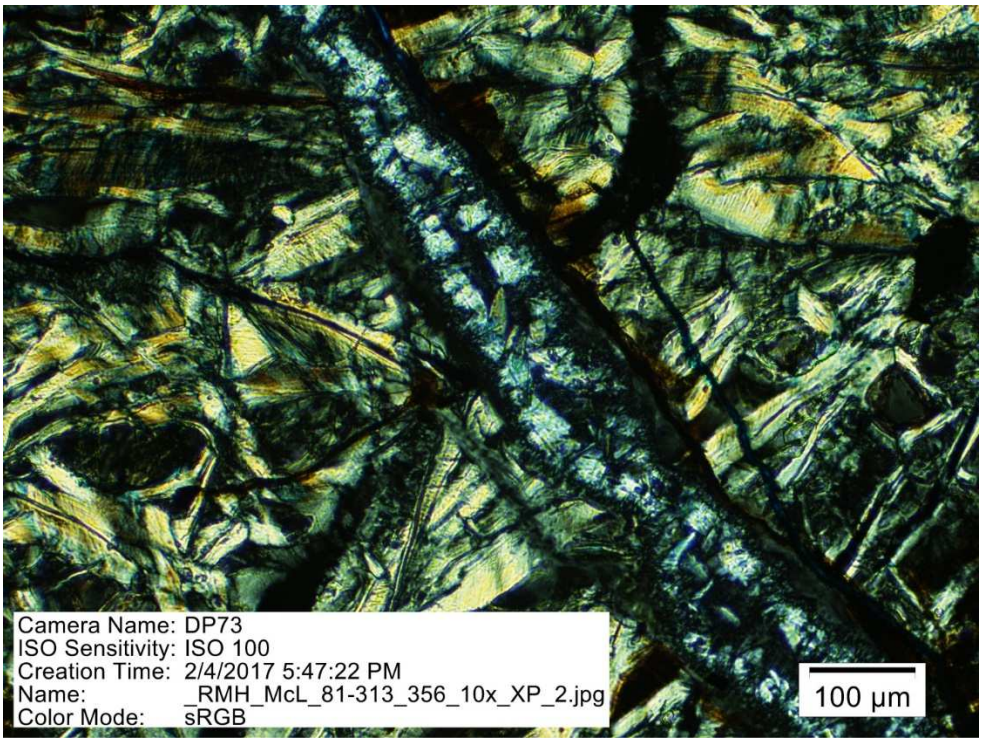

Figure 8. Representative photomicrograph of McL_356, at 10x under cross polarized light, consisting of largely serpentinized peridotite with a large vein of chrysotile at center from the Coast Range Ophiolite obtained at the McLaughlin Natural Research Reserve. Some second order interference colors occur in approximately 15% of the sample.

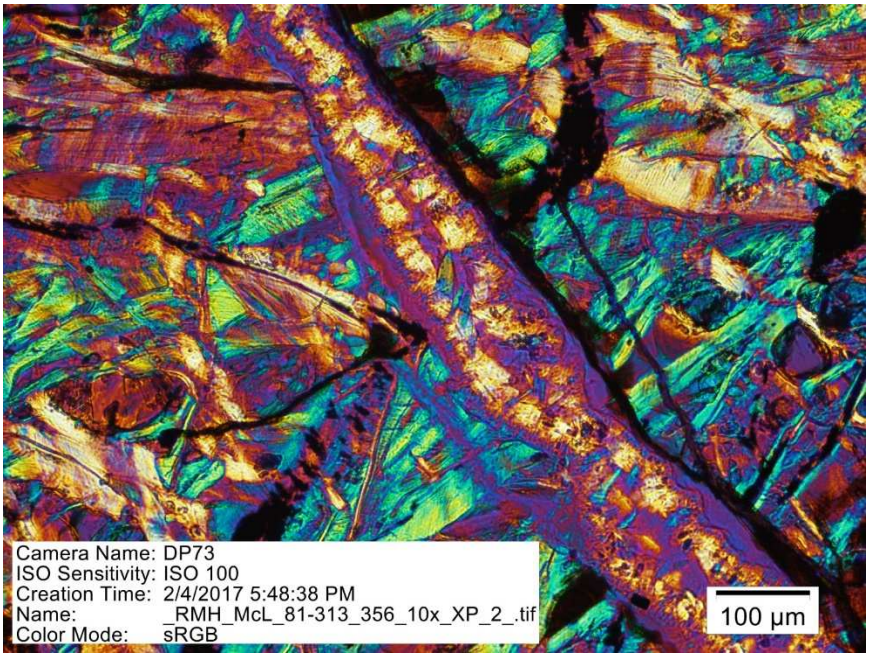

Figure 9. Representative photomicrograph of McL_356, at 10x under cross polarized light with the retardation plate inserted, consisting of largely serpentinized peridotite with a large vein of chrysotile at center. Sample from the Coast Range Ophiolite obtained at the McLaughlin Natural Research Reserve.

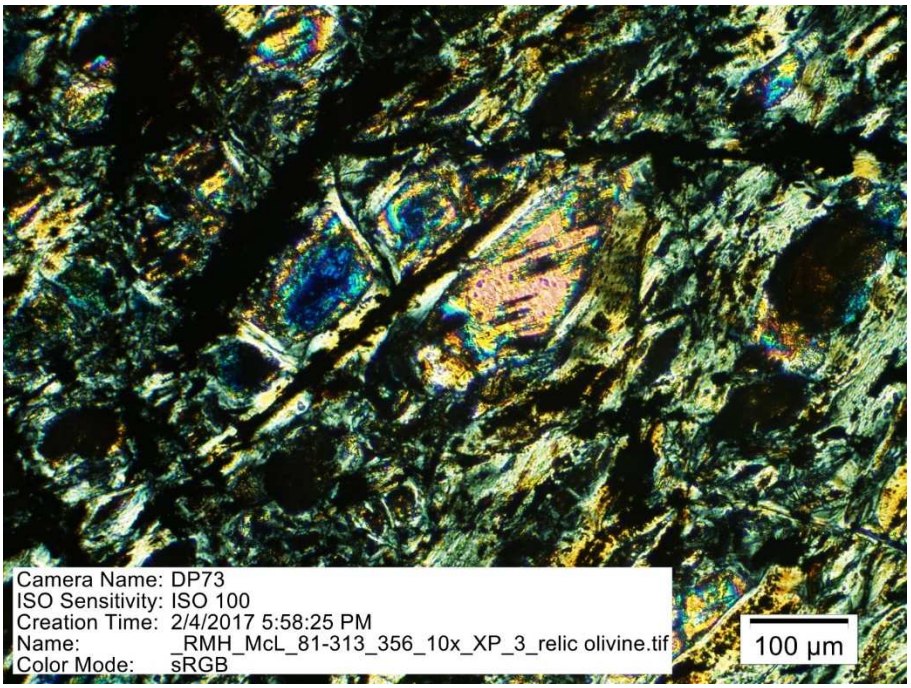

Figure 10. Representative photomicrograph of McL_356 at 10x under cross polarized light, consisting of largely serpentinized peridotite with second order interference colors from relict olivine grains the Coast Range Ophiolite obtained at the McLaughlin Natural Research Reserve.

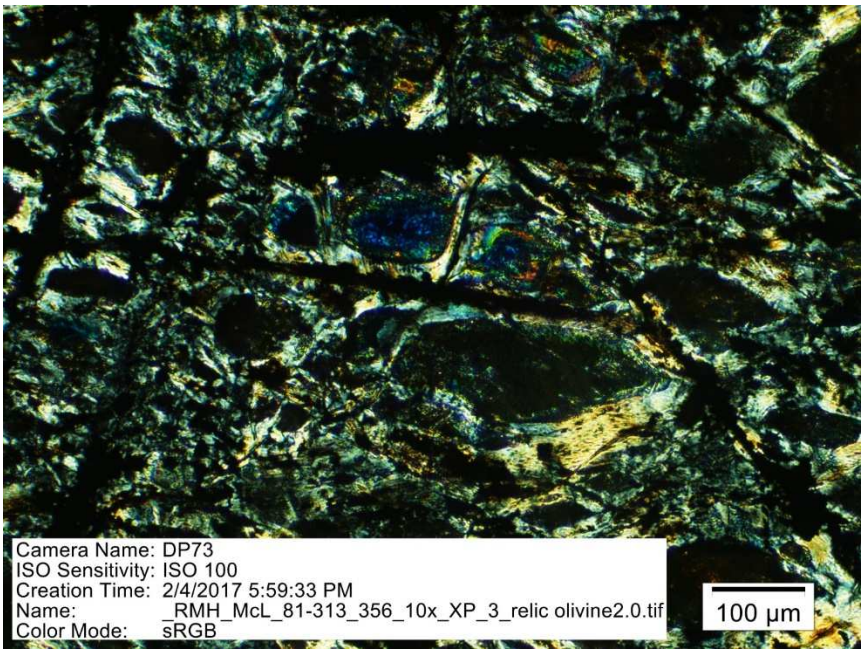

Figure 11. Representative photomicrograph of McL_356 at 10x under cross polarized light at some location as Figure 15 rotated 90 degrees, consisting of largely serpentinized peridotite with second order interference colors from relict olivine grains the Coast Range Ophiolite obtained at the McLaughlin Natural Research Reserve.

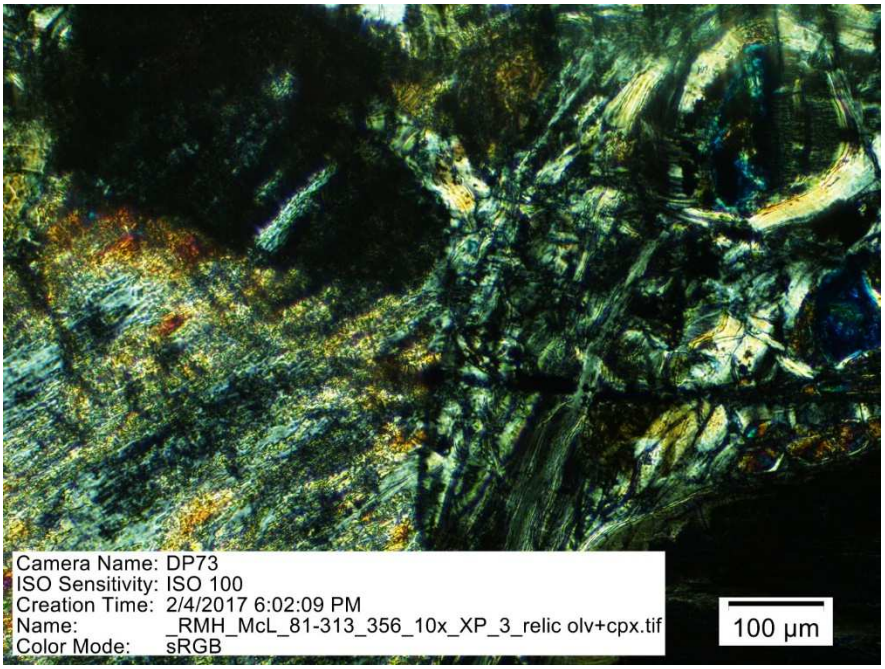

Figure 12. Representative photomicrograph of McL_356, at 10x under cross polarized light consisting of largely serpentinized peridotite with evidence of higher order interference colors in approximately 5% of the sample from the Coast Range Ophiolite obtained at the McLaughlin Natural Research Reserve.

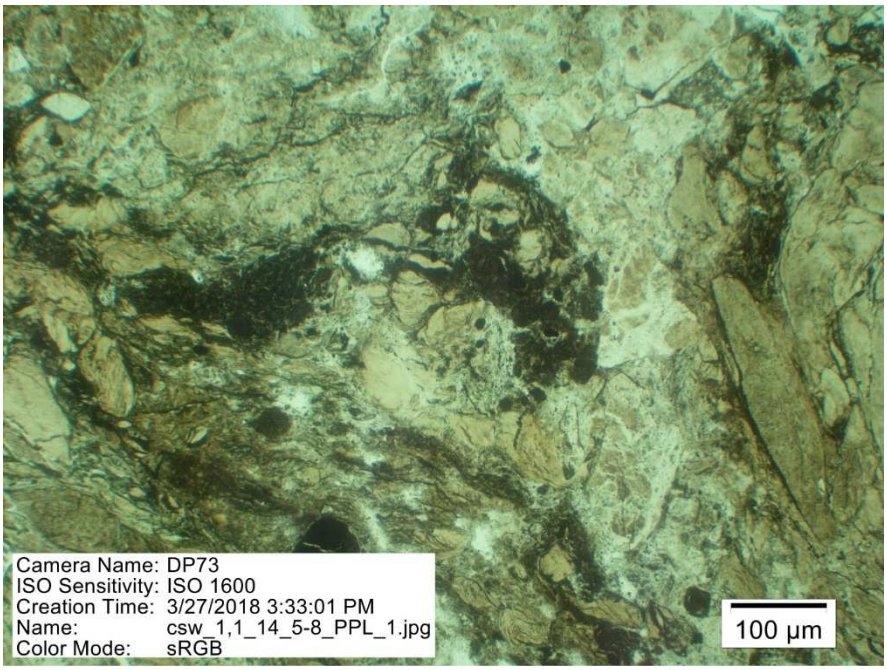

Figure 13. Representative photomicrograph of CSW_1,1_14_5-8, at 10x under plain polarized light consisting of largely serpentinized peridotite from the Coast Range Ophiolite obtained at the McLaughlin Natural Research Reserve.

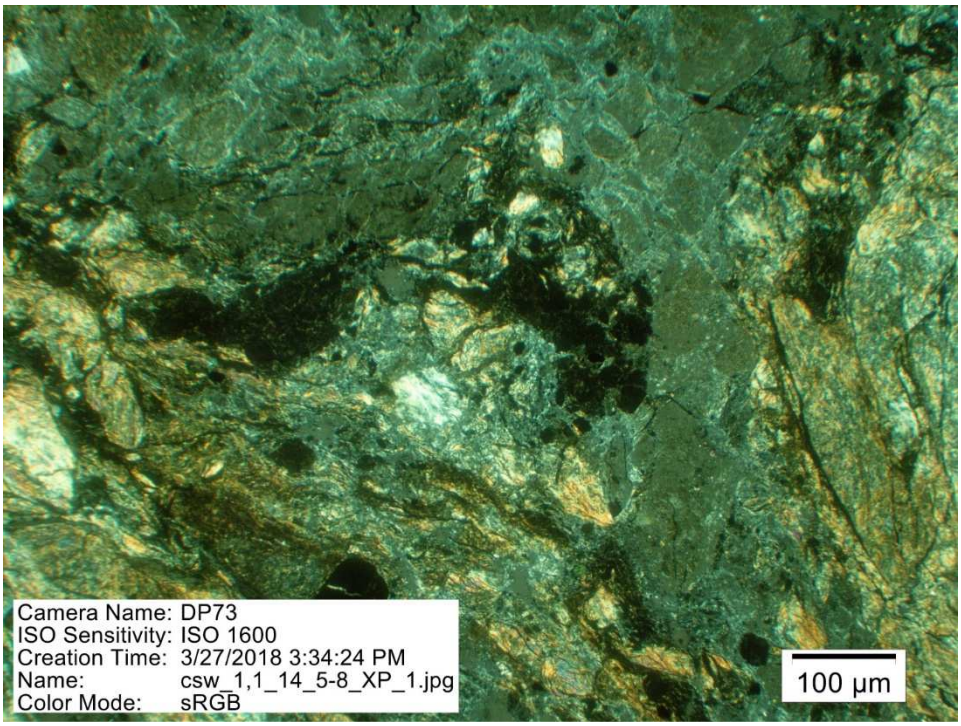

Figure 14. Representative photomicrograph of CSW_1,1_14_5-8, at 10x under cross polarized light consisting of largely serpentinized peridotite with evidence of higher order interference colors in approximately 15% of the sample from the Coast Range Ophiolite obtained at the McLaughlin Natural Research Reserve.

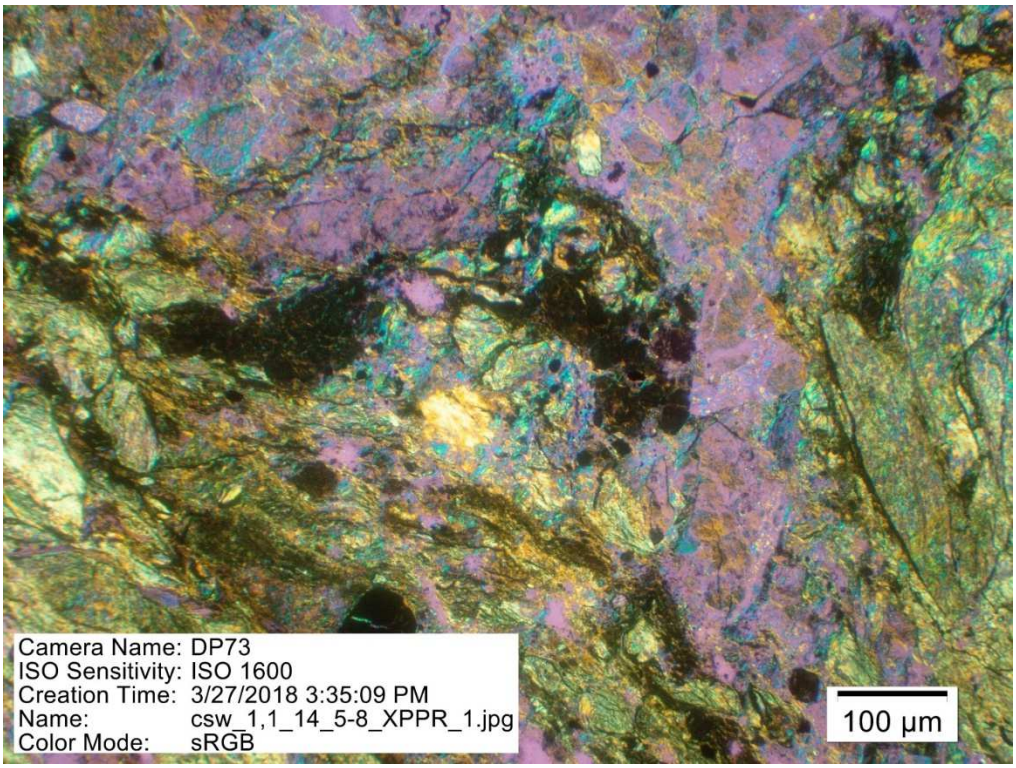

Figure 15. Representative photomicrograph of CSW_1,1_14_5-8, at 10x under cross polarized light with the retardation plate inserted consisting of largely serpentinized peridotite with evidence of higher order interference colors in approximately 15% of the sample from the Coast Range Ophiolite obtained at the McLaughlin Natural Research Reserve.

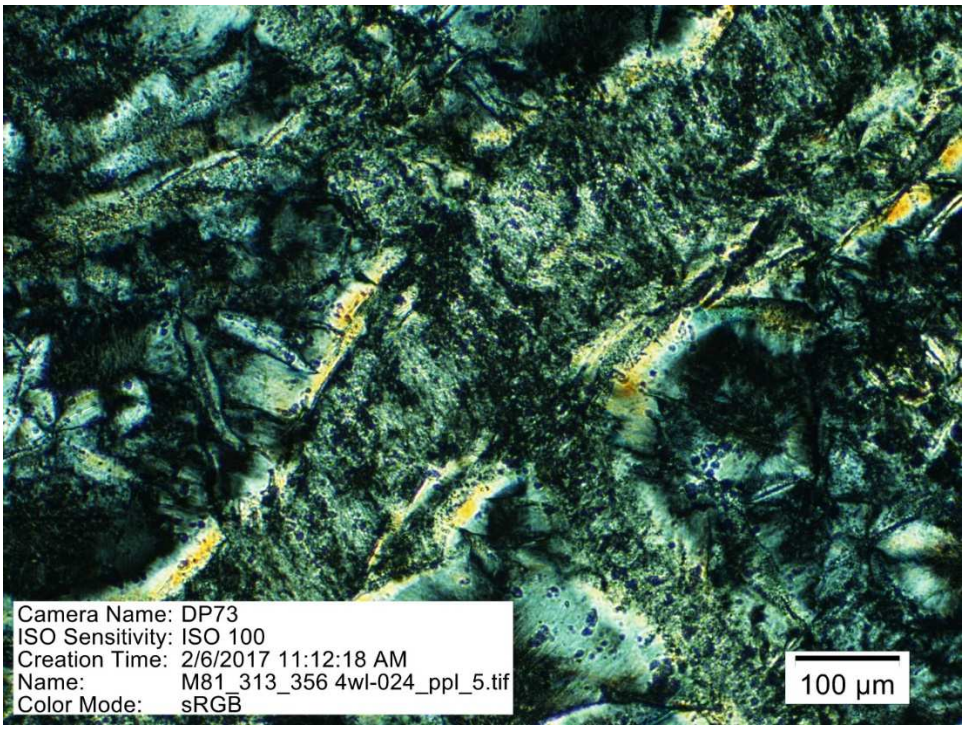

Figure 16. Representative photomicrograph of M81_313_356 at 10x under cross polarized light consisting of largely serpentinized peridotite with evidence of higher order interference colors in approximately 10% of the sample from the Coast Range Ophiolite obtained at the McLaughlin Natural Research Reserve. Fine chrysotile fibrous veins are noticeable here.

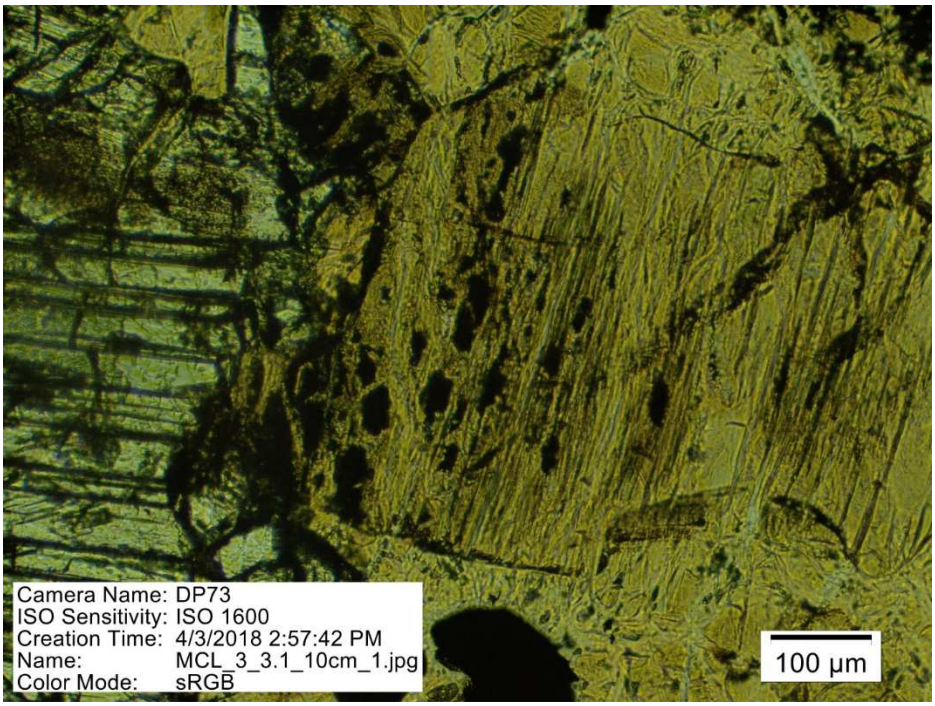

Figure 17. Representative photomicrograph of MCL_3_3.1_10cm at x under plain polarized light, consisting of largely serpentinized peridotite from the Coast Range Ophiolite obtained at the McLaughlin Natural Research Reserve.

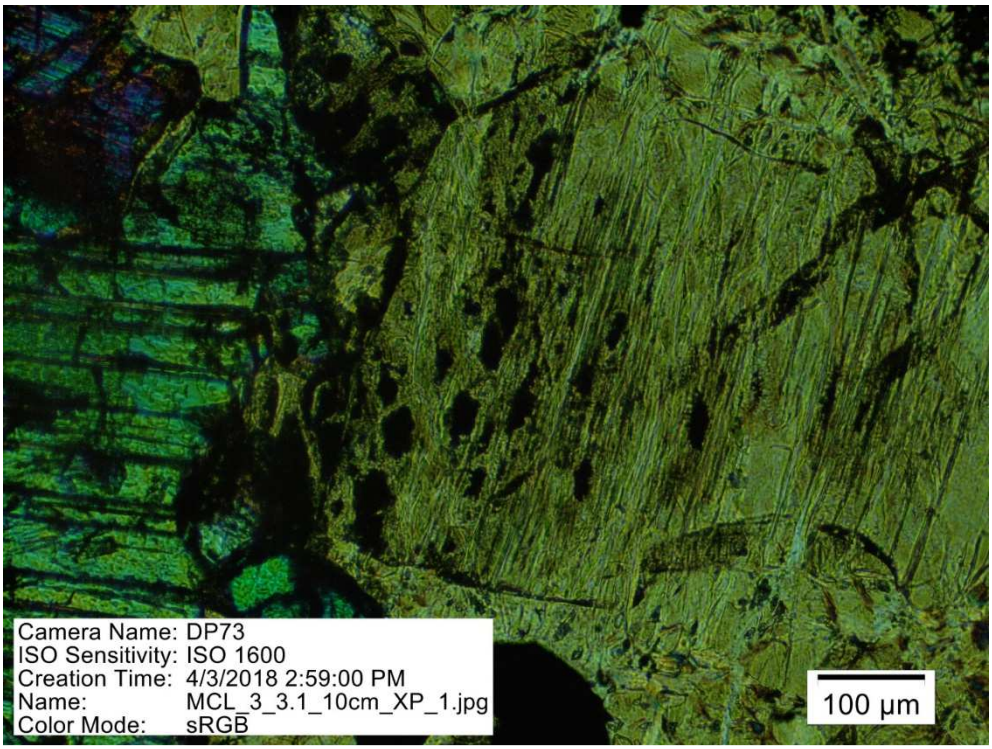

Figure 18. Representative photomicrograph of MCL_3_3.1_10cm at x cross plain polarized light, consisting of largely serpentinized peridotite from the Coast Range Ophiolite obtained at the McLaughlin Natural Research Reserve.

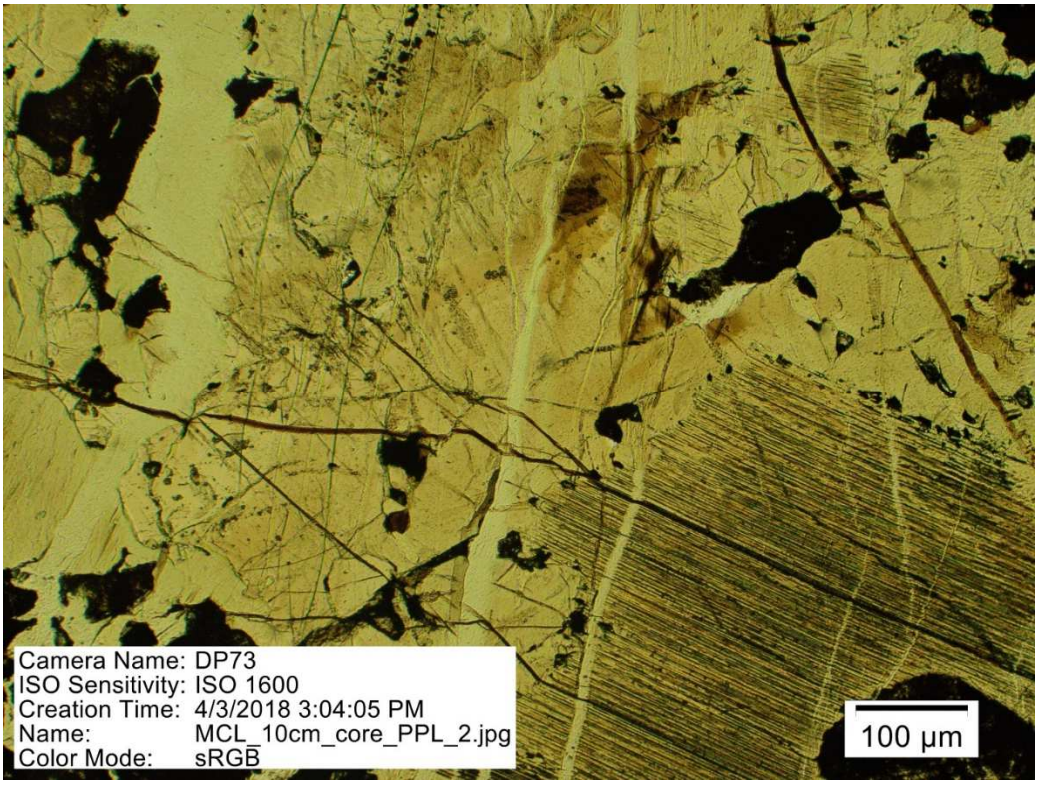

Figure 19. Representative photomicrograph of MCL surface core at 10x under plain polarized light, consisting of largely serpentinized peridotite from the Coast Range Ophiolite obtained at the McLaughlin Natural Research Reserve.

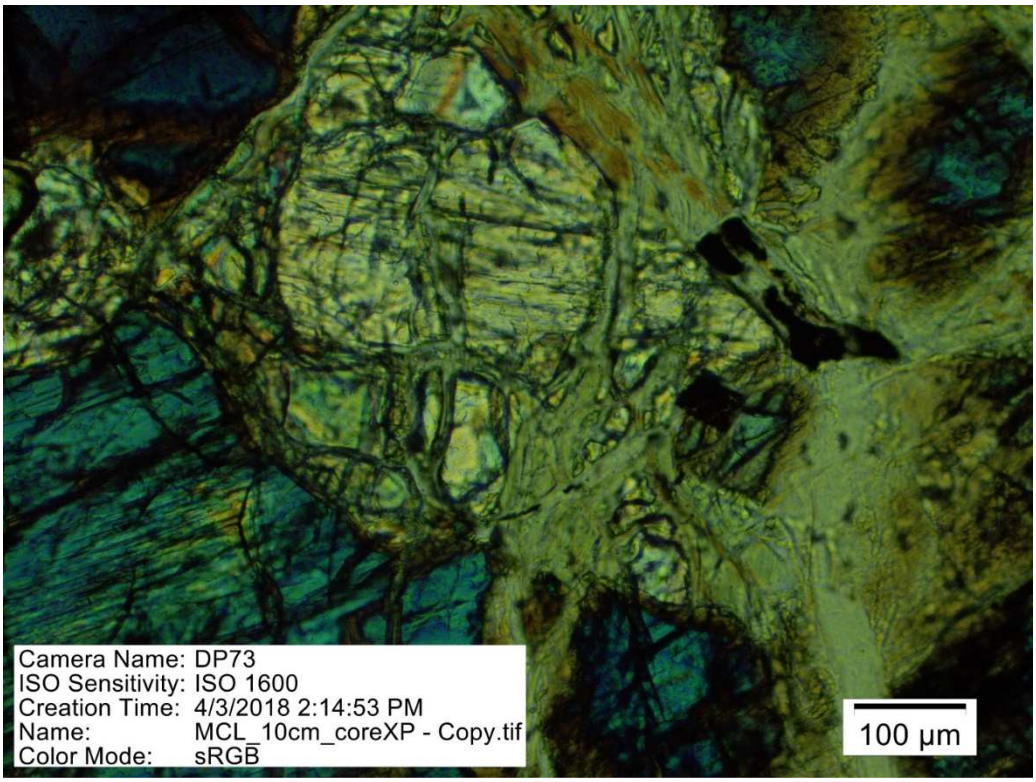

Figure 20. Representative photomicrograph of MCL surface core at 10x under cross polarized light, consisting of largely serpentinized peridotite from the Coast Range Ophiolite obtained at the McLaughlin Natural Research Reserve.

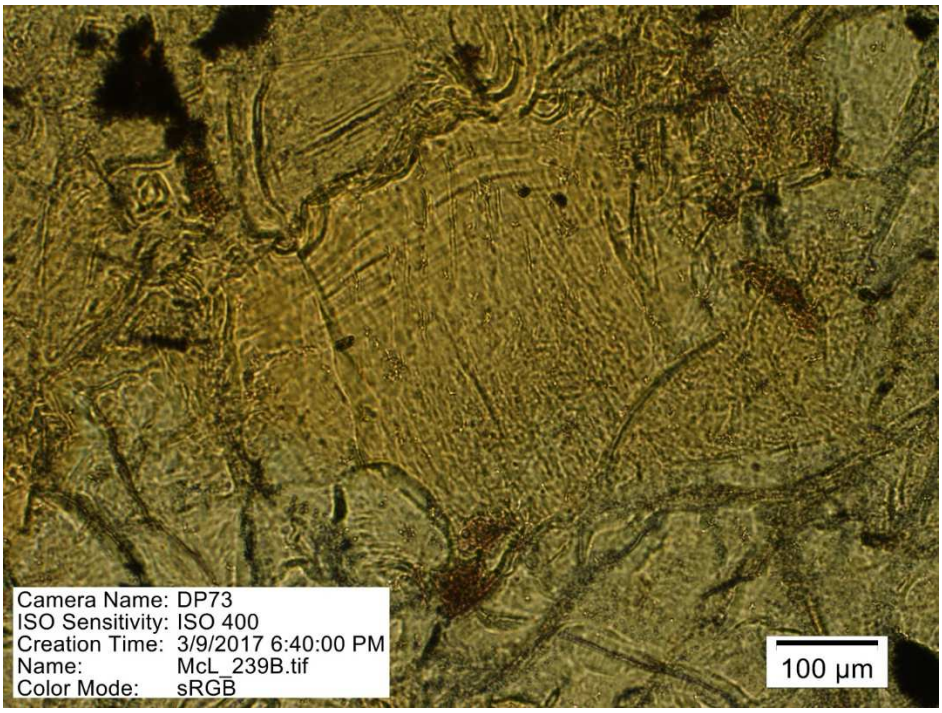

Figure 21. Representative photomicrograph of MCL_239B core under plain polarized light, consisting of largely serpentinized peridotite from the Coast Range Ophiolite obtained at the McLaughlin Natural Research Reserve.

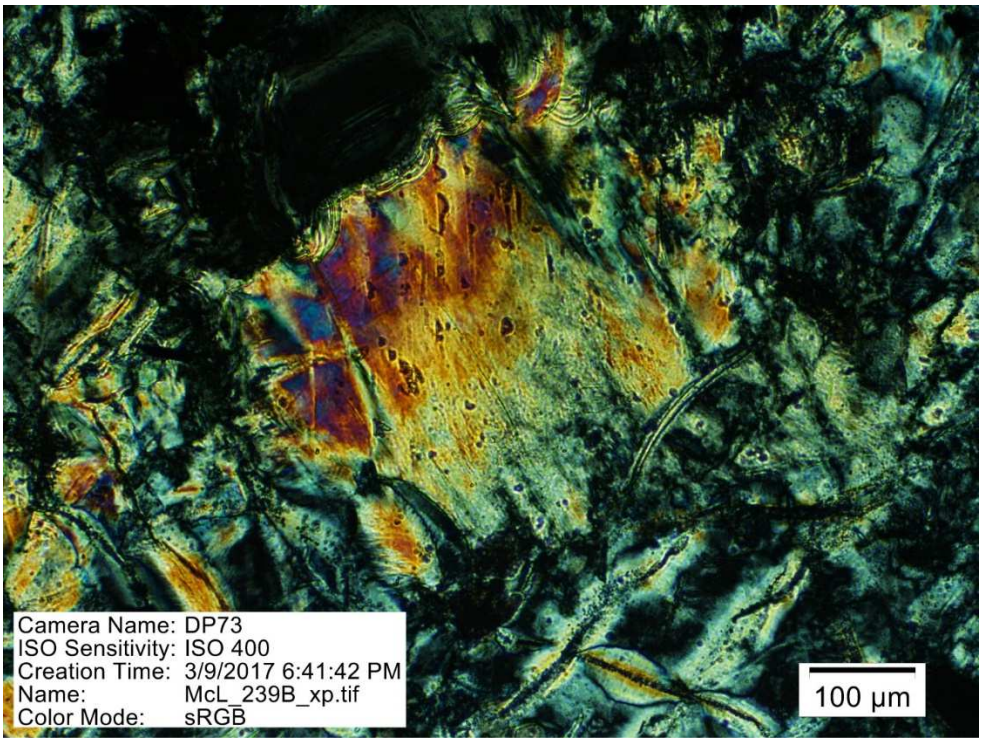

Figure 22. Representative photomicrograph of MCL_239B core under cross polarized light at 10x, consisting of largely serpentinized peridotite with evidence of higher order interference colors in approximately 10% of the sample from the Coast Range Ophiolite obtained at the McLaughlin Natural Research Reserve.

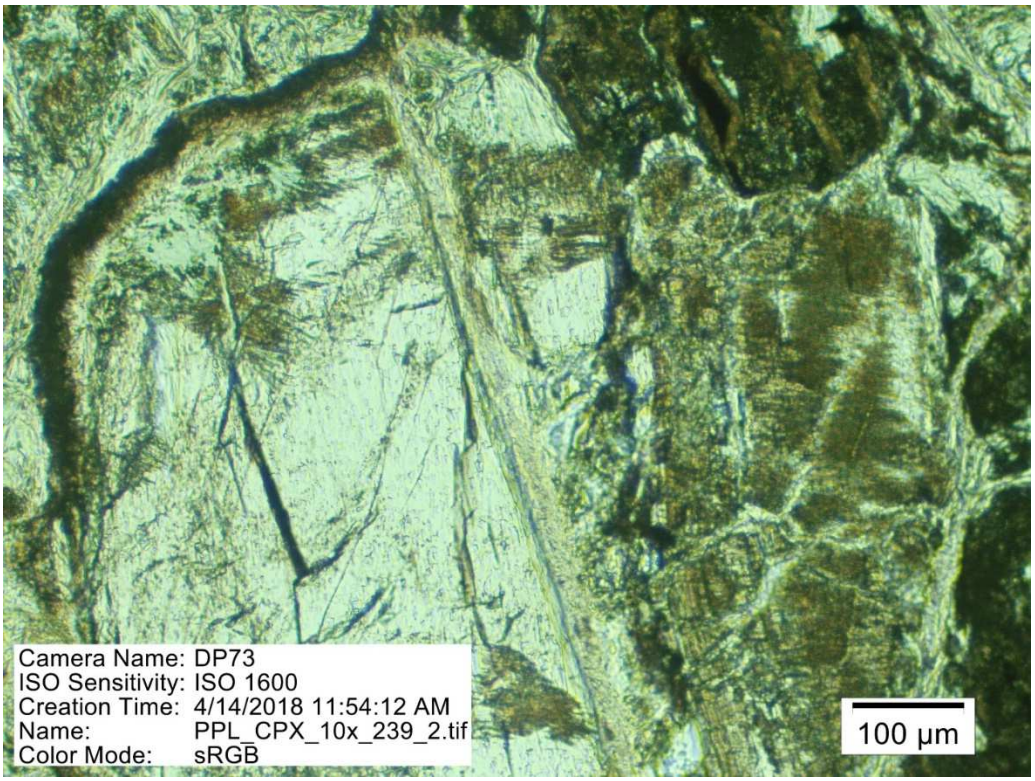

Figure 23. Representative photomicrograph of MCL_239_2 core under plain polarized light at 10x, consisting of largely serpentinized peridotite from the Coast Range Ophiolite obtained at the McLaughlin Natural Research Reserve.

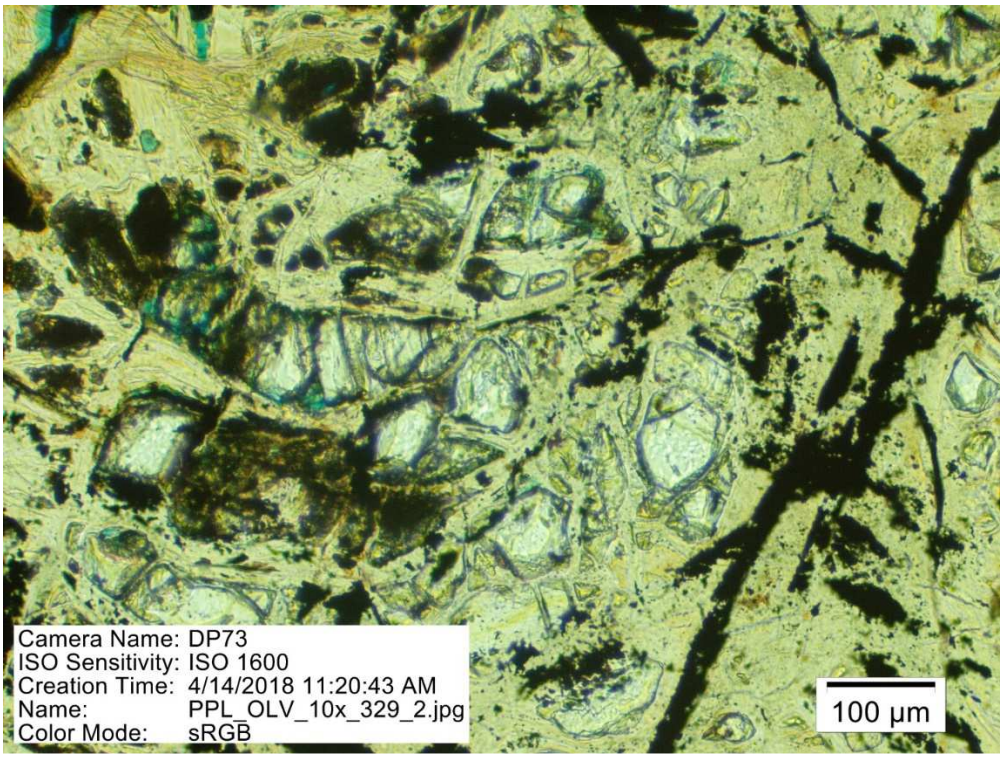

Figure 24. Representative photomicrograph of MCL_329_2 core under plain polarized light at 10x, consisting of largely serpentinized peridotite with evidence of high relief crystals in approximately 30% of the sample from the Coast Range Ophiolite obtained at the McLaughlin Natural Research Reserve.

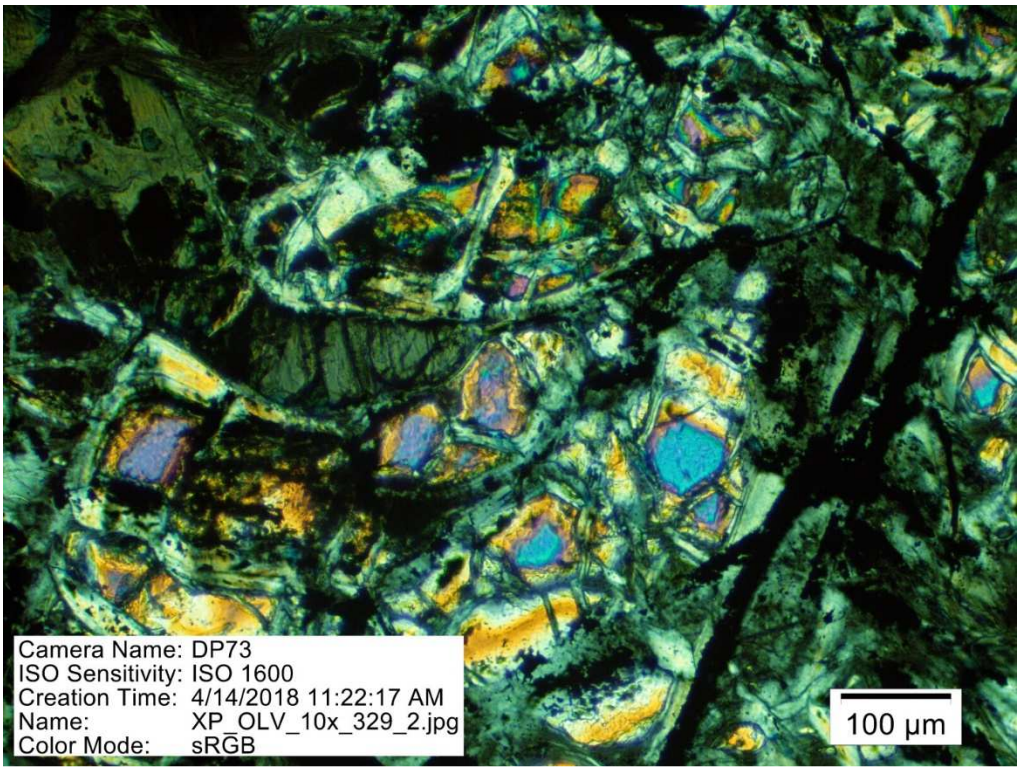

Figure 25. Representative photomicrograph of MCL_329_2 core under plain polarized light at 10x, consisting of largely serpentinized peridotite with evidence of high relief crystals in approximately 30% of the sample from the Coast Range Ophiolite obtained at the McLaughlin Natural Research Reserve.

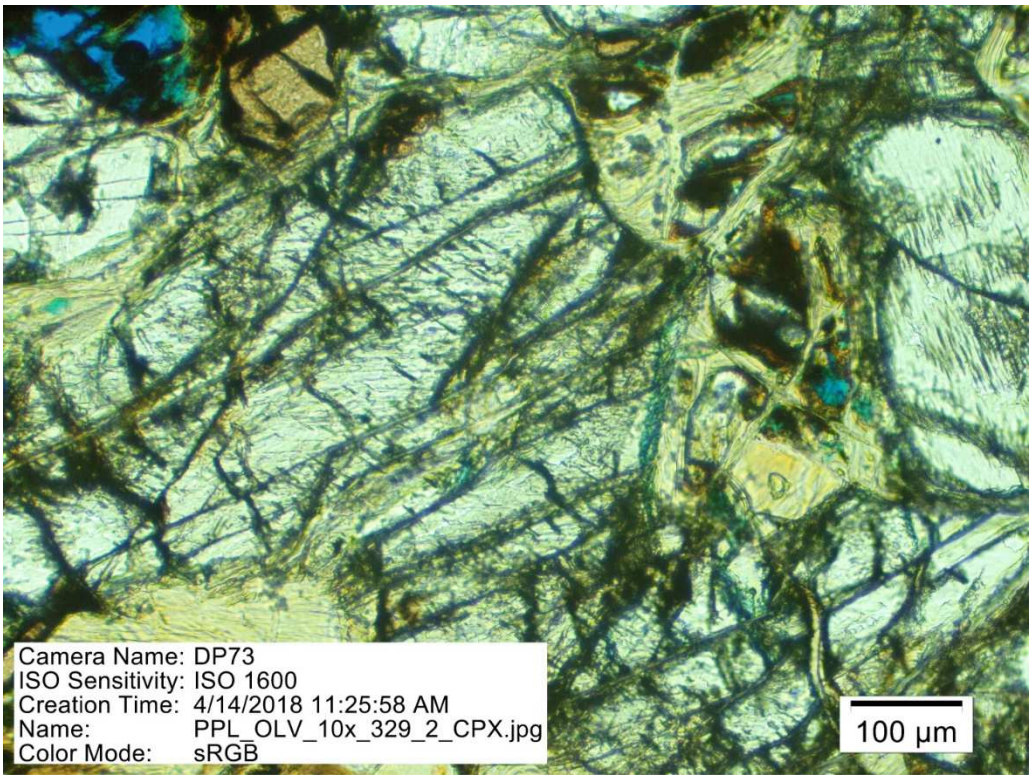

Figure 2. Representative photomicrograph of MCL_329_2 core under plain polarized light at 10x, consisting of serpentinized peridotite with evidence of high relief crystals of olivines and orthopyroxene fractures in approximately 40% of the sample from the Coast Range Ophiolite obtained at the McLaughlin Natural Research Reserve.

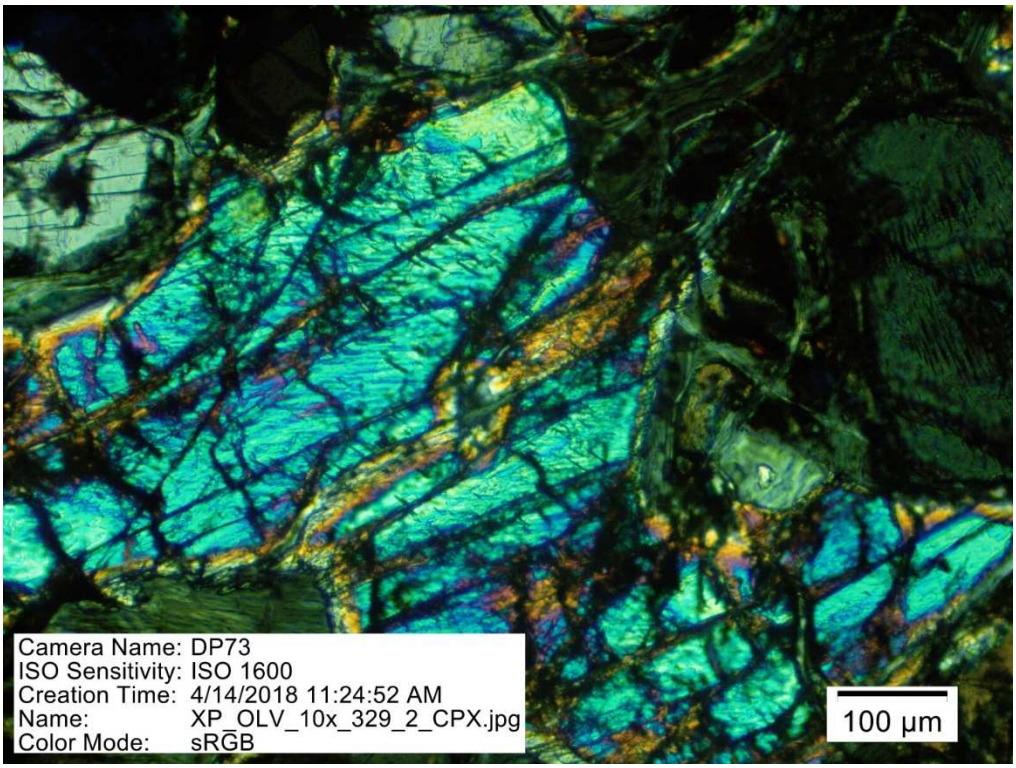

Figure 27. Representative photomicrograph of MCL_329_2 core under cross polarized light at 10x, consisting of serpentinized peridotite with evidence of high relief crystals of olivines and orthopyroxene fractures in approximately 40% of the sample from the Coast Range Ophiolite obtained at the McLaughlin Natural Research Reserve, showing second order interference blue color.

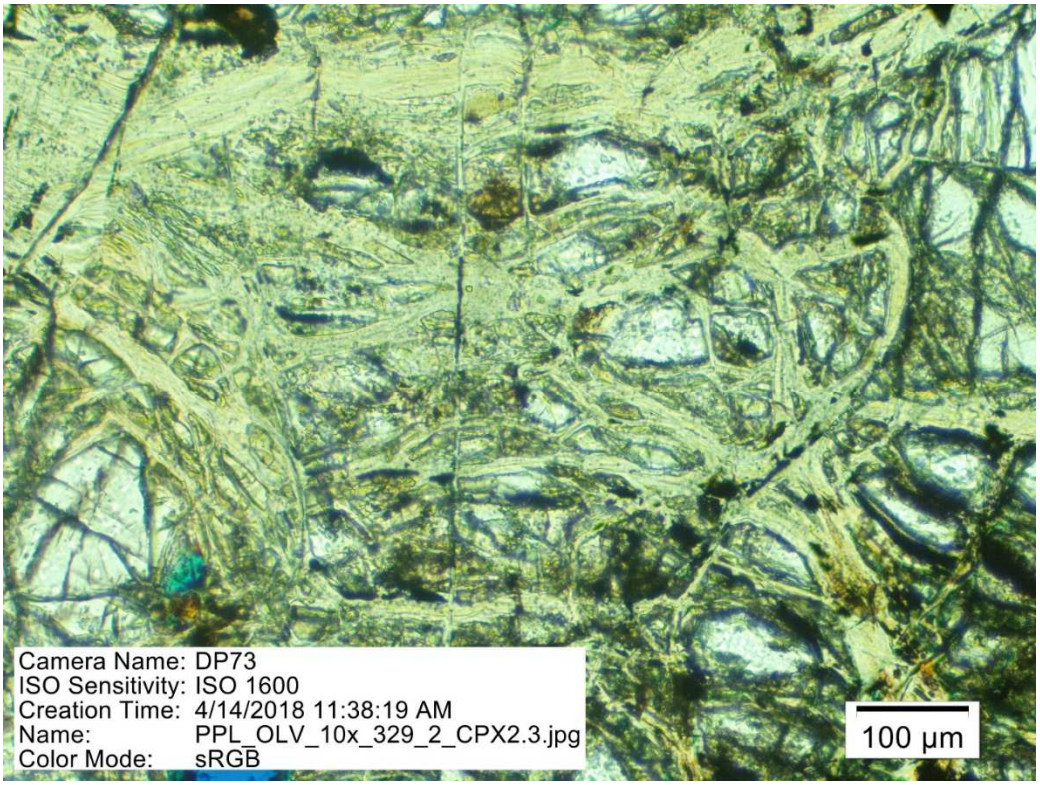

Figure 28. Representative photomicrograph of MCL_329_2 core under plain polarized light at 10x, consisting of serpentinized peridotite with evidence of high relief crystals of olivines and fractures of clinopyroxene fractures in approximately 20% of the sample from the Coast Range Ophiolite obtained at the McLaughlin Natural Research Reserve.

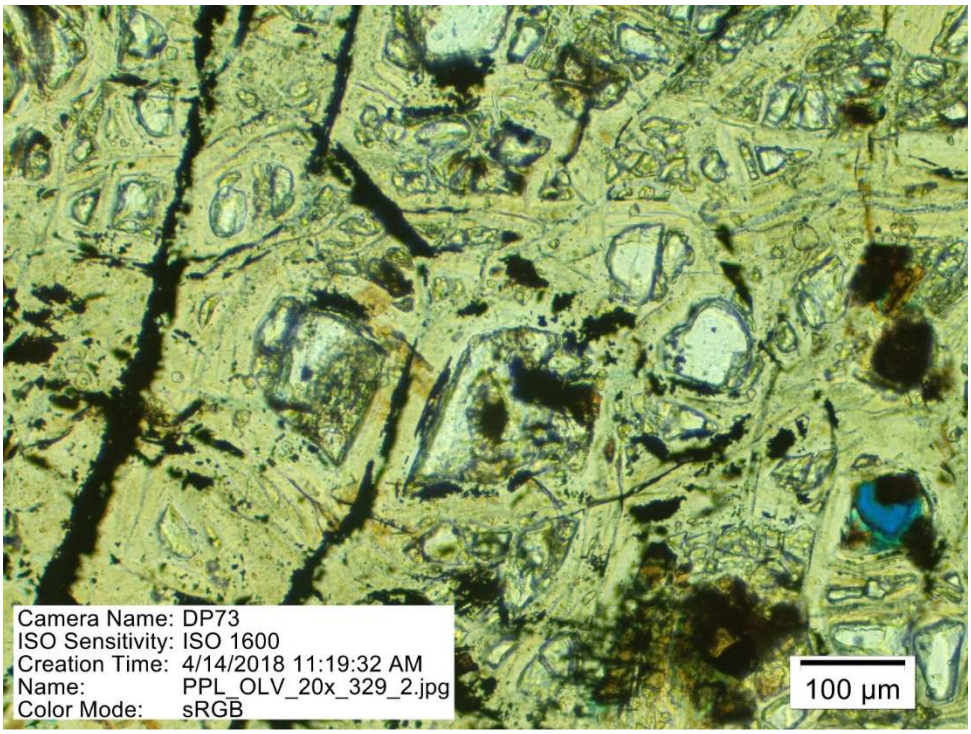

Figure 29. Representative photomicrograph of MCL_329_2 core under plain polarized light at 10x, consisting of serpentinized peridotite with evidence of high relief crystals of olivines 30% of the sample from the Coast Range Ophiolite obtained at the McLaughlin Natural Research Reserve.

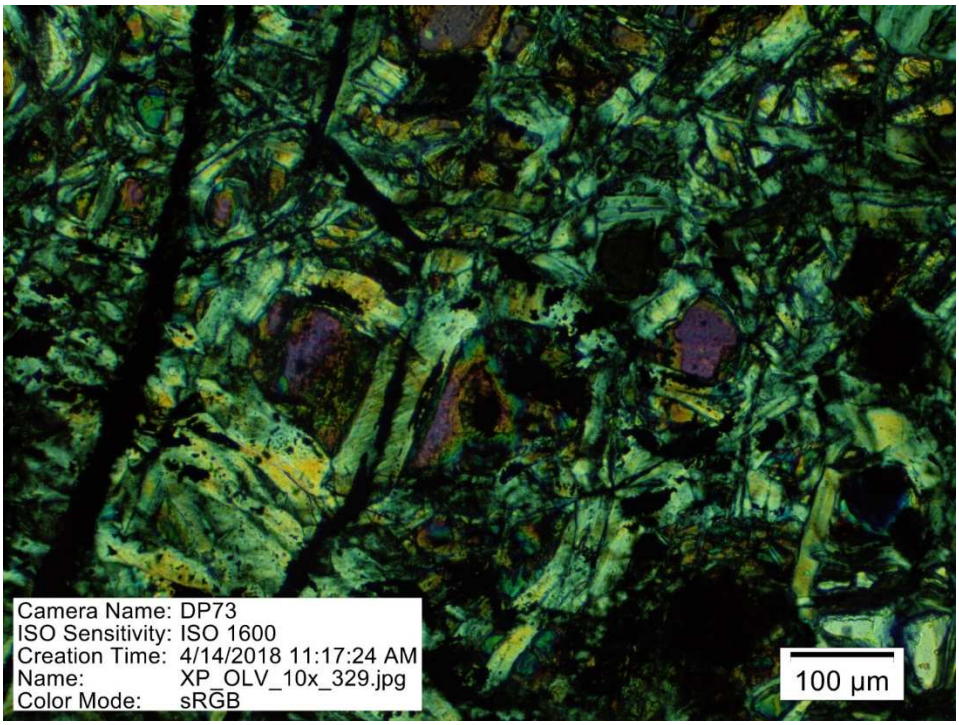

Figure 30. Representative photomicrograph of MCL_329_2 core under cross polarized light at 10x, consisting of largely serpentinized peridotite with evidence of high relief crystals olivine and second order interference colors in approximately 30% of the sample from the Coast Range Ophiolite obtained at the McLaughlin Natural Research Reserve.

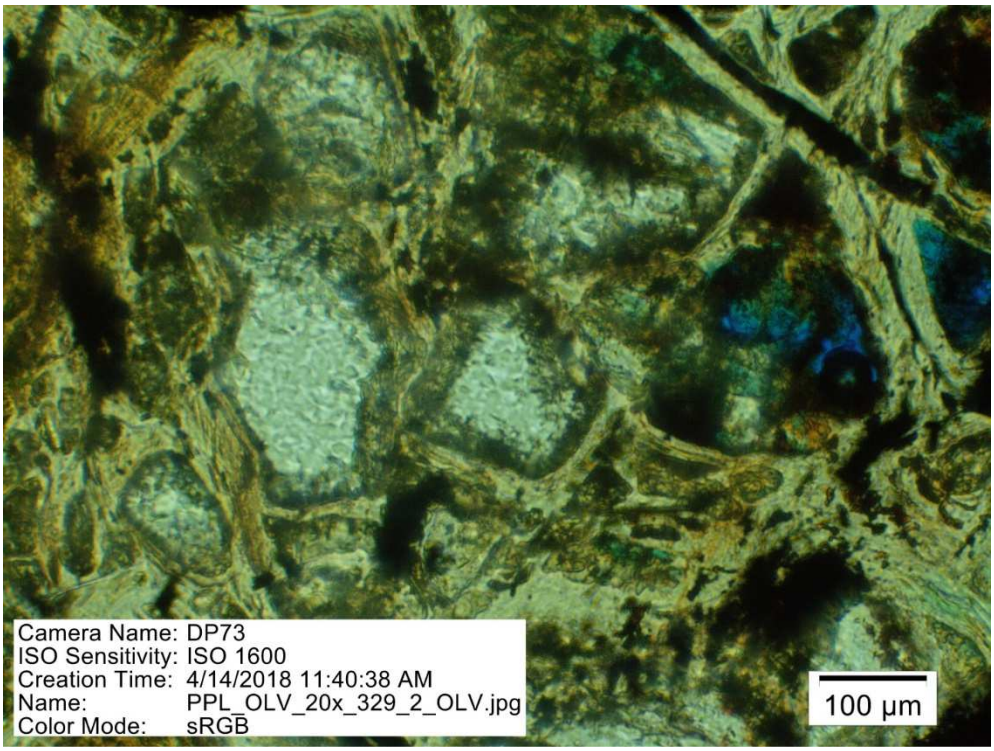

Figure 31. Representative photomicrograph of MCL_329_2 core under plain polarized light at 20x, consisting of serpentinized peridotite with evidence of high relief crystals of olivines 35% of the sample from the Coast Range Ophiolite obtained at the McLaughlin Natural Research Reserve.

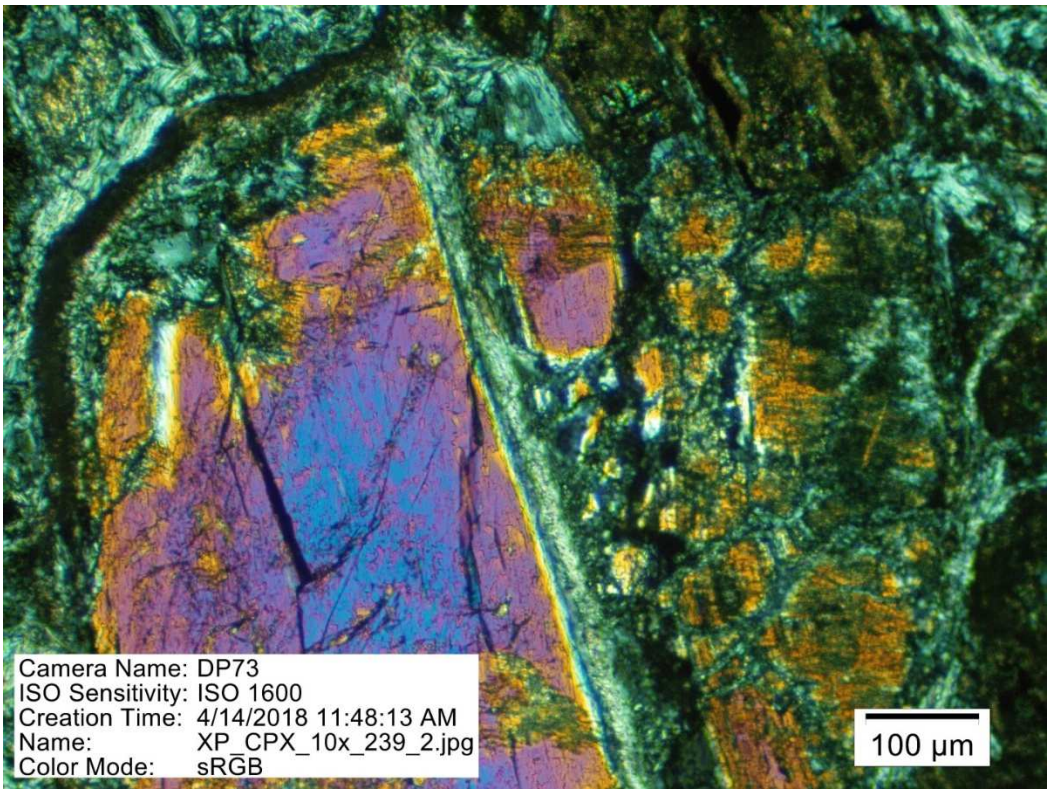

Figure 32. Representative photomicrograph of MCL_239_2 core under cross polarized light at 10x, consisting of largely serpentinized peridotite with evidence of fracturing and zonation of reaction, likely in a clinopyroxene that displays second order interference colors in approximately 30% of the sample from the Coast Range Ophiolite obtained at the McLaughlin Natural Research Reserve. Olivine could be along the serpentine fraction on the right side.

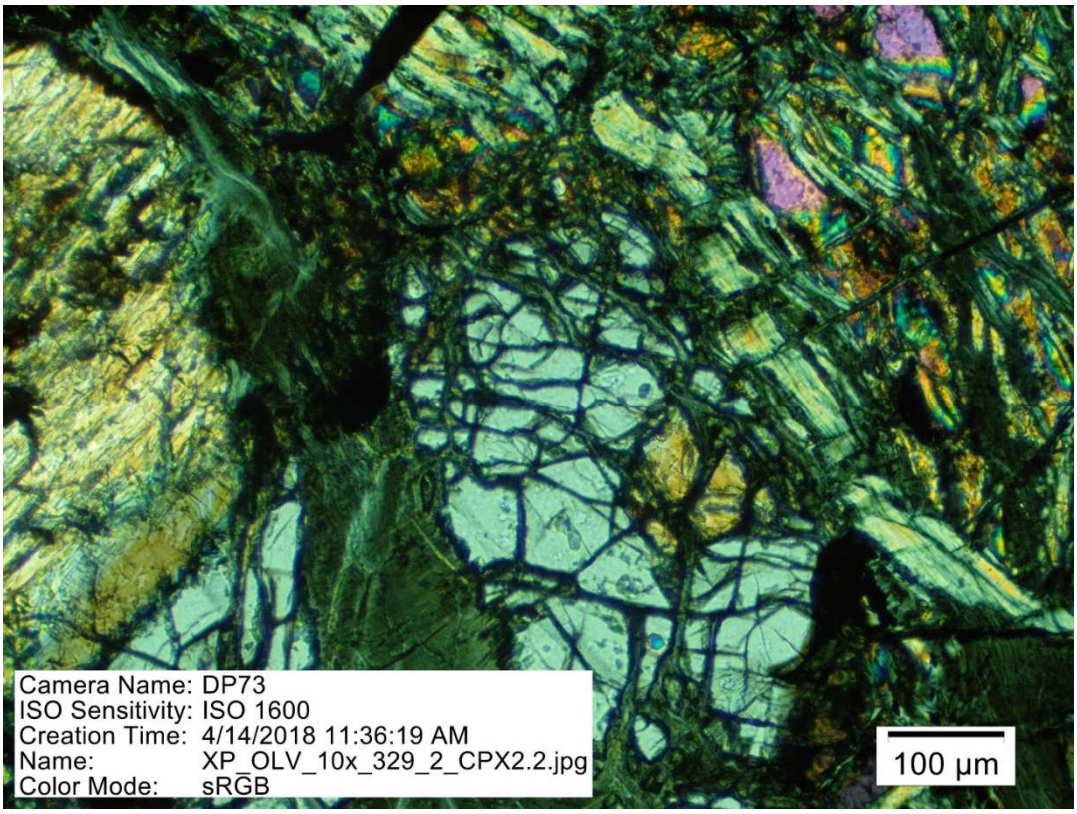

Figure 33. Representative photomicrograph of MCL_392_2 core under cross polarized light at 10x, consisting of largely serpentinized peridotite with evidence of fracturing and zonation of reaction, likely in a clinopyroxene that displays second order interference colors in approximately 30% of the sample from the Coast Range Ophiolite obtained at the McLaughlin Natural Research Reserve. Olivine could be along the serpentine chrysotile vein, on the upper right corner of the slide. Also, the imperfect 90 degree cleavage.

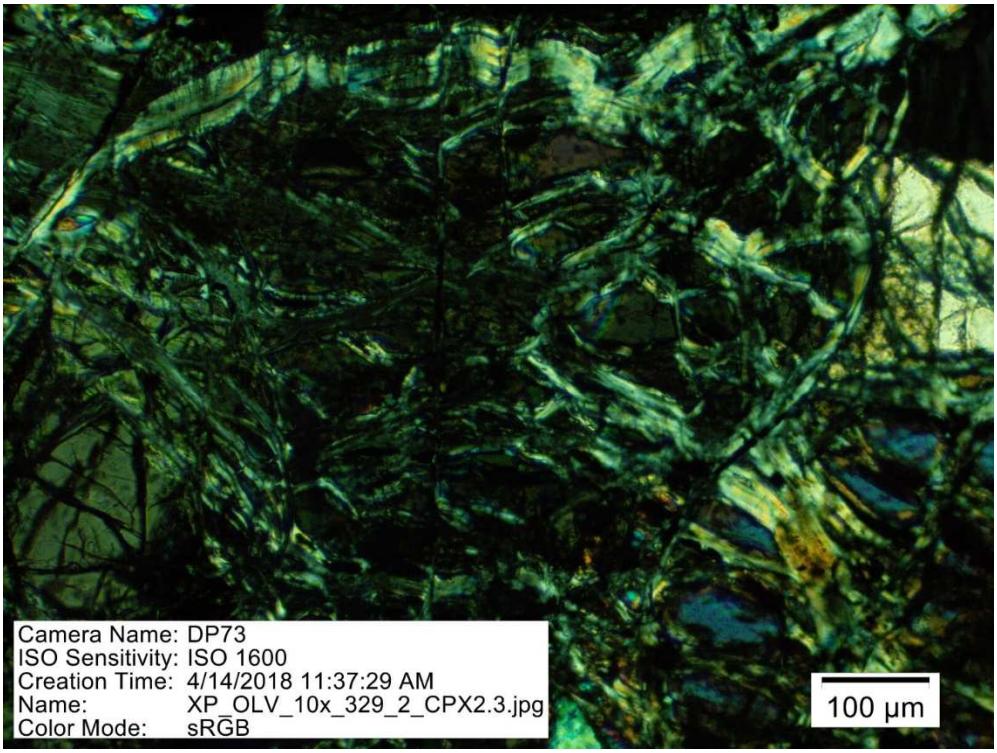

Figure 34. Representative photomicrograph of MCL_392_2 core under cross polarized light at 10x, rotated 45 degrees consisting of largely serpentinized peridotite with evidence of fracturing and zonation of reaction, likely in a clinopyroxene that displays second order interference colors in approximately 30% of the sample from the Coast Range Ophiolite obtained at the McLaughlin Natural Research Reserve. Olivine could be along the serpentine chrysotile vein, on the upper right corner of the slide. This show the pleochroism of the previous slide.

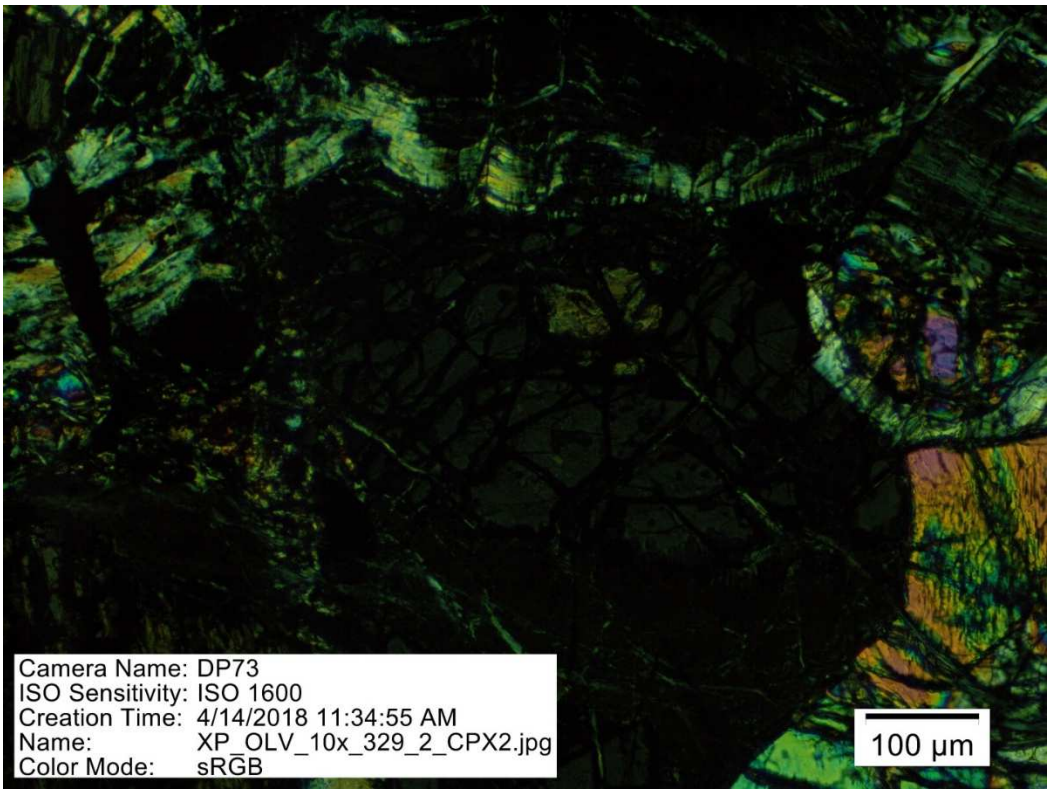

Figure 35. Representative photomicrograph of MCL_392_2 core under cross polarized light at 10x, rotated 90 degrees consisting of largely serpentinized peridotite with evidence of fracturing and zonation of reaction, likely in a clinopyroxene that displays second order interference colors in approximately 30% of the sample from the Coast Range Ophiolite obtained at the McLaughlin Natural Research Reserve. Olivine could be along the serpentine chrysotile vein, on the upper right corner of the slide. This show another angle of the pleochroism of the previous slide.

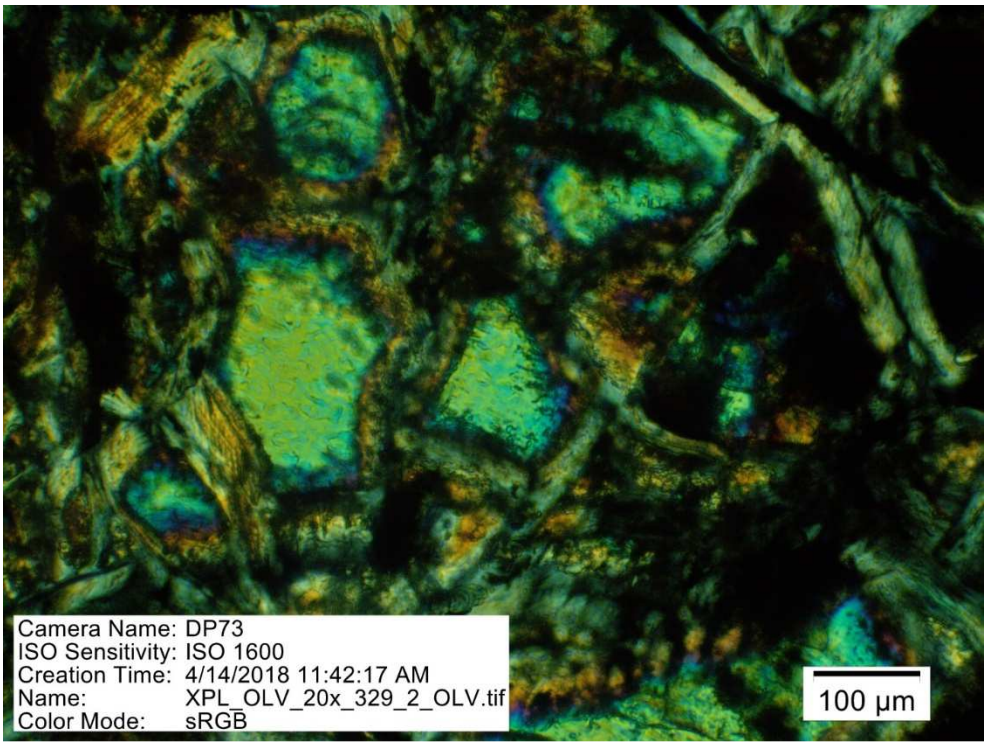

Figure 36. Representative photomicrograph of MCL_392_2 core under cross polarized light at 20x, rotated 90 degrees consisting of largely serpentinized peridotite with evidence of fracturing and zonation of reaction, in an olivine that displays second order interference colors in approximately 30% of the sample from the Coast Range Ophiolite obtained at the McLaughlin Natural Research Reserve.

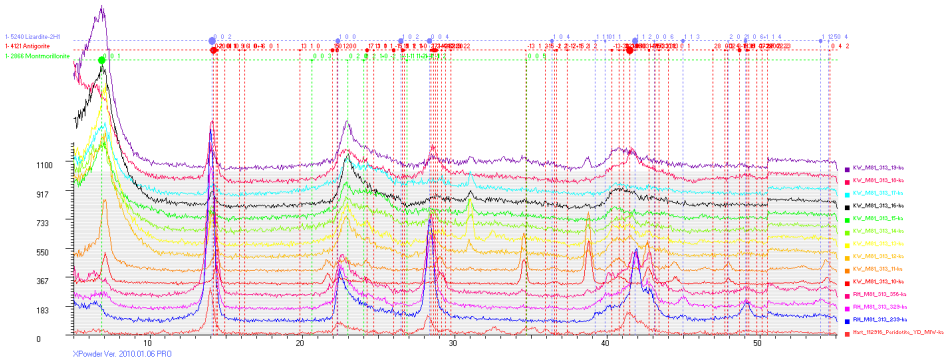

Figure 37. Representative XRD diffractogram of M81_313_10 to M81_313_19 with M81_313_356, M81_313_329 and M81_313_239 showing the presence of serpentine polymorphs and serpentinization products from highly serpentinized peridotite from the Coast Range Ophiolite obtained at the McLaughlin Natural Research Reserve. Yellow Dog Peridotite was used as a representative sample as a standard obtained from Wards. Minerals identified include 1-5240 Lizardite-2H1, 1-4121 Antigorite, 1-2866 Montmorillonite.

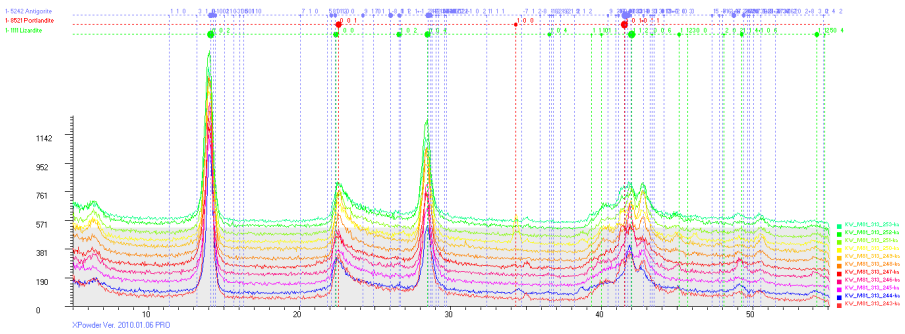

Figure 38. Representative XRD diffractogram of M81_313_243 to M81_313_253 showing the presence 1-5242 Antigorite, 1-8521 Portlandite, and 1-111 Lizardite from highly serpentinized peridotite from the Coast Range Ophiolite obtained at the McLaughlin Natural Research Reserve.

1-5242 Antigorite
1-8521 Portlandite
1-111 Lizardite

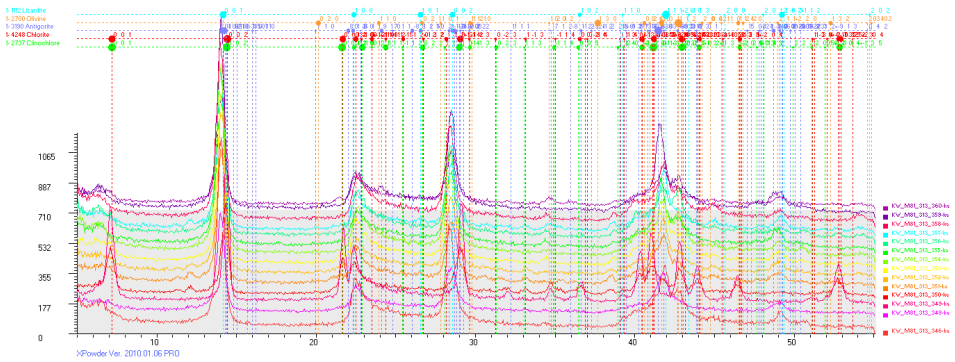

Figure 39. Representative XRD diffractogram M81_313_346 to M81_313_360 showing the presence from 1-112 Lizardite, 1-2700 Olivine, 1-3190 Antigorite, 1-4248 Chlorite, and 1-2737 Clinochlore highly serpentinized peridotite from the Coast Range Ophiolite obtained at the McLaughlin Natural Research Reserve.

1-112 Lizardite
1-2700 Olivine
1-3190 Antigorite
1-4248 Chlorite
1-2737 Clinochlore

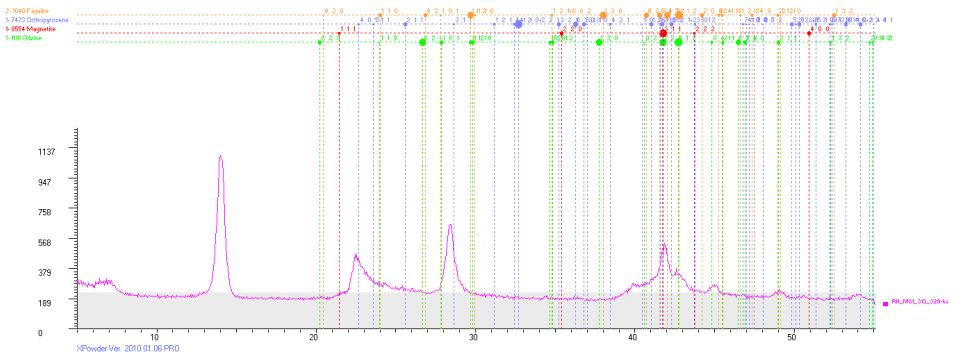

Figure 40. Representative XRD diffractogram M81_313_329 showing the presence from 2-1040 Fayalite, 1-7473 Orthopyroxene, 1-8554 Magnetite, and 1-1116 Olivine highly serpentinized peridotite from the Coast Range Ophiolite obtained at the McLaughlin Natural Research Reserve.

2-1040 Fayalite
1-7473 Orthopyroxene
1-8554 Magnetite
1-1116 Olivine

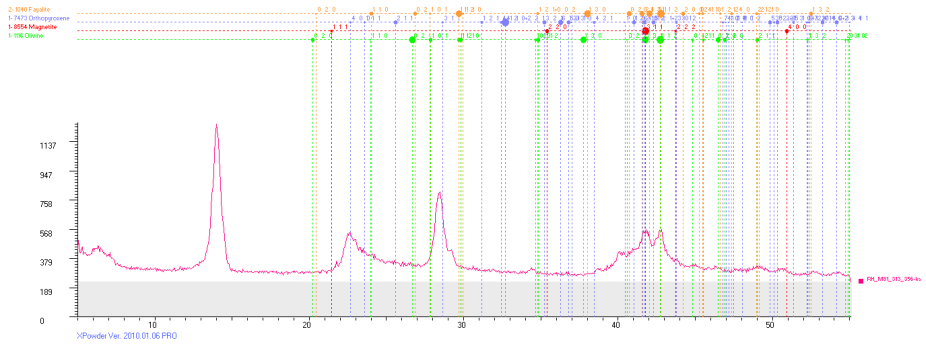

Figure 41. Representative XRD diffractogram M81_313_356 showing the presence from 2-1040 Fayalite, 1-7473 Orthopyroxene, 1-8554 Magnetite, and 1-1116 Olivine highly serpentinized peridotite from the Coast Range Ophiolite obtained at the McLaughlin Natural Research Reserve.

2-1040 Fayalite
1-7473 Orthopyroxene
1-8554 Magnetite
1-1116 Olivine

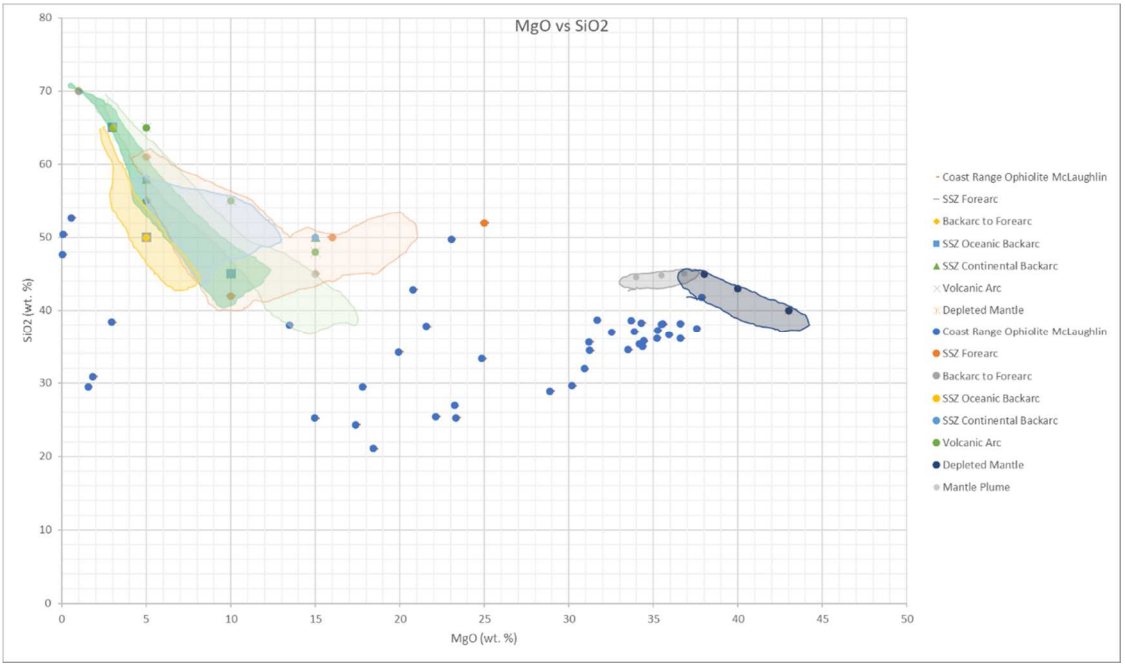

Figure 42. MgO vs SiO_2 plot showing the placement of various geochemically derived tectonic settings associated with ophiolites. Values are sparsely located but fall generally in a depleted silica and enriched magnesium zone. Few points plot in the supra-subduction zone (SSZ), backarc to forearc (Backarc to Forearc), forearc (SSZ Forearc), oceanic backarc (SSZ Oceanic Backarc), and continental backarc (SSZ Continental Backarc), which are mean values from Dilek & Furnes (2011). Mean values plot in a significantly lower silica zone than these representative types. Furthermore, these samples also plot lower in silica than depleted mantle (Depleted Mantle) and mantle plume.

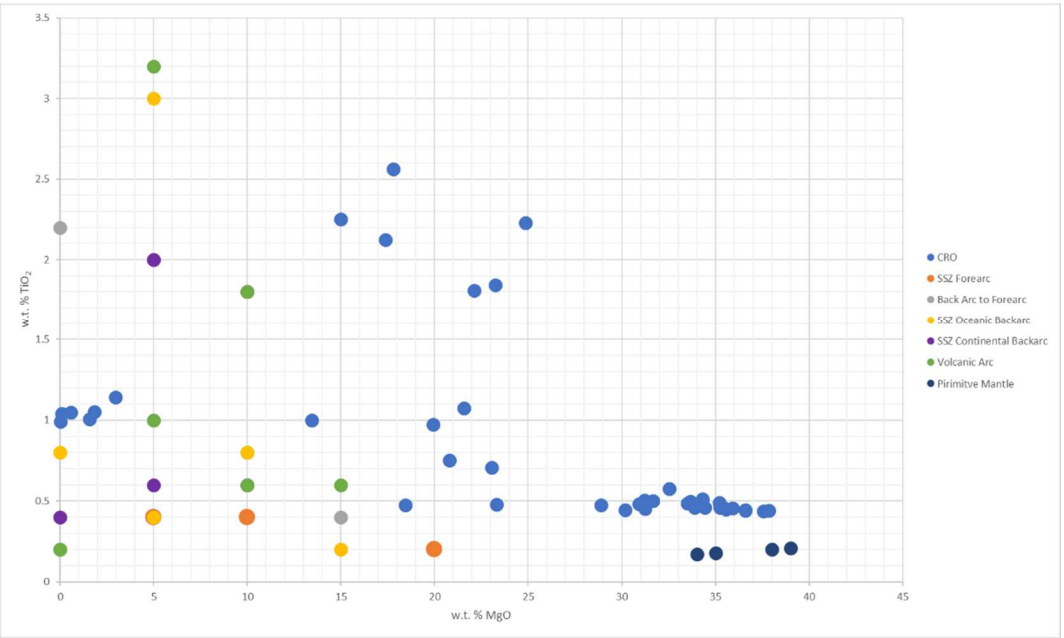

Figure 43. MgO vs TiO_2 plot showing the placement of various geochemically derived tectonic settings associated with ophiolites. Values are sparsely located but fall in two generalized patters. The supra-subduction zone (SSZ), backarc to forearc (Backarc to Forearc), forearc (SSZ Forearc), oceanic backarc (SSZ Oceanic Backarc), and continental backarc (SSZ Continental Backarc) are defined by mean values in Dilek & Furnes (2011). CRO values of samples QV 135, 337, QV 137, 326, QV 137.1, 335 all plot near the primitive mantle zone and other samples plot above the SSZ Forearc and populate regions of the backarc to forearc (Backarc to Forearc), forearc (SSZ Forearc), oceanic backarc (SSZ Oceanic Backarc), and continental backarc (SSZ Continental Backarc).

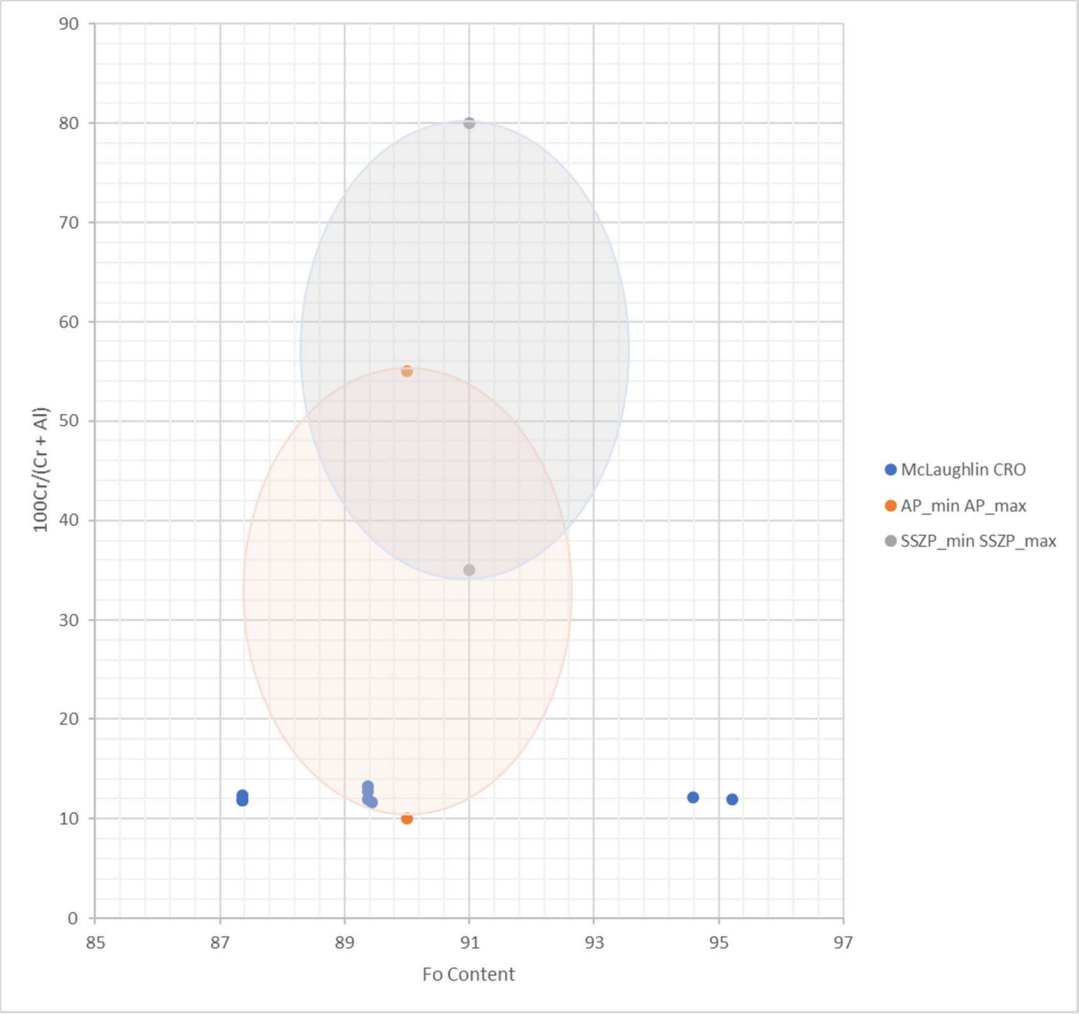

Figure 44. Spinel and Fo content of coexisting olivine showing major zones of abyssal peridotites and supra-subduction zone peridotites from Choi et al. (2008). CRO rocks from McLaughlin plot variably, with few samples plotting in the abyssal peridotites zone.

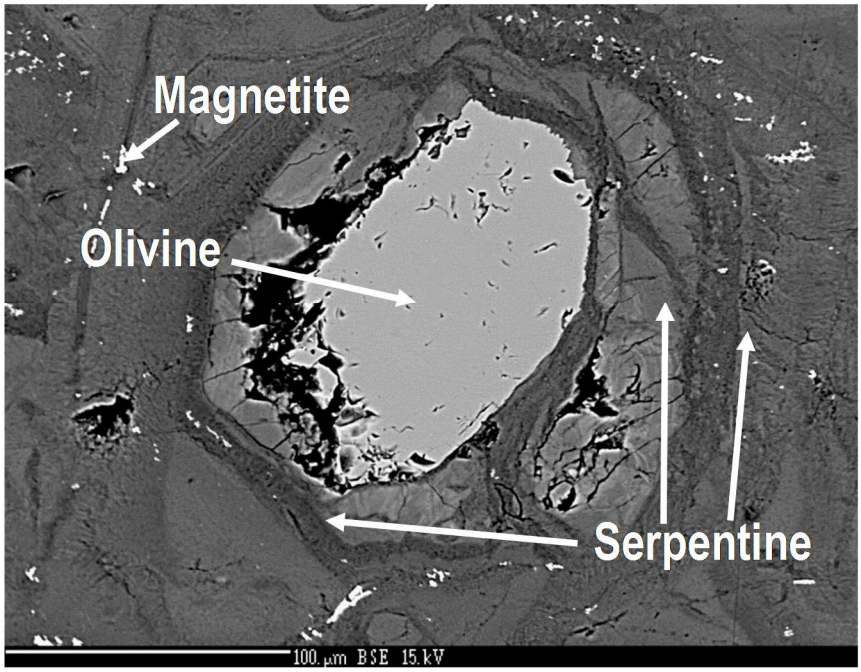

Figure 45. Backscattered electron image of serpentinization ongoing on a crystal of olivine from McL_313_329 obtained at the Brown University EMP Facility.

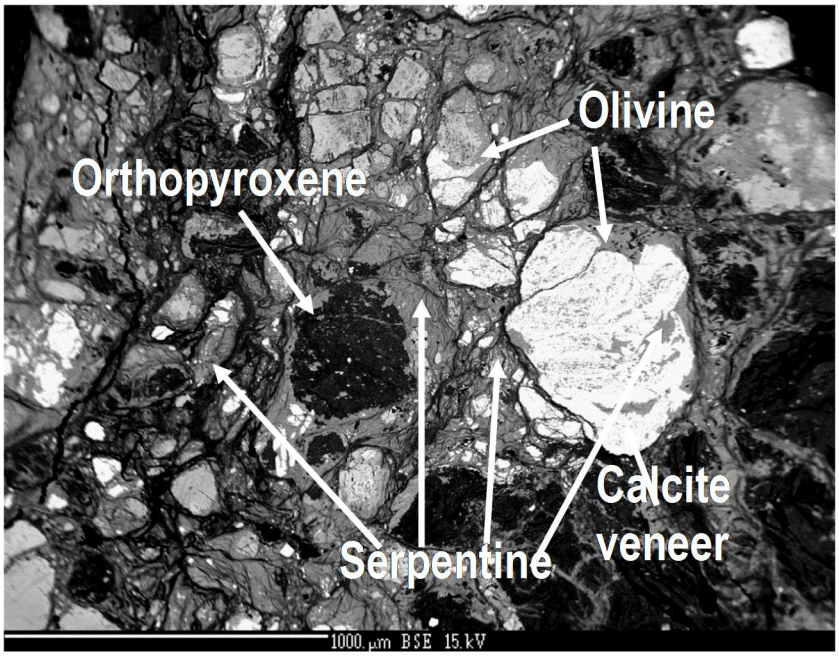

Figure 46. Backscattered electron image of serpentinization ongoing on a crystal of olivine from McL_313_239A obtained at the Brown University EMP Facility showing pervasive serpentinization of multiple crystals of olivine.

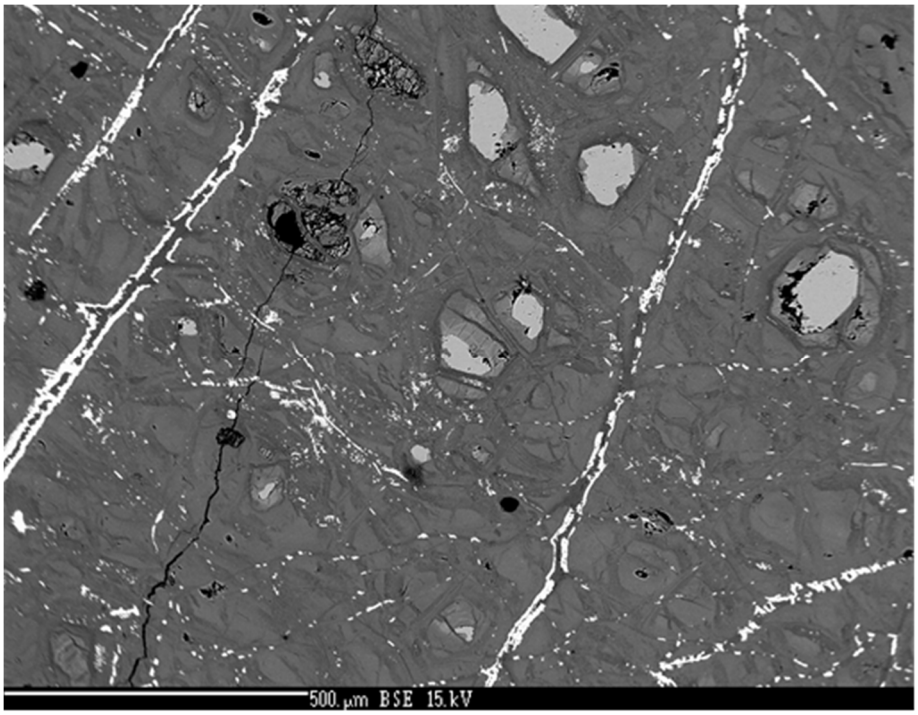

Figure 47. Backscattered electron image of serpentinization ongoing on a crystal of olivine from McL_313_329 obtained at the Brown University EMP Facility.

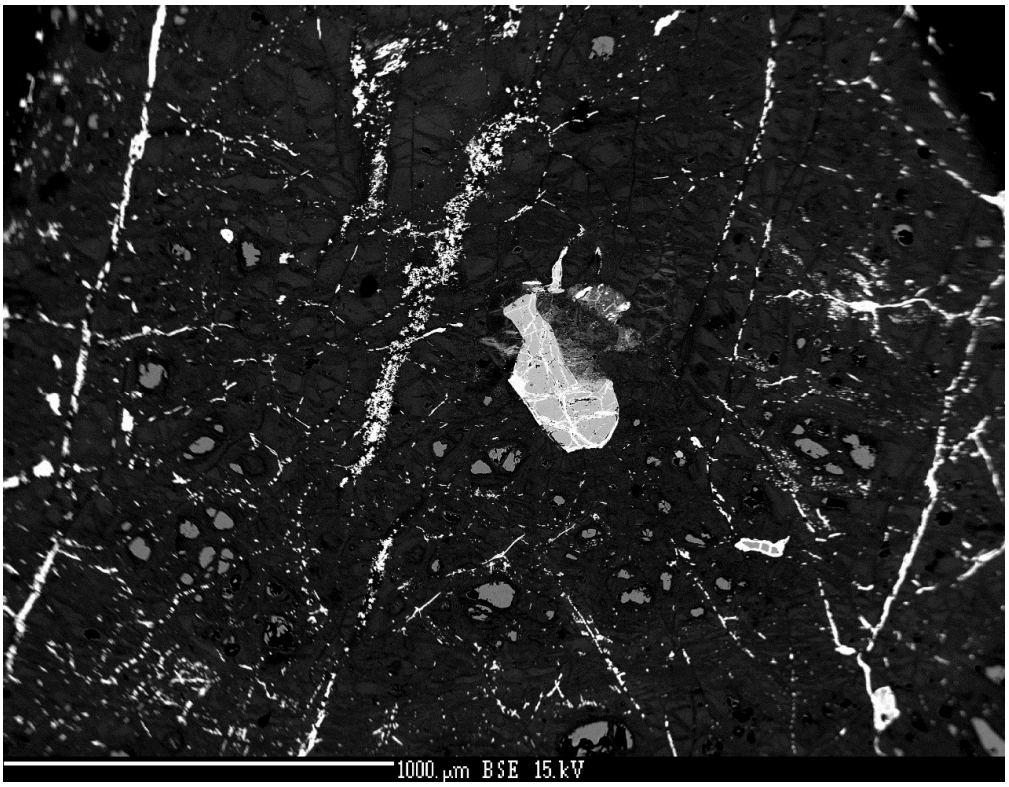

Figure 48. Backscattered electron image of serpentinized peridotite from McL_surface obtained at the Brown University EMP Facility.

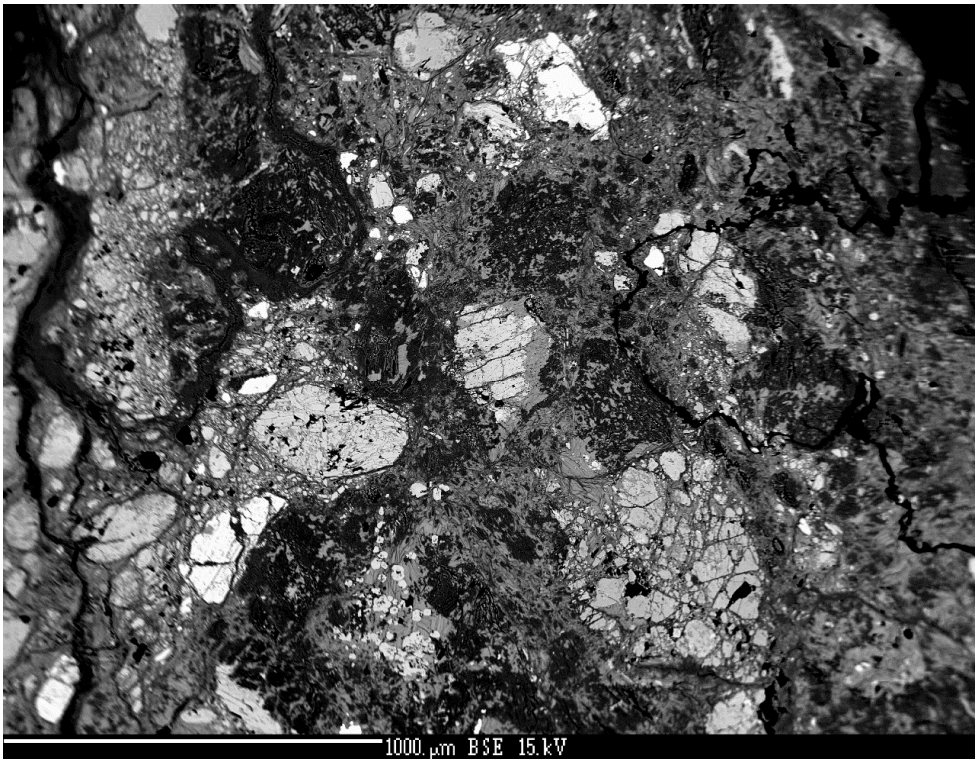

Figure 49. Backscattered electron image of serpentinized peridotite showing olivine and orthopyroxene from McL_356 obtained at the Brown University EMP Facility.

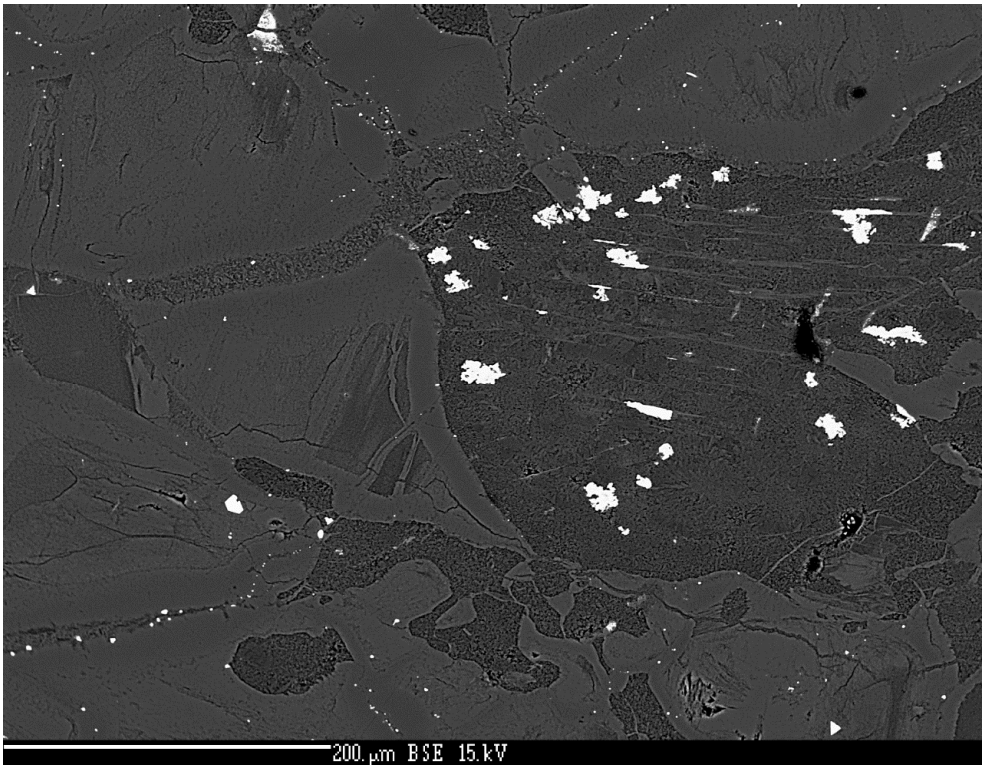

Figure 50. Backscattered electron image of serpentinized peridotite from McL_surface obtained at the Brown University EMP Facility.

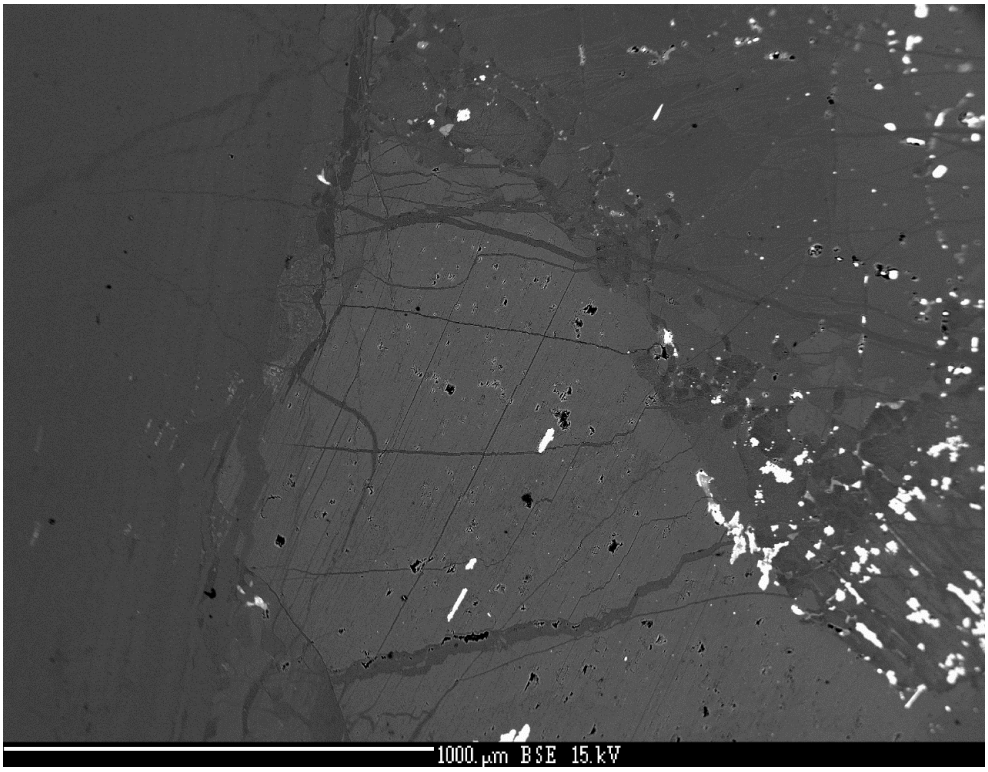

Figure 51. Backscattered electron image of serpentinized peridotite from McL_surface obtained at the Brown University EMP Facility.

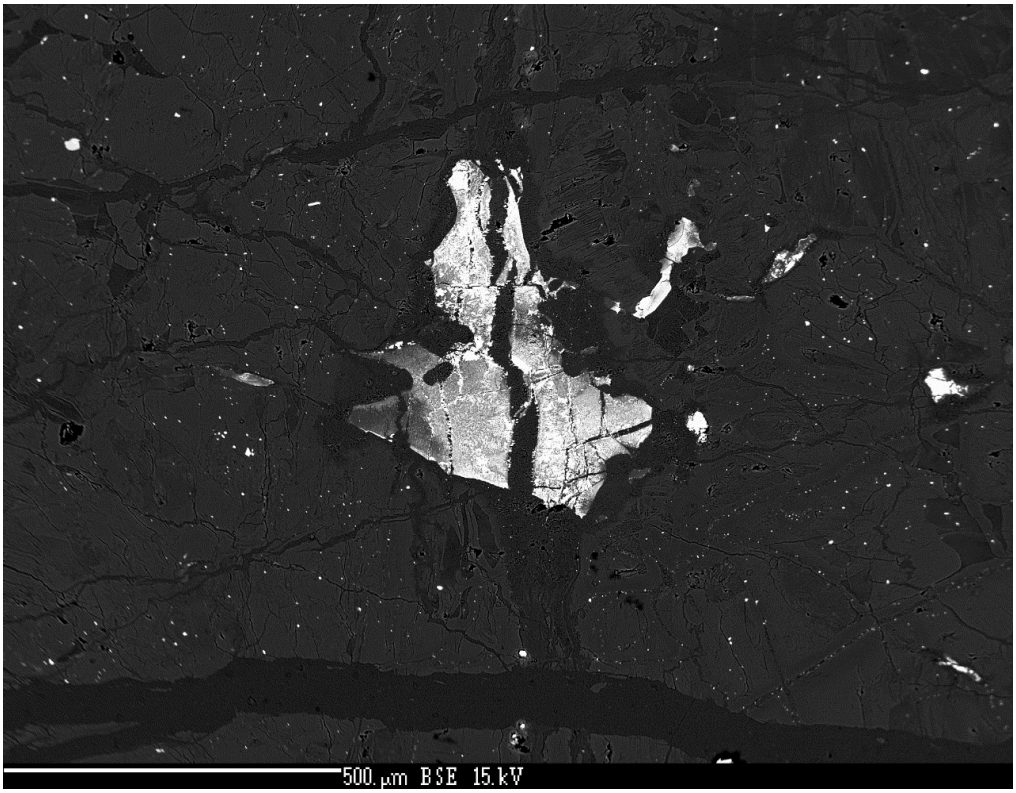

Figure 52. Backscattered electron image of serpentinized peridotite from McL_surface obtained at the Brown University EMP Facility.

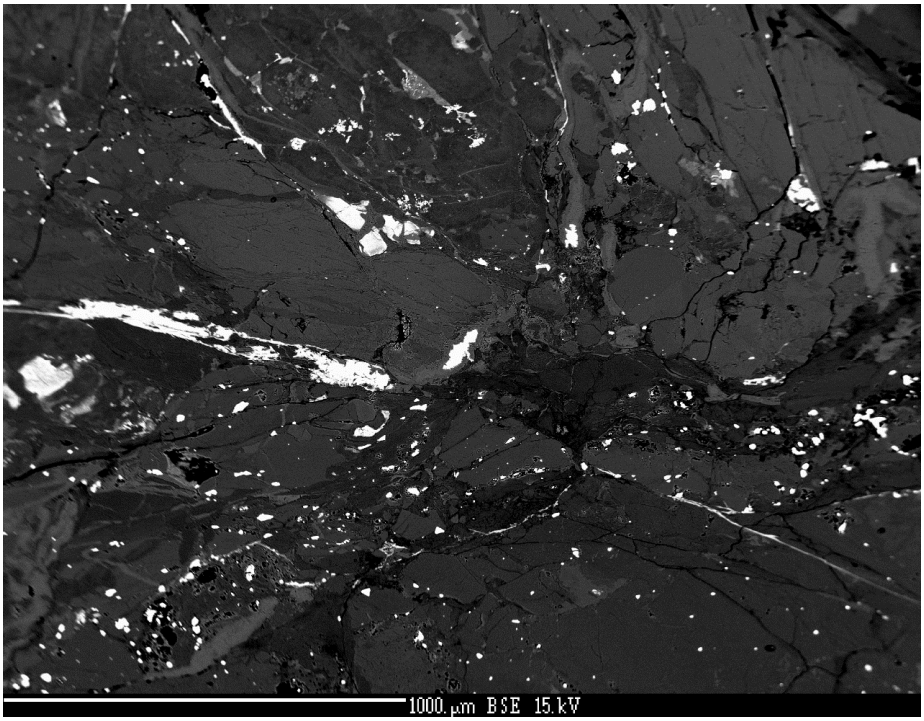

Figure 53. Backscattered electron image of serpentinized peridotite showing olivine and orthopyroxene from McL_356 obtained at the Brown University EMP Facility.

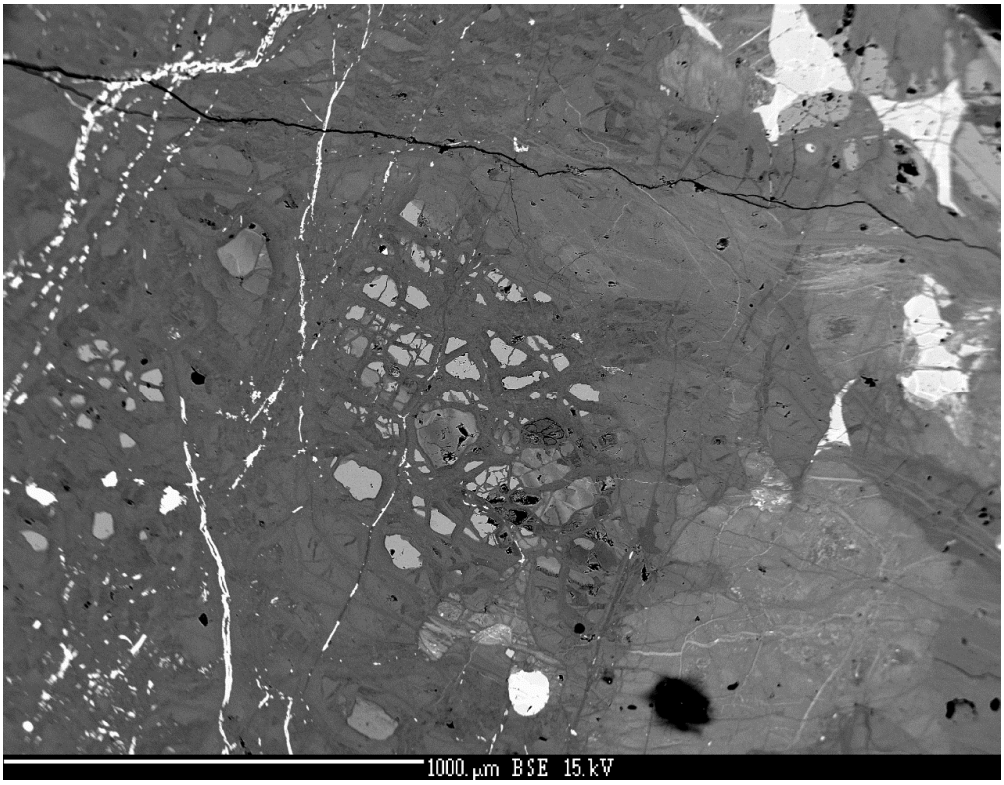

Figure 54. Backscattered electron image of serpentinization ongoing on a crystal of olivine from McL_313_329 obtained at the Brown University EMP Facility.

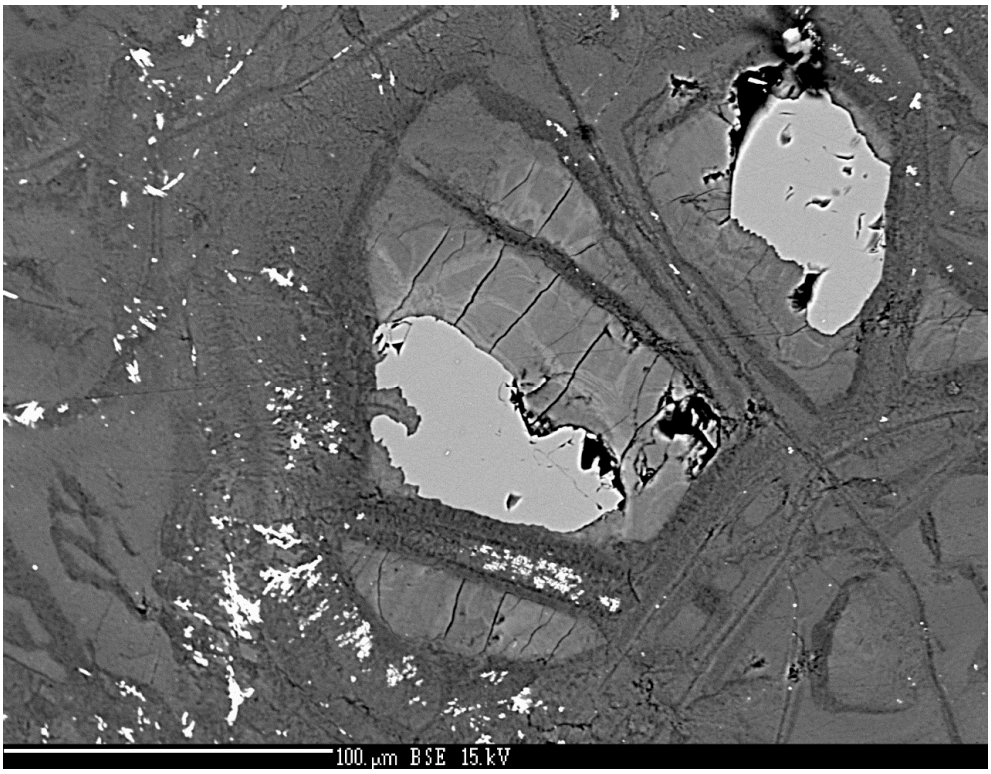

Figure 55. Backscattered electron image of serpentinization ongoing on a crystal of olivine from McL_313_329 obtained at the Brown University EMP Facility.

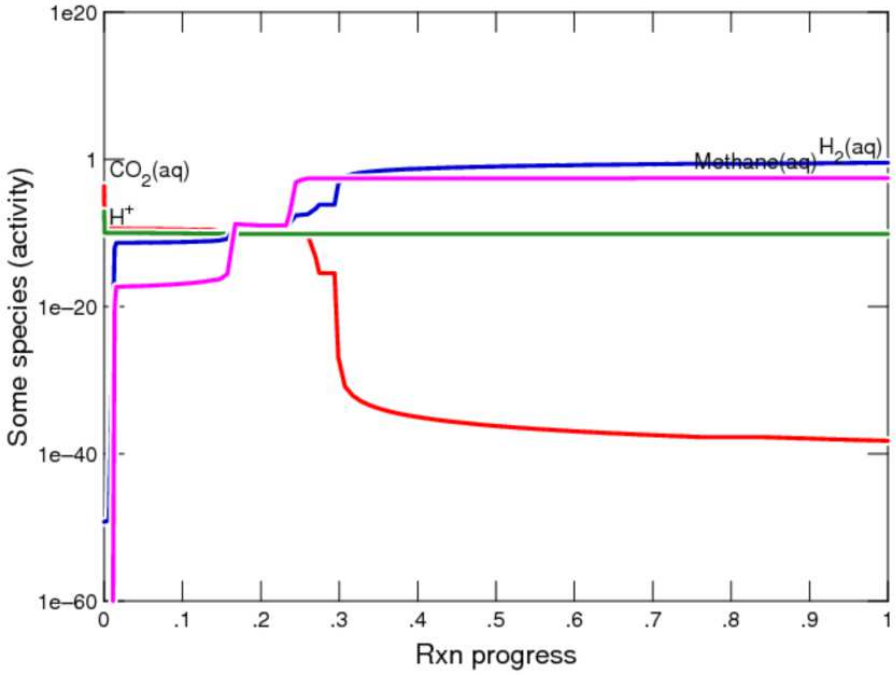

Figure 56. Representative results from Geochemist's Workbench REACT modeling of model CRO with planetary Na-Cl seawater at 273 showing major astrobiological aqueous species.

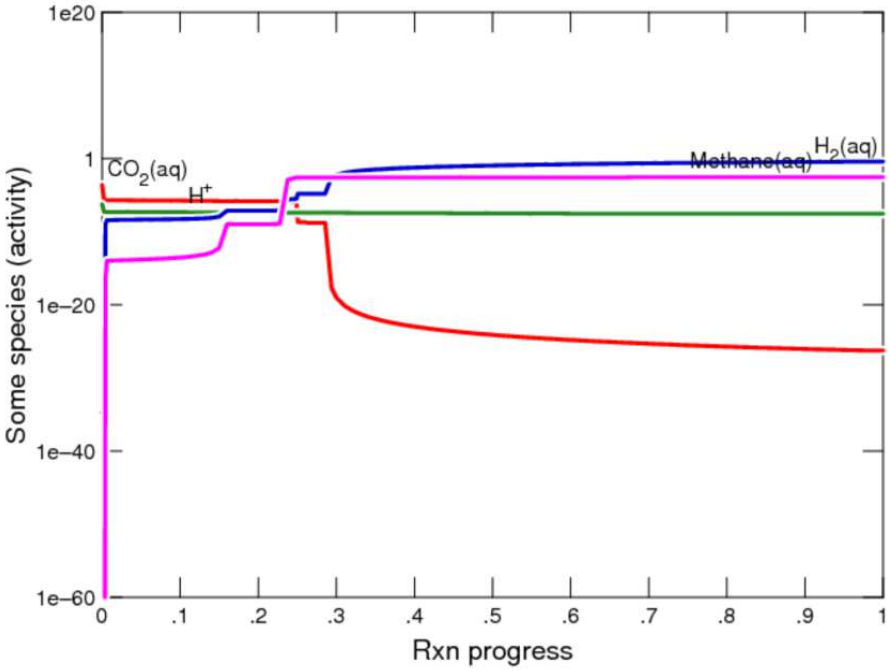

Figure 57. Representative results from Geochemist's Workbench REACT modeling of model CRO with planetary Na-Cl seawater at 373, showing major astrobiological aqueous species.

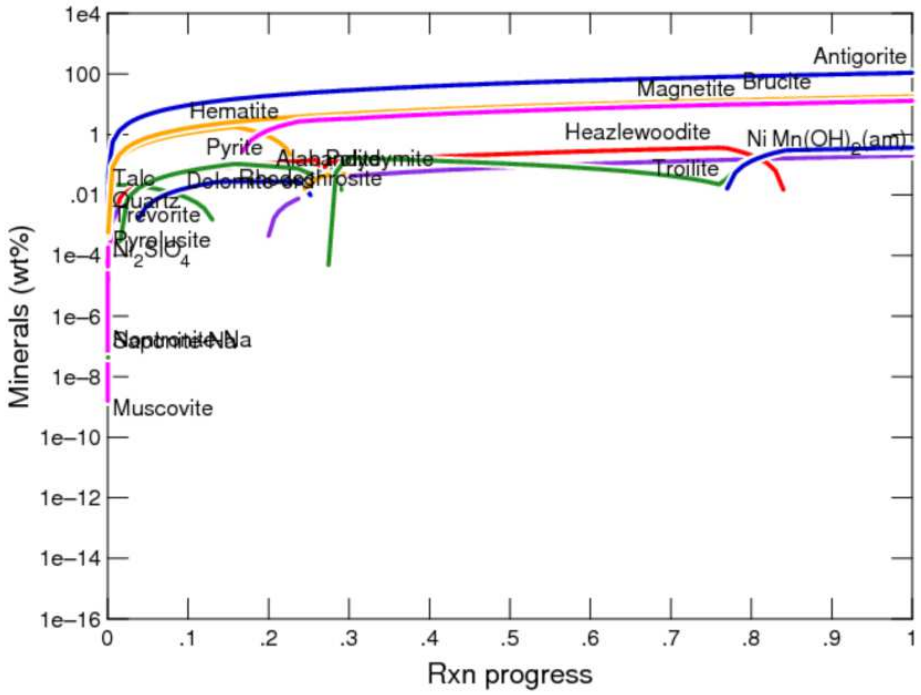

Figure 58. Representative results from Geochemist's Workbench REACT modeling of model CRO with planetary Na-Cl seawater at 273, showing major mineralogical species.

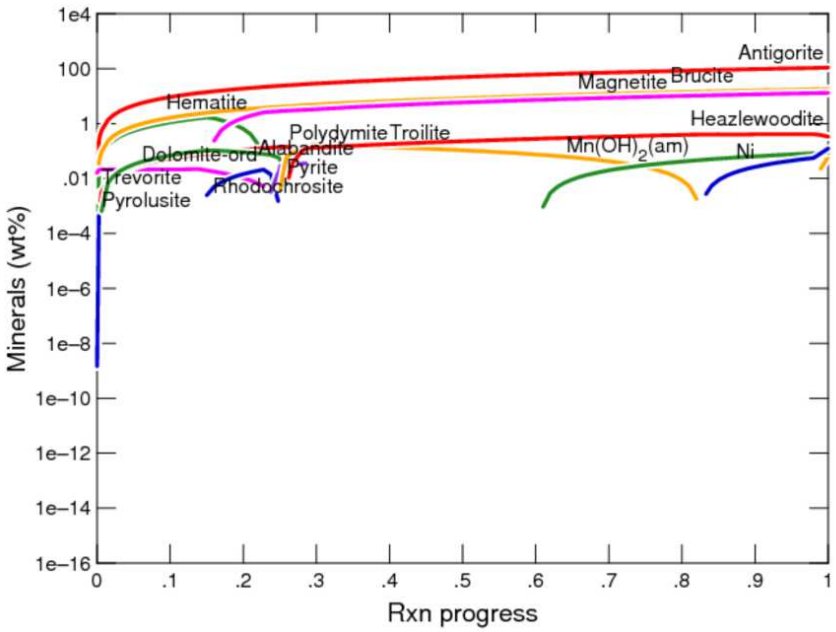

Figure 59. Representative results from Geochemist's Workbench REACT modeling of model CRO with planetary Na-Cl seawater at 373, showing major mineralogical species.

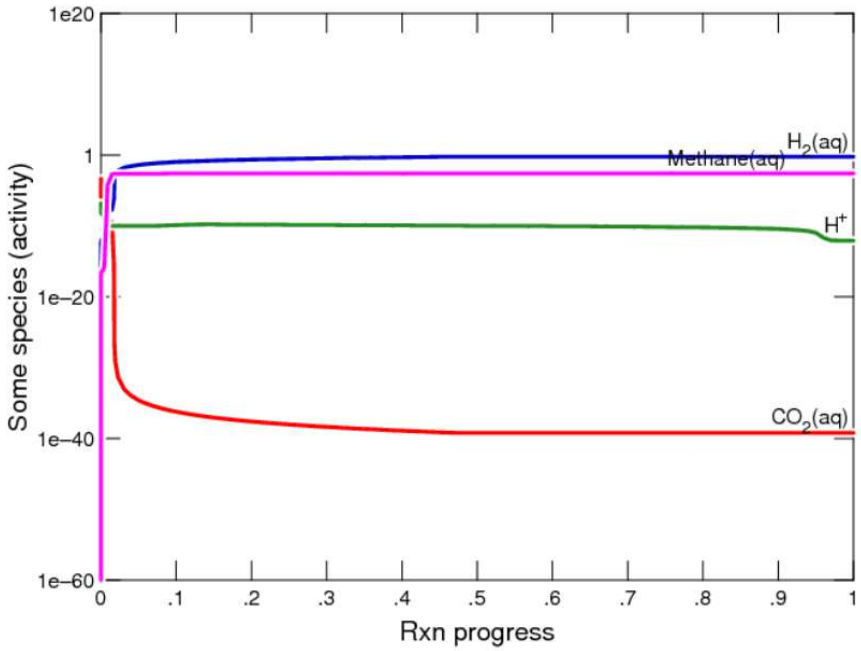

Figure 60. Representative results from Geochemist's Workbench REACT modeling of model lherzolitic shergottites with planetary Na-Cl seawater at 273, showing major astrobiological aqueous species.

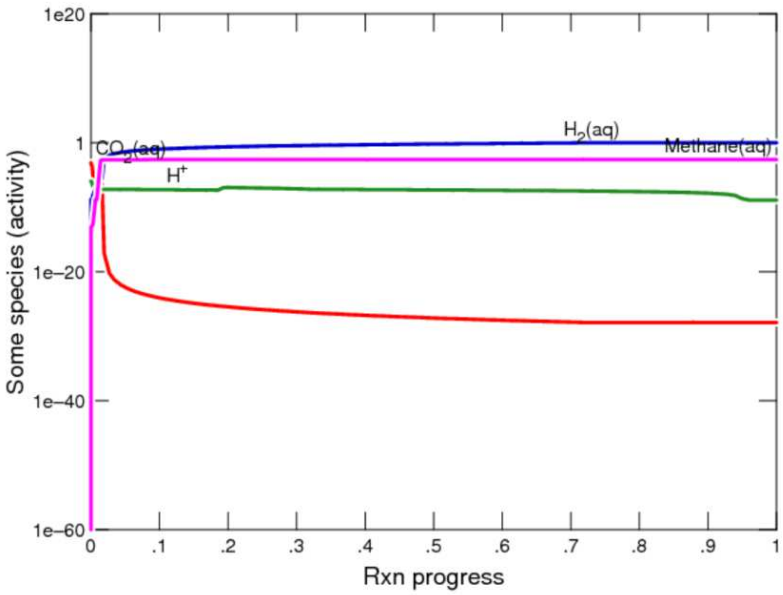

Figure 61. Representative results from Geochemist's Workbench REACT modeling of model lherzolitic shergottites with planetary Na-Cl seawater at 373, showing major astrobiological aqueous species.

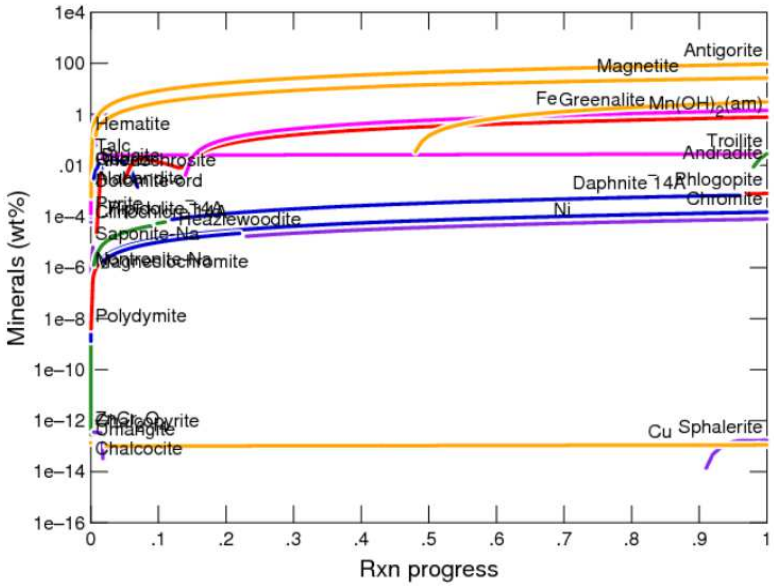

Figure 62. Representative results from Geochemist's Workbench REACT modeling of model lherzolitic shergottites with planetary Na-Cl seawater at 273, showing major mineralogical species.

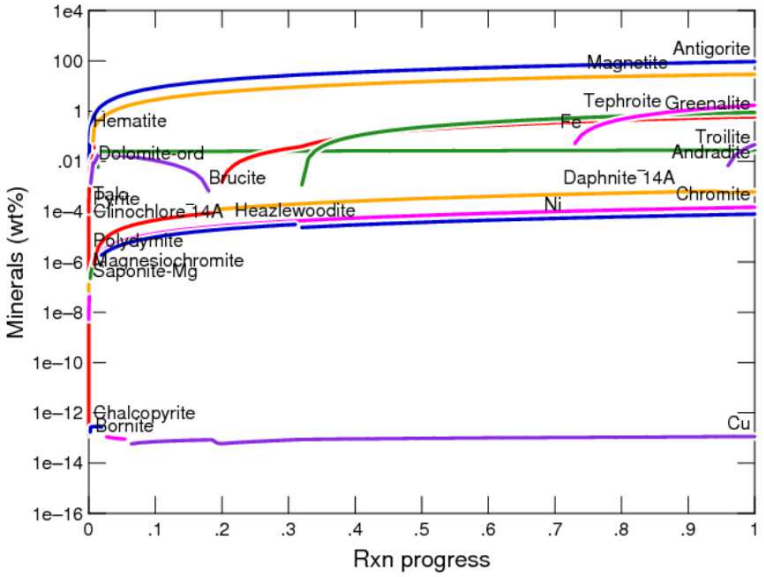

Figure 63. Representative results from Geochemist's Workbench REACT modeling of model lherzolitic shergottites with planetary Na-Cl seawater at 373, showing major mineralogical species.

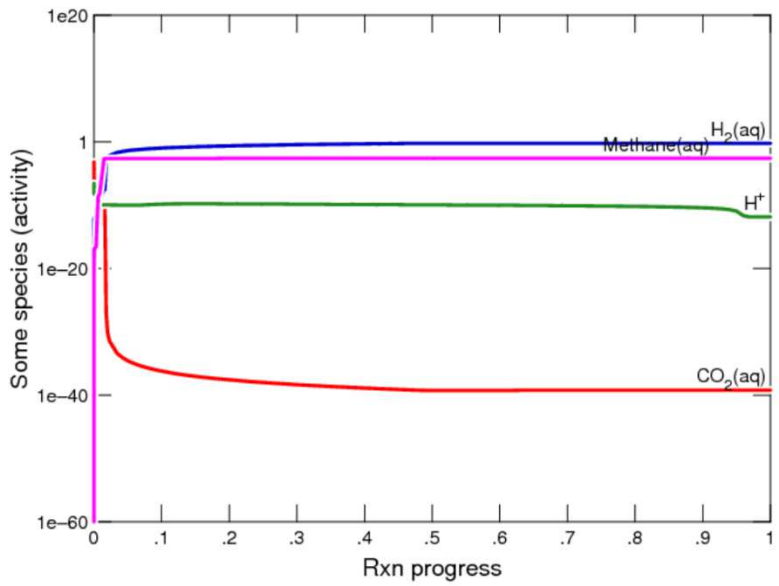

Figure 64. Representative results from Geochemist's Workbench REACT modeling of model lherzolitic shergottites with planetary Ca-Cl seawater at 273, showing major astrobiological aqueous species.

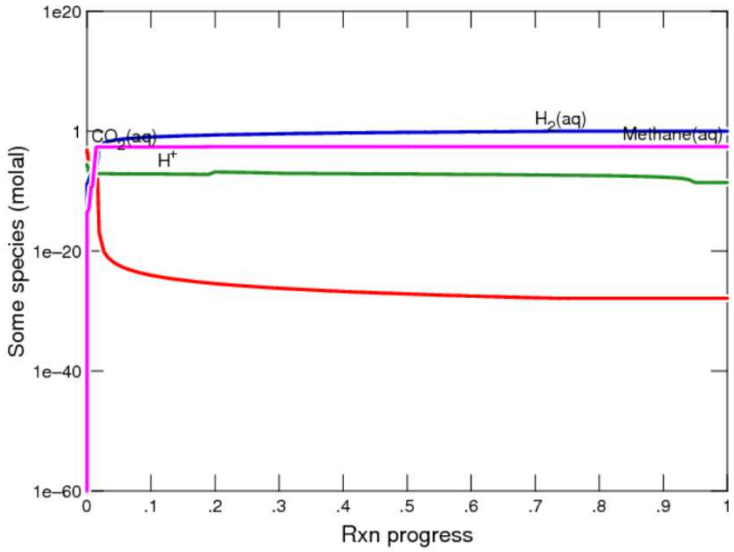

Figure 65. Representative results from Geochemist's Workbench REACT modeling of model lherzolitic shergottites with planetary Ca-Cl seawater at 373, showing major astrobiological aqueous species.

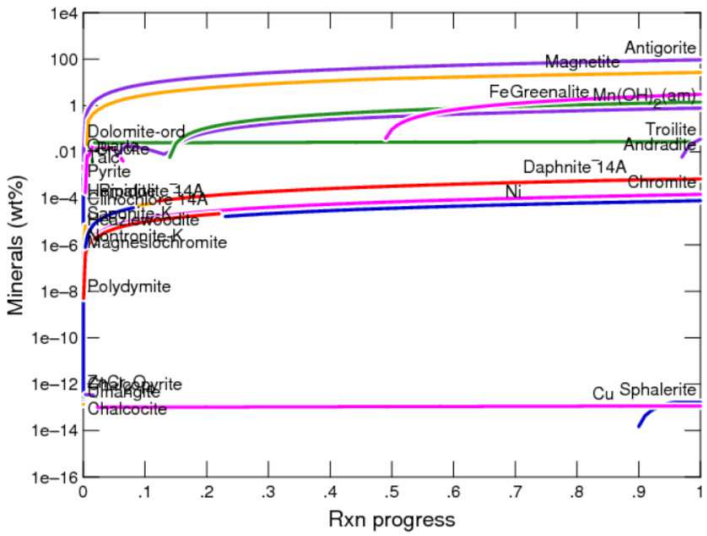

Figure 66. Representative results from Geochemist's Workbench REACT modeling of model lherzolitic shergottites with planetary Ca-Cl seawater at 273, showing major mineralogical species.

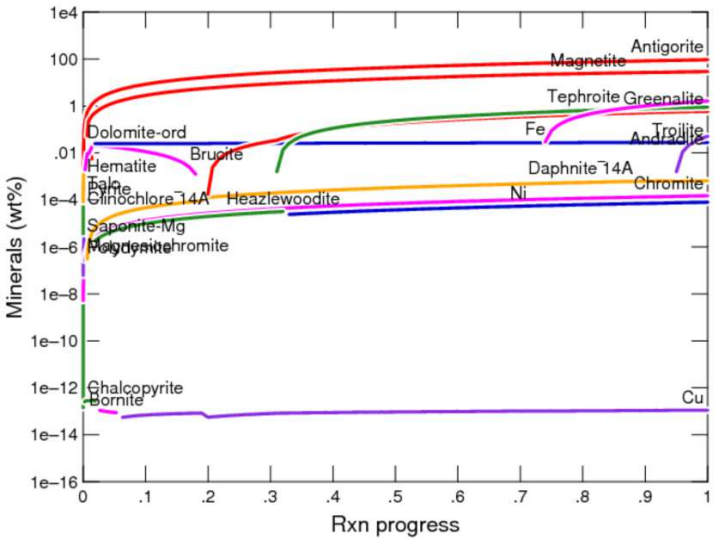

Figure 67. Representative results from Geochemist's Workbench REACT modeling of model lherzolitic shergottites with planetary Ca-Cl seawater at 373, showing major mineralogical species.

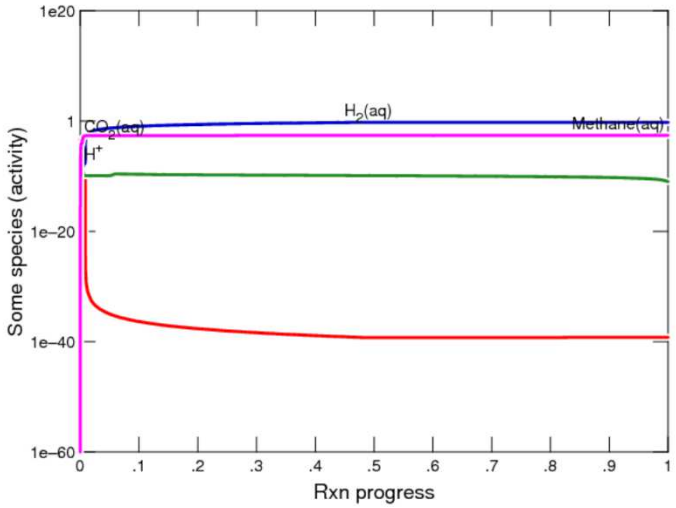

Figure 68. Representative results from Geochemist's Workbench REACT modeling of model lherzolitic shergottites with planetary Mg-Cl seawater at 273, showing major astrobiological aqueous species.

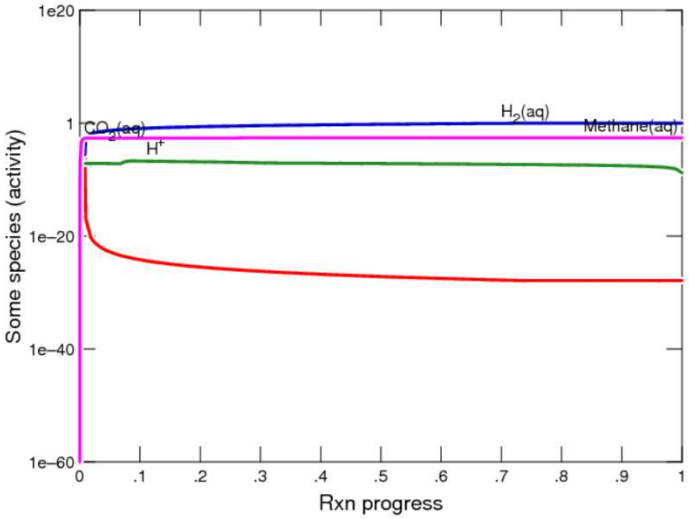

Figure 69. Representative results from Geochemist's Workbench REACT modeling of model lherzolitic shergottites with planetary Mg-Cl seawater at 373, showing major astrobiological aqueous species.

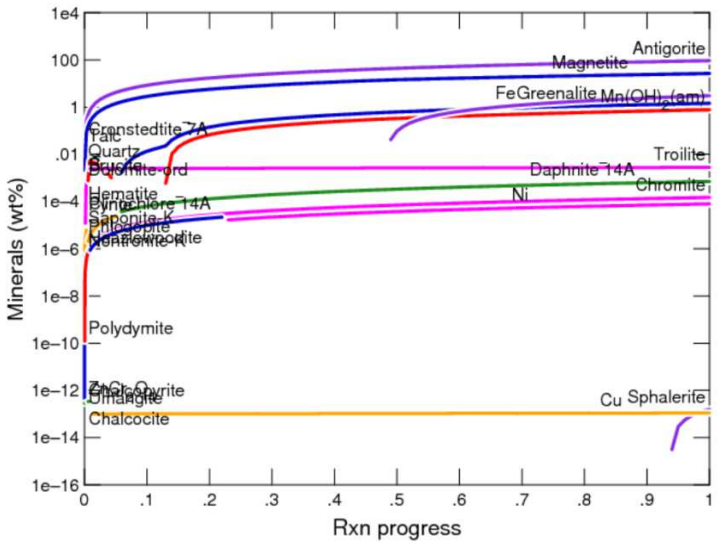

Figure 70. Representative results from Geochemist's Workbench REACT modeling of model lherzolitic shergottites with planetary Mg-Cl seawater at 273, showing major mineralogical species.

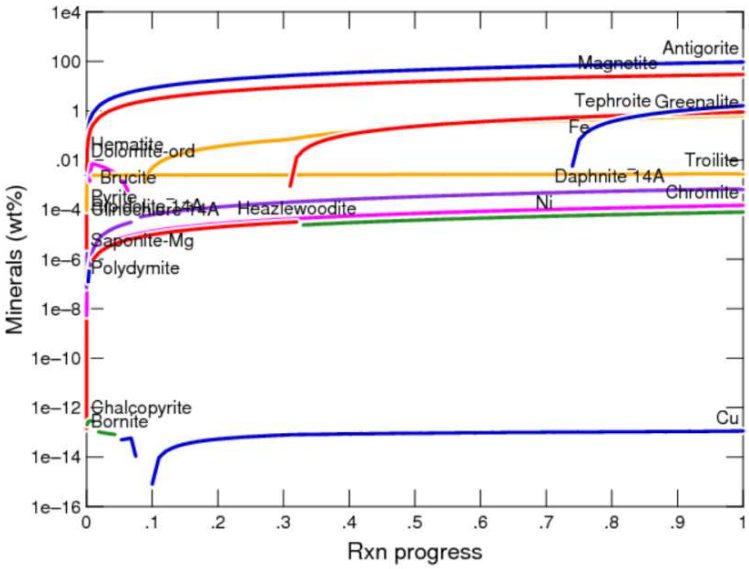

Figure 71. Representative results from Geochemist's Workbench REACT modeling of model lherzolitic shergottites with planetary Mg-Cl seawater at 373, showing major mineralogical species.

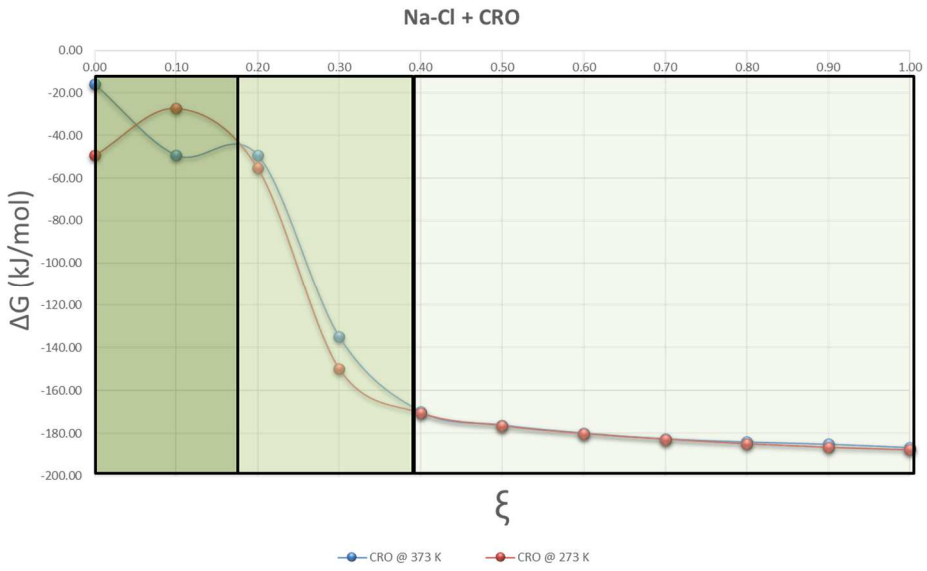

Figure 72. Bioenergetic modeling (as in Amend and Shock, 2001; Cardace et al., 2015), calculated from outputs results from Geochemist's Workbench REACT modeling of CRO and Na-Cl seawater systems using the Gibbs Free Energy equation for the methanogenesis (MG) reaction, $CO_{2(aq)} + 4H_{2(aq)} = CH4_{(aq)} + 2H_2O_{(l)}$.

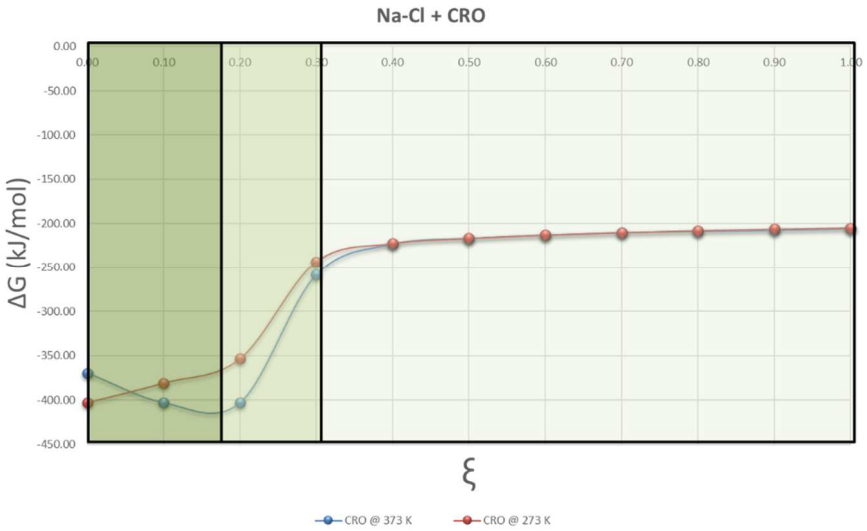

Figure 73. Bioenergetic modeling (as in Amend and Shock, 2001; Cardace et al., 2015), calculated from outputs results from Geochemist's Workbench REACT modeling of CRO and Na-Cl seawater systems using the Gibbs Free Energy equation for the methanotrophy (MT) reaction, $CH_{4(aq)} + 2H_2O_{(l)} = CO_{2(aq)} + 4H_{2(aq)}$.

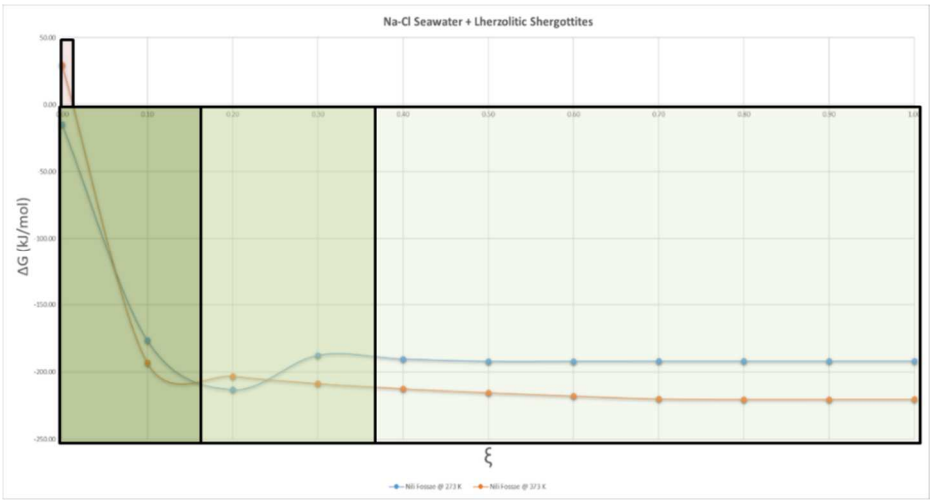

Figure 74. Generalized bioenergetic modeling at 273 K and 373 K (as in Amend and Shock, 2001; Cardace et al., 2015), calculated from outputs results from Geochemist's Workbench REACT modeling of Martian lherzolite shergottite and Na-Cl seawater systems using the Gibbs Free Energy equation of the methanogenesis (MG) reaction, $CO_{2(aq)} + 4H_{2(aq)} = CH4_{(aq)} + 2H_2O_{(l)}$.

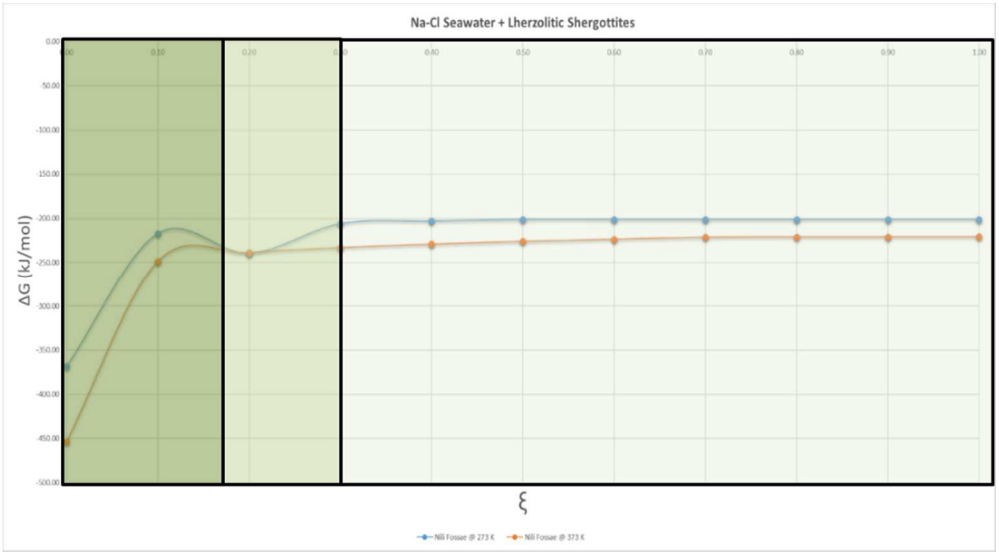

Figure 75. Bioenergetic modeling at 273 K and 373 K (as in Amend and Shock, 2001; Cardace et al., 2015), calculated from outputs results from Geochemist's Workbench REACT modeling of Martian lherzolite shergottite and Na-Cl seawater systems using the Gibbs Free Energy equation of the methanotrophy (MT) reaction, $CH_{4(aq)} + 2H_2O_{(l)} = CO_{2(aq)} + 4H_{2(aq)}$.

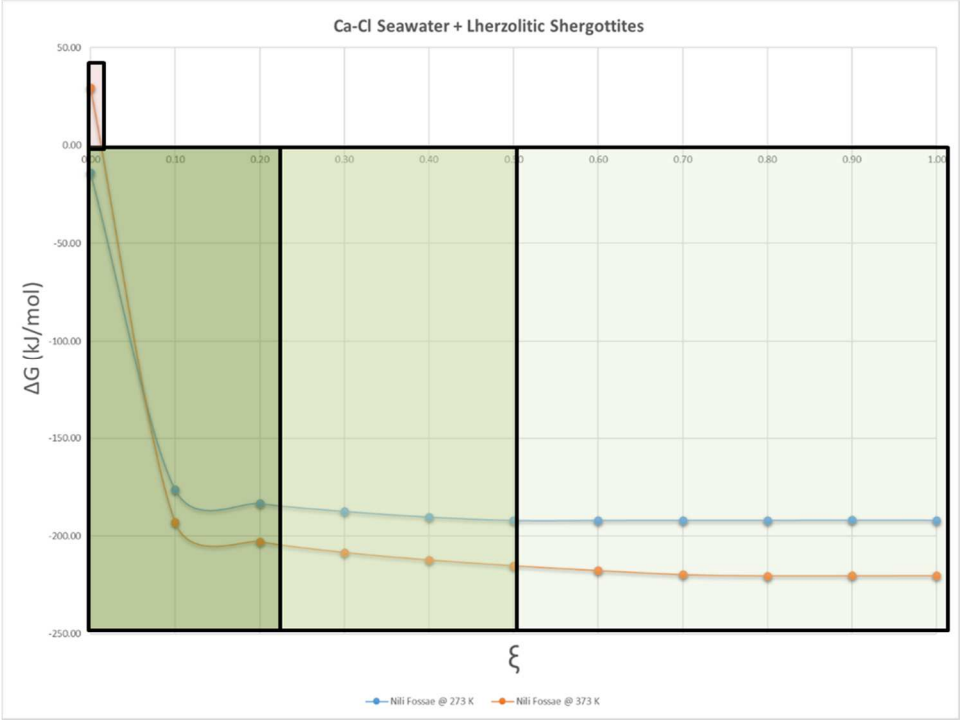

Figure 76. Generalized bioenergetic modeling at 273 K and 373 K (as in Amend and Shock, 2001; Cardace et al., 2015), calculated from outputs results from Geochemist's Workbench REACT modeling of Martian lherzolite shergottite and Ca-Cl seawater systems using the Gibbs Free Energy equation of the methanogenesis (MG) reaction, $CO_{2(aq)} + 4H_{2(aq)} = CH4_{(aq)} + 2H_2O_{(l)}$.

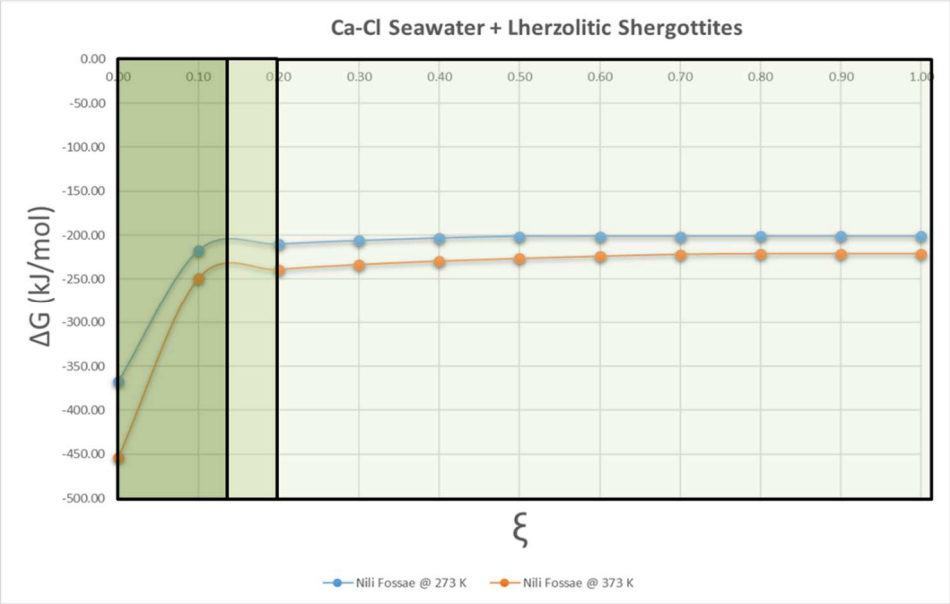

Figure 77. Bioenergetic modeling at 273 K and 373 K (as in Amend and Shock, 2001; Cardace et al., 2015), calculated from outputs results from Geochemist's Workbench REACT modeling of Martian lherzolite shergottite and Ca-Cl seawater systems using the Gibbs Free Energy equation of the methanotrophy (MT) reaction, $CH_{4(aq)} + 2H_2O_{(l)} = CO_{2(aq)} + 4H_{2(aq)}$.

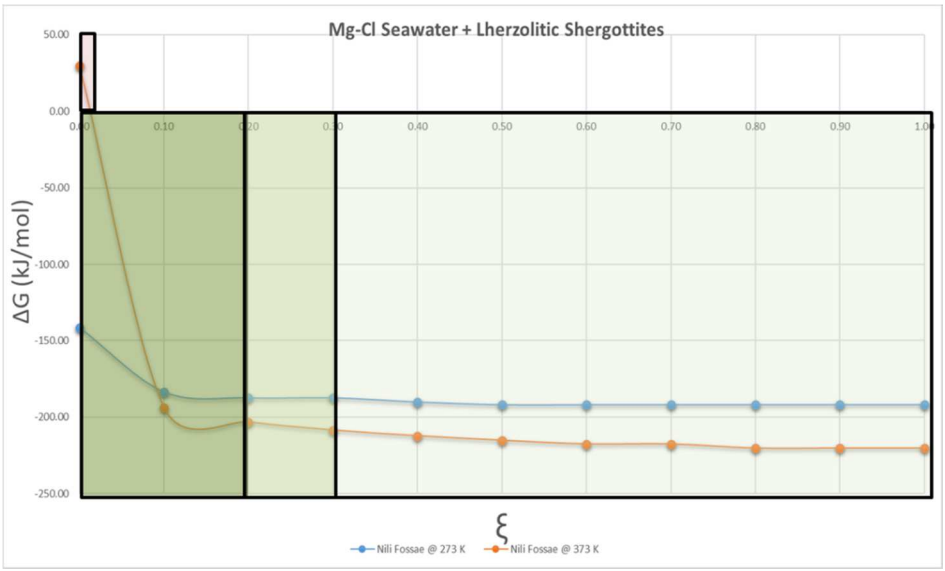

Figure 78. Bioenergetic modeling at 273 K (as in Amend and Shock, 2001; Cardace et al., 2015), calculated from outputs results from Geochemist's Workbench REACT modeling of Martian lherzolite shergottite and Mg-Cl seawater systems using the Gibbs Free Energy equation of the methanogenesis (MG) reaction, $CO_{2(aq)} + 4H_{2(aq)} = CH4_{(aq)} + 2H_2O_{(l)}$.

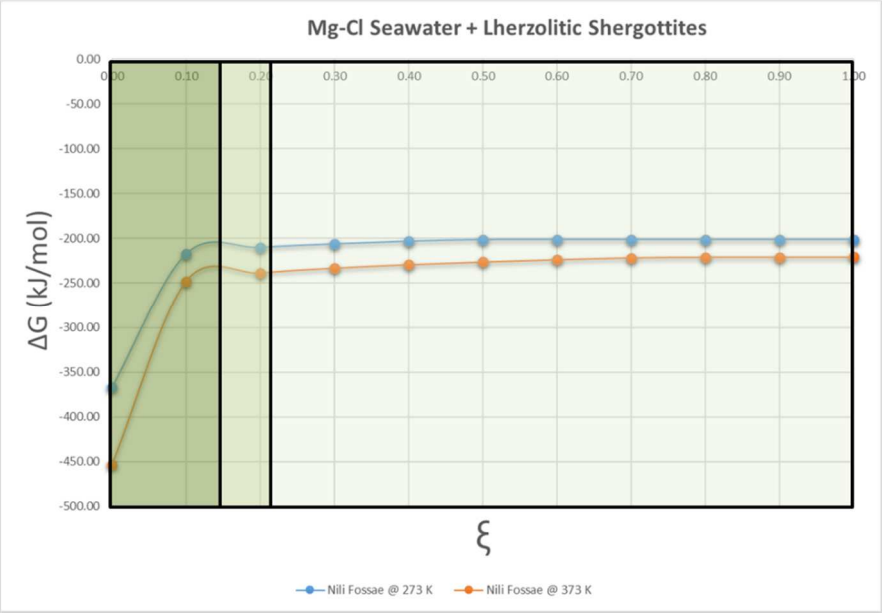

Figure 79. Bioenergetic modeling at 273 K and 373 K (as in Amend and Shock, 2001; Cardace et al., 2015), calculated from outputs results from Geochemist's Workbench REACT modeling of Martian lherzolite shergottite and Mg-Cl seawater systems using the Gibbs Free Energy equation of the methanotrophy (MT) reaction, $CH_{4(aq)} + 2H_2O_{(l)} = CO_{2(aq)} + 4H_{2(aq)}$.

REFERENCES

Abramov, O., & Kring, D. A. (2005). Impact□induced hydrothermal activity on early mars. *Journal of Geophysical Research: Planets, 110*(E12)

Akai, J. (1988). Incompletely transformed serpentine-type phyllosilicates in the matrix of antarctic CM chondrites. *Geochimica Et Cosmochimica Acta, 52*(6), 1593-1599.

Allen, D. E., & Seyfried, W. (2003). Compositional controls on vent fluids from ultramafic-hosted hydrothermal systems at mid-ocean ridges: An experimental study at 400 C, 500 bars. *Geochimica Et Cosmochimica Acta, 67*(8), 1531-1542.

Allen, D. E., & Seyfried, W. (2004). Serpentinization and heat generation: Constraints from lost city and rainbow hydrothermal systems. *Geochimica Et Cosmochimica Acta, 68*(6), 1347- 1354.

Bach, W., Garrido, C. J., Paulick, H., Harvey, J., & Rosner, M. (2004). Seawater□peridotite interactions: First insights from ODP Leg 209, MAR 15° N. *Geochemistry, Geophysics, Geosystems*, 5(9).

Bach, W., Paulick, H., Garrido, C. J., Ildefonse, B., Meurer, W. P., & Humphris, S. E. (2006).Unraveling the sequence of serpentinization reactions: Petrography, mineral chemistry, and petrophysics of serpentinites from MAR 15 N (ODP leg 209, site 1274). *Geophysical Research Letters, 33*(13)

Bailey, E., & Blake, M. (1974). Major chemical characteristics of mesozoic coast range ophiolite in california. *Journal of Research of the United States Geological Survey, 2*, 637-656.

Balaram, V., Ramesh, S., & Anjaiah, K. (1996). New trace element and ree data in thirteen gsf reference samples by icp□ms. *Geostandards Newsletter, 20*(1), 71-78.

Barge, L., Branscomb, E., Brucato, J., Cardoso, S., Cartwright, J., Danielache, S., . . . Mojzsis, S. (2016). Thermodynamics, disequilibrium, evolution: Far-from-equilibrium geological and chemical considerations for origin-of-life research. *Origins of Life and Evolution of Biospheres,* , 1-18.

Berndt, M. E., Allen, D. E., & Seyfried, W. E. (1996). Reduction of CO2 during serpentinization of olivine at 300 C and 500 bar. *Geology, 24*(4), 351-354.

Blake, D., Vaniman, D., Achilles, C., Anderson, R., Bish, D., Bristow, T., ... & Downs, R. T. (2012). Characterization and calibration of the CheMin mineralogical instrument on Mars Science Laboratory. Space Science Reviews, 170(1-4), 341-399.

Bonatti, E., Lawrence, J. R., & Morandi, N. (1984). Serpentinization of oceanic peridotites: Temperature dependence of mineralogy and boron content. *Earth and Planetary Science Letters, 70*(1), 88-94.

Borucki, W. J., Agol, E., Fressin, F., Kaltenegger, L., Rowe, J., Isaacson, H., . . . Winn, J. N. (2013). Kepler-62: A five-planet system with planets of 1.4 and 1.6 earth radii in the habitable zone. *Science (New York, N.Y.), 340*(6132), 587-590. doi:10.1126/science.1234702 [doi]

Boye Nissen, S., Taubner, R., Leitner, J. J., & Firneis, M. G. (2015). The possibility of serpentinization on enceladus. Paper presented at the *EGU General Assembly Conference Abstracts, , 17* 13114.

Brugger, J., Wülser, P., & Foden, J. (2011). Genesis and preservation of a uranium-rich paleozoic epithermal system with a surface expression (northern flinders ranges, south australia):Radiogenic heat driving regional hydrothermal circulation over geological timescales. *Astrobiology, 11*(6), 499-508.

Campins, H., & Ryan, E. V. (1989). The identification of crystalline olivine in cometary silicates. *The Astrophysical Journal, 341*, 1059-1066.

Cannat, M., Bideau, D., & Bougault, H. (1992). Serpentinized peridotites and gabbros in the mid- atlantic ridge axial valley at 15 37′ N and 16 52′ N. *Earth and Planetary* **`Science`** *Letters, 109*(1), 87-106.

Cardace, D., Carnevale, D., Schrenk, M. O., Twing, K. I., McCollom, T. M., & Hoehler, T. M. (2012). Mineral controls on microbial niche space in subsurface serpentinites of the coast range ophiolite, northern california. Paper presented at the *AGU Fall Meeting Abstracts, , 1* 0511.

Cardace, D., Hoehler, T., McCollom, T., Schrenk, M., Carnevale, D., Kubo, M., & Twing, K. (2013). Establishment of the coast range ophiolite microbial observatory (CROMO): Drilling objectives and preliminary outcomes.

Cardace, D., Hoehler, T., McCollom, T., Schrenk, M., & Kubo, M. (2014). Integration of 3 consecutive years of aqueous geochemistry monitoring

serpentinization at the coast range ophiolite microbial observatory (CROMO), northern califorhnia, USA. Paper presented at the *AGU Fall Meeting Abstracts, , 1* 4835.

Carnevale, D., Cardace, D., Mccann, A., & Hoehler, T. (2011). Mineralogy and geochemistry of coast range ophiolite, CA rock cores keys to understanding subsurface serpentinite habitability on mars. Paper presented at the *AGU Fall Meeting Abstracts, , 1* 0401.

Carnevale, D., Cardace, D., Mccann, A., & Hoehler, T. (2011). Mineralogy and geochemistry of coast range ophiolite, CA rock cores keys to understanding subsurface serpentinite habitability on mars. Paper presented at the *AGU Fall Meeting Abstracts, , 1* 0401.

Chambers, J. (2010). Terrestrial planet formation. *Exoplanets, 1*, 297-317.

Chambers, J. E. (2004). Planetary accretion in the inner solar system. *Earth and Planetary Science Letters, 223*(3), 241-252.

Chapman, R. H. (1975). *Geophysical Study of the Clear Lake Region, California,*

Charlou, J. L., Fouquet, Y., Bougault, H., Donval, J. P., Etoubleau, J., Jean-Baptiste, P., . . . Rona, P. A. (1998). Intense CH 4 plumes generated by serpentinization of ultramafic rocks at the intersection of the 15 20′ N fracture zone and the mid-atlantic ridge. *Geochimica Et Cosmochimica Acta, 62*(13), 2323-2333.

Choi, S. H., Shervais, J. W., & Mukasa, S. B. (2008). Supra-subduction and abyssal mantle peridotites of the coast range ophiolite, california. *Contributions to Mineralogy and Petrology, 156*(5), 551-576.

Cruikshank, D. P., & Hartmann, W. K. (1984). The meteorite-asteroid connection: Two olivine-rich asteroids. *Science, 223*, 281-284.

De Pater, I., & Lissauer, J. J. (2015). Planetary sciences. Cambridge University Press.

Deschamps, F., Guillot, S., Godard, M., Chauvel, C., Andreani, M., & Hattori, K. (2010). In situ characterization of serpentinites from forearc mantle wedges: Timing of serpentinization and behavior of fluid-mobile elements in subduction zones. *Chemical Geology, 269*(3), 262- 277.

Dilek, Y., & Furnes, H. (2011). Ophiolite genesis and global tectonics: Geochemical and tectonic fingerprinting of ancient oceanic lithosphere. *GSA Bulletin,* 123(3-4), 387-411.

Dilek, Y., Furnes, H., & Shallo, M. (2007). Suprasubduction zone ophiolite formation along the periphery of mesozoic gondwana. *Gondwana Research, 11*(4), 453-475.

Dilek, Y., & Polat, A. (2008). Suprasubduction zone ophiolites and archean tectonics. *Geology, 36*(5), 431-432.

Donnelly, J., McLaughlin, R., Goff, F., & Hearn Jr, B. (1976). Active faulting in the geysers-clear lake area, northern california: Geol. *Soc.America Abs.with Programs, 8*(3), 369-370.

Dorn, C., Khan, A., Heng, K., Connolly, J. A., Alibert, Y., Benz, W., & Tackley, P. (2015). Can we constrain the interior structure of rocky exoplanets from mass and radius measurements? *Astronomy & Astrophysics, 577*, A83.

Ehlmann, B. L., Mustard, J. F., Murchie, S. L., Bibring, J., Meunier, A., Fraeman, A. A., & Langevin, Y. (2011). Subsurface water and clay mineral formation during the early history of mars. *Nature, 479*(7371), 53-60.

Ehlmann, B., Anderson, F., Andrews□Hanna, J., Catling, D., Christensen, P., Cohen, B., . . . Farley,(2016). The sustainability of habitability on terrestrial planets: Insights, questions, and needed measurements from mars for understanding the evolution of Earth□like worlds. *Journal of Geophysical Research: Planets,*

Ehlmann, B., Mustard, J., & Murchie, S. (2010). Geologic setting of serpentine deposits on mars. *Geophysical Research Letters, 37*(6)

Elkins-Tanton, L. T., Draper, D. S., Agee, C. B., Jewell, J., Thorpe, A., & Hess, P. (2007). The last lavas erupted during the main phase of the siberian flood volcanic province: Results from experimental petrology. *Contributions to Mineralogy and Petrology, 153*(2), 191-209.

Fairen, A. G., Chevrier, V., Abramov, O., Marzo, G. A., Gavin, P., Davila, A. F., . . . McKay, C. P. (2010). Noachian and more recent phyllosilicates in impact craters on mars. *Proceedings of the National Academy of Sciences of the United States of America, 107*(27), 12095-12100. doi:10.1073/pnas.1002889107 [doi]

Fassett, C. I., & Head, J. W. (2008). Valley network-fed, open-basin lakes on mars: Distribution and implications for noachian surface and subsurface hydrology. *Icarus, 198*(1), 37-56.

Fassett, C. I., & Head, J. W. (2008). Valley network-fed, open-basin lakes on mars: Distribution and implications for noachian surface and subsurface hydrology. *Icarus, 198*(1), 37-56.

Foing, B., Stoker, C., & Ehrenfreund, P. (2011). Astrobiology field research in Moon/Mars analogue environments. *International Journal of Astrobiology, 10*(03), 137-139.

Foustoukos, D. I., Savov, I. P., & Janecky, D. R. (2008). Chemical and isotopic constraints on water/rock interactions at the lost city hydrothermal field, 30 N mid-atlantic ridge. *Geochimica Et Cosmochimica Acta, 72*(22), 5457-5474.

Fruh-Green, G. L., Kelley, D. S., Bernasconi, S. M., Karson, J. A., Ludwig, K. A., Butterfield, D. A., . . . Proskurowski, G. (2003). 30,000 years of hydrothermal activity at the lost city vent field. *Science (New York, N.Y.), 301*(5632), 495-498. doi:10.1126/science.1085582 [doi]

Glein, C. R. (2015). Noble gases, nitrogen, and methane from the deep interior to the atmosphere of titan. *Icarus, 250*, 570-586.

Glein, C. R., Baross, J. A., & Waite, J. H. (2015). The pH of enceladus' ocean. *Geochimica Et Cosmochimica Acta, 162*, 202-219.

Godard, M., Jousselin, D., & Bodinier, J. (2000). Relationships between geochemistry and structure beneath a palaeo-spreading centre: A study of the mantle section in the oman ophiolite. *Earth and Planetary Science Letters, 180*(1), 133-148.

Gonzalez-Cataldo, F., Davis, S., & Gutierrez, G. (2016). Melting curve of SiO2 at multimegabar pressures: Implications for gas giants and super-earths. *Scientific Reports, 6*, 26537. doi:10.1038/srep26537 [doi]

Goodman, J. C., & Lenferink, E. (2012). Numerical simulations of marine hydrothermal plumes for europa and other icy worlds. *Icarus, 221*(2), 970-983.

Greenberger, R. N., Mustard, J. F., Cloutis, E. A., Pratt, L. M., Sauer, P. E., Mann, P., . . . Bish, D. (2015). Serpentinization, iron oxidation, and aqueous conditions in an ophiolite: Implications for hydrogen production and habitability on mars. *Earth and Planetary Science Letters, 416*, 21-34.

Greenberger, R., Mustard, J., Cloutis, E., Pratt, L., Sauer, P., Mann, P., . . . Dyar, M. (2014). Aqueous conditions and habitability associated with formation of a serpentinite: Using analyses of ferric iron and stable carbon isotopes to reconstruct hydrogen production. Paper presented at the *AGU Fall Meeting Abstracts, , 1* 4040.

Haghighipour, N. (2013). The formation and dynamics of super-earth planets. *Annual Review of Earth and Planetary Sciences, 41*, 469-495.

Hansen, C., Shemansky, D. E., Esposito, L. W., Stewart, A., Lewis, B., Colwell, J., . . . Teolis, B. (2011). The composition and structure of the enceladus plume. *Geophysical Research Letters, 38*(11)

Hansen, C. J., Esposito, L., Stewart, A. I., Colwell, J., Hendrix, A., Pryor, W., . . . West, R. (2006). Enceladus' water vapor plume. *Science (New York, N.Y.), 311*(5766), 1422-1425. doi:311/5766/1422 [pii]

Hawkins, J. W., & Evans, C. A. (1983). Geology of the zambales range, luzon, philippine islands: Ophiolite derived from an island Arc□Back arc basin pair. *The Tectonic and Geologic Evolution of Southeast Asian Seas and Islands: Part 2,* , 95-123.

Hearn Jr, B. C., Donnelly, J. M., & Goff, F. E. (1976). *Preliminary Geologic Map and Cross- Section of the Clear Lake Volcanic Field, Lake County, California,*

Hellevang, H., Huang, S., & Thorseth, I. H. (2011). The potential for low-temperature abiotic hydrogen generation and a hydrogen-driven deep biosphere. *Astrobiology, 11*(7), 711-724.

Hicks, L. J., Bridges, J. C., & Gurman, S. (2014). Ferric saponite and serpentine in the nakhlite martian meteorites. *Geochimica Et Cosmochimica Acta, 136*, 194-210.

Holm, N. G., Oze, C., Mousis, O., Waite, J., & Guilbert-Lepoutre, A. (2015). **Serpentinization and the formation of H2 and CH4 on celestial bodies (planets, moons,** comets). *Astrobiology, 15*(7), 587-600.

Hopson, C. A., Mattinson, J. M., & Pessagno Jr, E. A. (1981). Coast range ophiolite, western california. *The Geotectonic Development of California, Rubey, 1*, 418-510.

Houghton, J., Seyfried Jr, W., Banta, A., & Reysenbach, A. (2007). Continuous enrichment culturing of thermophiles under sulfate and nitrate-reducing conditions and at deep-sea hydrostatic pressures. *Extremophiles, 11*(2), 371-382.

Hsu, H., Postberg, F., Sekine, Y., Shibuya, T., Kempf, S., Horányi, M., . . . Masaki, Y. (2015). Ongoing hydrothermal activities within enceladus. *Nature, 519*(7542), 207-210.

Iess, L., Stevenson, D. J., Parisi, M., Hemingway, D., Jacobson, R. A., Lunine, J. I., . . . Tortora, P. (2014). The gravity field and interior structure of enceladus. *Science (New York,N.Y.), 344*(6179), 78-80. doi:10.1126/science.1250551 [doi]

Ionov, D., Savoyant, L., & Dupuy, C. (1992). Application of the icp□ms technique to trace element analysis of peridotites and their minerals. *Geostandards Newsletter, 16*(2), 311-315.

Isherwood, W. F. (1976). Gravity and magnetic studies of the geysers-clear lake geothermal region, california, USA.

Jackson, B., Barnes, R., & Greenberg, R. (2008). Tidal heating of terrestrial extrasolar planets and implications for their habitability. *Monthly Notices of the Royal Astronomical*

Society, 391(1), 237-245.

Jacobson, R., Antreasian, P., Bordi, J., Criddle, K., Ionasescu, R., Jones, J., . . . Pelletier, F. (2006). The gravity field of the saturnian system from satellite observations and spacecraft tracking data. *The Astronomical Journal, 132*(6), 2520.

Jewitt, D., Chizmadia, L., Grimm, R., & Prialnik, D. (2007). Water in the small bodies of the solar system. *Protostars and Planets V, 1*, 863-878.

Jones, A. P., Price, G. D., Price, N. J., DeCarli, P. S., & Clegg, R. A. (2002). Impact induced melting and the development of large igneous provinces. *Earth and Planetary Science Letters, 202*(3), 551-561.

Kaltenegger, L., & Sasselov, D. (2009). Detecting planetary geochemical cycles on exoplanets: Atmospheric signatures and the case of SO2. *The Astrophysical Journal, 708*(2), 1162.

Kargel, J. S., Kaye, J. Z., Head, J. W., Marion, G. M., Sassen, R., Crowley, J. K., . . . Hogenboom,

D. L. (2000). Europa's crust and ocean: Origin, composition, and the prospects for life. *Icarus, 148*(1), 226-265.

Kasting, J. F., & Catling, D. (2003). Evolution of a habitable planet. *Annual Review of Astronomy and Astrophysics, 41*(1), 429-463.

Kelley, D. S., Karson, J. A., Blackman, D. K., FruÈh-Green, G. L., Butterfield, D. A., Lilley, M. D.,. . . Lebon, G. T. (2001). An off-axis hydrothermal vent field near the mid-atlantic ridge at 30 N. *Nature, 412*(6843), 145-149.

Kelley, D. S., Karson, J. A., Blackman, D. K., FruÈh-Green, G. L., Butterfield, D. A., Lilley, M. D.,. . . Lebon, G. T. (2001). An off-axis hydrothermal vent field near the mid-atlantic ridge at 30 N. *Nature, 412*(6843), 145-149.

Kelley, D. S., Karson, J. A., Fruh-Green, G. L., Yoerger, D. R., Shank, T. M., Butterfield, D. A., . .. Sylva, S. P. (2005). A serpentinite-hosted ecosystem: The lost city hydrothermal field. *Science (New York, N.Y.), 307*(5714), 1428-1434. doi:307/5714/1428 [pii]

Kirsimäe, K., Suuroja, S., Kirs, J., Kärki, A., Polikarpus, M., Puura, V., & Suuroja, K. (2002). Hornblende alteration and fluid inclusions in kärdla impact crater, estonia-evidence for impact-induced hydrothermal activity. *Meteoritics and Planetary Science, 37*, 449-457.

Koeppen, W. C., & Hamilton, V. E. (2008). Global distribution, composition, and abundance of olivine on the surface of mars from thermal infrared data. *Journal of Geophysical Research: Planets, 113*(E5)

Kuchner, M. J. (2003). Volatile-rich earth-mass planets in the habitable zone. *The Astrophysical Journal Letters, 596*(1), L105.

Lang, S. Q., Butterfield, D. A., Schulte, M., Kelley, D. S., & Lilley, M. D. (2010). Elevated concentrations of formate, acetate and dissolved organic carbon found at the lost city hydrothermal field. *Geochimica Et Cosmochimica Acta, 74*(3), 941-952.

Lineweaver, C. H., & Chopra, A. (2012). The habitability of our earth and other earths: Astrophysical, geochemical, geophysical, and biological limits on planet habitability. *Annual Review of Earth and Planetary Sciences, 40*(1), 597.

Lodders, K. (2003). Solar system abundances and condensation temperatures of the elements. *The Astrophysical Journal, 591*(2), 1220.

Lodders, K. (2003). Solar system abundances and condensation temperatures of the elements. *The Astrophysical Journal, 591*(2), 1220.

Longhi, J., Knittle, E., Holloway, J. R., & Waenke, H. (1992). The bulk composition, mineralogy and internal structure of mars. *Mars, 1*, 184-208.

Lowell, R., & Rona, P. (2002). Seafloor hydrothermal systems driven by the serpentinization of peridotite. *Geophysical Research Letters, 29*(11)

Lowenstein, T. K., Timofeeff, M. N., Brennan, S. T., Hardie, L. A., & Demicco, R. V. (2001). Oscillations in Phanerozoic seawater chemistry: Evidence from fluid inclusions. *Science*, 294(5544), 1086-1088.

Malamud, U., & Prialnik, D. (2016). A 1-D evolutionary model for icy satellites, applied to enceladus. *Icarus, 268*, 1-11.

Malvoisin, B., Brunet, F., Carlut, J., Rouméjon, S., & Cannat, M. (2012). Serpentinization of oceanic peridotites: 2. kinetics and processes of san carlos olivine hydrothermal alteration. *Journal of Geophysical Research: Solid Earth, 117*(B4)

Matson, D. L., Castillo, J. C., Lunine, J., & Johnson, T. V. (2007). Enceladus' plume: Compositional evidence for a hot interior. *Icarus, 187*(2), 569-573.

McCollom, T. M., Klein, F., Robbins, M., Moskowitz, B., Berquó, T. S., Jöns, N., . . . Templeton, A. (2016). Temperature trends for reaction rates, hydrogen generation, and partitioning of iron during experimental serpentinization of olivine. *Geochimica Et Cosmochimica* ***Acta, 181, 175-200.***

McCollom, T. M., & Seewald, J. S. (2001). A reassessment of the potential for reduction of dissolved CO2 to hydrocarbons during serpentinization of olivine. *Geochimica Et Cosmochimica Acta, 65*(21), 3769-3778.

McCord, T. B., Clark, R. N., Hawke, B., McFadden, L. A., Owensby, P., Pieters, C. M., & Adams, **J. B. (1981). Moon: Near-infrared spectral reflectance, a first good look. *Journal of Geophysical Research: Solid Earth, 86*(B11), 10883-10892.**

McKay, C. P. (2015). Habitability in the solar system and on extrasolar planets and moons.

McLaughlin, R., Sliter, W., Sorg, D., Russell, P., & Sarna□Wojcicki, A. (1996). Large□scale right□ slip displacement on the east san francisco bay region fault system, california: Implications for location of late miocene to pliocene pacific plate boundary. *Tectonics, 15*(1), 1-18.

McLaughlin, R. J. (1981). Tectonic setting of pre-tertiary rocks and its relation to geothermal resources in the geysers-clear lake area. *US Geol.Surv.Prof.Pap, 1141*, 3-23.

Michalski, J. R., Cuadros, J., Niles, P. B., Parnell, J., Rogers, A. D., & Wright, S. P. (2013). Groundwater activity on mars and implications for a deep biosphere. *Nature Geoscience, 6*(2), 133-138.

Michalski, J. R., & Niles, P. B. (2010). Deep crustal carbonate rocks exposed by meteor impact on mars. *Nature Geoscience, 3*(11), 751-755.

Moody, J. B. (1976). Serpentinization: a review. Lithos, 9(2), 125-138.

Moore, J. M., Howard, A. D., Dietrich, W. E., & Schenk, P. M. (2003). Martian layered fluvial deposits: Implications for noachian climate scenarios. *Geophysical Research Letters, 30*(24)

Morbidelli, A., Lunine, J., O'Brien, D., Raymond, S., & Walsh, K. (2012). Building terrestrial planets. *Annual Review of Earth and Planetary Sciences, 40*, 251-275.

Morbidelli, A., Lunine, J. I., Obrien, D. P., Raymond, S. N., & Walsh, K. J. (2012). Building terrestrial planets. *ArXiv Preprint arXiv:1208.4694,*

Müntener, O. (2010). Serpentine and serpentinization: A link between planet formation and life. *Geology, 38*(10), 959-960.

Nathues, A., Hoffmann, M., Cloutis, E. A., Schäfer, M., Reddy, V., Christensen, U., . . . Mengel, K. (2014). Detection of serpentine in exogenic carbonaceous chondrite material on vesta from dawn FC data. *Icarus, 239*, 222-237.

Nie, J., King, J. W., & Fang, X. (2008). Link between benthic oxygen isotopes and magnetic susceptibility in the red□clay sequence on the chinese loess plateau. *Geophysical Research Letters, 35*(3)

Niemann, H., Atreya, S., Bauer, S., Carignan, G., Demick, J., Frost, R., . . . Hunten, D. (2005). The abundances of constituents of titan's atmosphere from the GCMS instrument on the huygens probe. *Nature, 438*(7069), 779-784.

Nimmo, F., & Pappalardo, R. (2016). Ocean worlds in the outer solar system. *Journal of Geophysical Research: Planets, 121*(8), 1378-1399.

Nimmo, F., & Pappalardo, R. T. (2006). Diapir-induced reorientation of saturn's moon enceladus. *Nature, 441*(7093), 614-616.

Noack, L., & Breuer, D. (2014). Plate tectonics on rocky exoplanets: Influence of initial conditions and mantle rheology. *Planetary and Space Science, 98*, 41-49.

Ohara, Y., Stern, R. J., Ishii, T., Yurimoto, H., & Yamazaki, T. (2002). Peridotites from the mariana trough: First look at the mantle beneath an active back-arc basin. *Contributions to Mineralogy and Petrology, 143*(1), 1-18.

Oze, C., & Sharma, M. (2005). Have olivine, will gas: Serpentinization and the abiogenic production of methane on mars. *Geophysical Research Letters, 32*(10)

Page, N. J. (1976). Serpentinization and alteration in an olivine cumulate from the stillwater complex, southwestern montana. *Contributions to Mineralogy and Petrology, 54*(2), 127- 137.

Paukert, A. N., Matter, J. M., Kelemen, P. B., Shock, E. L., & Havig, J. R. (2012). Reaction path modeling of enhanced in situ CO 2 mineralization for carbon sequestration in the peridotite of the samail ophiolite, sultanate of oman. *Chemical Geology, 330*, 86-100.

Pearce, J. A., Lippard, S., & Roberts, S. (1984). Characteristics and tectonic significance of supra- subduction zone ophiolites. *Geological Society, London, Special Publications, 16*(1), 77-94.

Pirajno, F. (2009). Hydrothermal processes associated with meteorite impacts. *Hydrothermal processes and mineral systems* (pp. 1097-1130) Springer.

Porco, C. C., Helfenstein, P., Thomas, P. C., Ingersoll, A. P., Wisdom, J., West, R., . . . Squyres, S. (2006). Cassini observes the active south pole of enceladus. *Science (New York, N.Y.), 311*(5766), 1393-1401. doi:311/5766/1393 [pii]

Postberg, F., Kempf, S., Schmidt, J., Brilliantov, N., Beinsen, A., Abel, B., . . . Srama, R. (2009). Sodium salts in E-ring ice grains from an ocean below the surface of enceladus. *Nature, 459*(7250), 1098-1101.

Preston, L. J., & Dartnell, L. R. (2014). Planetary habitability: Lessons learned from terrestrial analogues. *International Journal of Astrobiology, 13*(01), 81-98.

Proskurowski, G., Lilley, M. D., Kelley, D. S., & Olson, E. J. (2006). Low temperature volatile production at the lost city hydrothermal field, evidence from a hydrogen stable isotope geothermometer. *Chemical Geology, 229*(4), 331-343.

Proskurowski, G., Lilley, M. D., Seewald, J. S., Fruh-Green, G. L., Olson, E. J., Lupton, J. E., . . .Kelley, D. S. (2008). Abiogenic hydrocarbon production at lost city hydrothermal field. *Science (New York, N.Y.), 319*(5863), 604-607. doi:10.1126/science.1151194 [doi]

Quesnel, Y., Sotin, C., Langlais, B., Costin, S., Mandea, M., Gottschalk, M., & Dyment, J. (2009). Serpentinization of the martian crust during noachian. *Earth and Planetary Science Letters, 277*(1), 184-193.

Quick, L. C., & Marsh, B. D. (2015). Constraining the thickness of Europa's water–ice shell: Insights from tidal dissipation and conductive cooling. *Icarus, 253*, 16-24.

Raymond, S. N., O'Brien, D. P., Morbidelli, A., & Kaib, N. A. (2009). Building the terrestrial planets: Constrained accretion in the inner solar system. *Icarus, 203*(2), 644-662.

Raymond, S. N., Quinn, T., & Lunine, J. I. (2004). Making other earths: Dynamical simulations of terrestrial planet formation and water delivery. *Icarus, 168*(1), 1-17.

Righter, K., & O'Brien, D. P. (2011). Terrestrial planet formation. *Proceedings of the National Academy of Sciences of the United States of America, 108*(48), 19165-19170. doi:10.1073/pnas.1013480108 [doi]

Rivoldini, A., Van Hoolst, T., Verhoeven, O., Mocquet, A., & Dehant, V. (2011). Geodesy constraints on the interior structure and composition of mars. *Icarus, 213*(2), 451-472.

Roatsch, T., Jaumann, R., Stephan, K., & Thomas, P. (2009). Cartographic mapping of the icy satellites using ISS and VIMS data. *Saturn from cassini-huygens* (pp. 763-781) Springer.

Robuchon, G., & Nimmo, F. (2011). Thermal evolution of pluto and implications for surface tectonics and a subsurface ocean. *Icarus, 216*(2), 426-439.

Rubie, D. C., Jacobson, S. A., Morbidelli, A., O'Brien, D. P., Young, E. D., de Vries, J., . . . Frost, D. (2015). Accretion and differentiation of the terrestrial planets

with implications for the compositions of early-formed solar system bodies and accretion of water. *Icarus, 248*, 89- 108.

Rubin, A. E. (1990). Kamacite and olivine in ordinary chondrites: Intergroup and intragroup relationships. *Geochimica Et Cosmochimica Acta, 54*(5), 1217-1232.

Russell, M. J., Barge, L. M., Bhartia, R., Bocanegra, D., Bracher, P. J., Branscomb, E., Nitschke, W. (2014). The drive to life on wet and icy worlds. *Astrobiology, 14*(4), 308-343.

Russell, M., Hall, A., & Martin, W. (2010). Serpentinization as a source of energy at the origin of life. *Geobiology, 8*(5), 355-371.

Rytuba, J. J. (1993). Epithermal precious-metal and mercury deposits in the sonoma and clear lake volcanic fields, california. *Active Geothermal Systems and Gold-Mercury Deposits in the Sonoma-Clear Lake Volcanic Fields, California: Society of Economic Geologists, Guidebook Series, 16*, 38-51.

Saur, J., Feldman, P. D., Roth, L., Nimmo, F., Strobel, D. F., Retherford, K. D., ... & Grodent, D. (2011). Hubble space telescope/advanced camera for surveys observations of Europa's atmospheric ultraviolet emission at eastern elongation. *The Astrophysical Journal*, 738(2), 153.

Pappalardo, R. T. (2008). Evidence for temporal variability of enceladus' gas jets: Modeling of cassini observations. *Geophysical Research Letters, 35*(20)

Savov, I. P., Ryan, J. G., D'Antonio, M., & Fryer, P. (2007). Shallow slab fluid release across and along the mariana arc□basin system: Insights from

geochemistry of serpentinized peridotites from the mariana fore arc. *Journal of Geophysical Research: Solid Earth, 112*(B9)

Scambelluri, M., Fiebig, J., Malaspina, N., Müntener, O., & Pettke, T. (2004). Serpentinite subduction: Implications for fluid processes and trace-element recycling. *International Geology Review, 46*(7), 595-613.

Schaller, E. L., & Brown, M. (2007). Volatile loss and retention on kuiper belt objects. *The Astrophysical Journal Letters, 659*(1), L61.

Schirmack, J., Alawi, M., & Wagner, D. (2015). Influence of martian regolith analogs on the activity and growth of methanogenic archaea, with special regard to long-term desiccation. *Frontiers in Microbiology, 6*, 210.

Schirmack, J., Böhm, M., Brauer, C., Löhmannsröben, H., de Vera, J., Möhlmann, D., & Wagner, D. (2014). Laser spectroscopic real time measurements of methanogenic activity under simulated martian subsurface analog conditions. *Planetary and Space Science, 98*, 198-204.

Schrenk, M. O., Brazelton, W. J., & Lang, S. Q. (2013). Serpentinization, carbon, and deep life. *Rev Mineral Geochem, 75*(1), 575-606.

Schulte, M., Blake, D., Hoehler, T., & McCOLLOM, T. (2006). Serpentinization and its implications for life on the early earth and mars. *Astrobiology, 6*(2), 364-376.

Scott, T. J. (2014). Habitability of ultrabasic, serpentinite-associated waters from coast range and philippines ophiolites.

Seager, S., Kuchner, M., Hier-Majumder, C., & Militzer, B. (2007). Mass-radius relationships for solid exoplanets. *The Astrophysical Journal, 669*(2), 1279.

Sekine, Y., Shibuya, T., Postberg, F., Hsu, H., Suzuki, K., Masaki, Y., . . . Yoshizaki, M. (2015). High-temperature water-rock interactions and hydrothermal environments in the chondrite- like core of enceladus. *Nature Communications, 6*

Selsis, F., Kaltenegger, L., & Paillet, J. (2008). Terrestrial exoplanets: Diversity, habitability and characterization. *Physica Scripta, 2008*(T130), 014032.

Shervais, J. W. (2001). Birth, death, and resurrection: The life cycle of suprasubduction zone ophiolites. *Geochemistry, Geophysics, Geosystems, 2*(1)

Shervais, J. W., & Kimbrough, D. L. (1985). Geochemical evidence for the tectonic setting of the coast range ophiolite: A composite island arc–oceanic crust terrane in western california. *Geology, 13*(1), 35-38.

Shervais, J. W., Kimbrough, D. L., Renne, P., Hanan, B. B., Murchey, B., Snow, C. A., . . . Beaman, J. (2004). Multi-stage origin of the coast range ophiolite, california: Implications for the life cycle of supra-subduction zone ophiolites. *International Geology Review, 46*(4), 289-315.

Shock, E. L., & Schulte, M. D. (1998). Organic synthesis during fluid mixing in hydrothermal systems. *Journal of Geophysical Research: Planets, 103*(E12), 28513-28527.

Sleep, N. H., Bird, D. K., & Pope, E. C. (2011). Serpentinite and the dawn of life. *Philosophical Transactions of the Royal Society of London.Series B, Biological Sciences, 366*(1580), 2857-2869. doi:10.1098/rstb.2011.0129 [doi]

Sleep, N. H., Meibom, A., Fridriksson, T., Coleman, R. G., & Bird, D. K. (2004). H2-rich fluids from serpentinization: Geochemical and biotic implications. *Proceedings of the National Academy of Sciences of the United States of America, 101*(35), 12818-12823. doi:10.1073/pnas.0405289101 [doi]

Sohl, F., Choukroun, M., Kargel, J., Kimura, J., Pappalardo, R., Vance, S., & Zolotov, M. (2010). Subsurface water oceans on icy satellites: Chemical composition and exchange processes. *Space Science Reviews, 153*(1-4), 485-510.

Sohl, F., Schubert, G., & Spohn, T. (2005). Geophysical constraints on the composition and structure of the martian interior. *Journal of Geophysical Research: Planets, 110*(E12)

Spencer, J. R., Pearl, J. C., Segura, M., Flasar, F. M., Mamoutkine, A., Romani, P., . . . Lopes, R.M. (2006). Cassini encounters enceladus: Background and the discovery of a south polar hot spot. *Science (New York, N.Y.), 311*(5766), 1401-1405. doi:311/5766/1401 [pii]

Stern, R. J., Bloomer, S. H., Martinez, F., Yamazaki, T., & Harrison, T. M. (1996). The composition of back□arc basin lower crust and upper mantle in the mariana trough: A first report. *Island Arc, 5*(3), 354-372.

Stesky, R., & Brace, W. (1973). Electrical conductivity of serpentinized rocks to 6 kilobars. *Journal of Geophysical Research, 78*(32), 7614-7621.

Szponar, N., Brazelton, W. J., Schrenk, M. O., Bower, D. M., Steele, A., & Morrill, P. L. (2013). Geochemistry of a continental site of serpentinization, the tablelands ophiolite, gros morne national park: A mars analogue. *Icarus, 224*(2), 286-296.

Suzuki, S., Ishii, S. I., Wu, A., Cheung, A., Tenney, A., Wanger, G., ... & Nealson, K. H. (2013). Microbial diversity in The Cedars, an ultrabasic, ultrareducing, and low salinity serpentinizing ecosystem. *Proceedings of the National Academy of Sciences*, 201302426.

Tackley, P. J., Ammann, M., Brodholt, J. P., Dobson, D. P., & Valencia, D. (2013). Mantle dynamics in super-earths: Post-perovskite rheology and self-regulation of viscosity. *Icarus, 225*(1), 50-61.

Takir, D., Emery, J. P., Mcsween, H. Y., Hibbitts, C. A., Clark, R. N., Pearson, N., & Wang, A. (2013). Nature and degree of aqueous alteration in CM and CI **carbonaceou**s chondrites. *Meteoritics & Planetary Science, 48*(9), 1618-1637.

Taubner, R., Leitner, J., Firneis, M., & Hitzenberger, R. (2016). Modelling the interior structure of enceladus based on the 2014's cassini gravity data. *Origins of Life and Evolution of Biospheres, 46*(2-3), 283-288.

Taylor, G. J., Martel, L. M., Karunatillake, S., Gasnault, O., & Boynton, W. V. (2010). Mapping mars geochemically. *Geology, 38*(2), 183-186.

Teir, S., Revitzer, H., Eloneva, S., Fogelholm, C., & Zevenhoven, R. (2007). Dissolution of natural serpentinite in mineral and organic acids. *International Journal of Mineral*

Processing, 83(1), 36-46.

Thomas, P. (2010). Sizes, shapes, and derived properties of the saturnian satellites after the cassini nominal mission. *Icarus, 208*(1), 395-401.

Toft, P. B., Arkani-Hamed, J., & Haggerty, S. E. (1990). The effects of serpentinization on density and magnetic susceptibility: A petrophysical model. *Physics of the Earth and Planetary Interiors, 65*(1-2), 137-157.

Tomeoka, K., & Buseck, P. R. (1988). Matrix mineralogy of the orgueil CI carbonaceous chondrite. *Geochimica Et Cosmochimica Acta, 52*(6), 1627-1640.

Travis, B., Palguta, J., & Schubert, G. (2012). A whole-moon thermal history model of europa: Impact of hydrothermal circulation and salt transport. *Icarus, 218*(2), 1006-1019.

Turner, S., Bridges, J., Grebby, S., & Ehlmann, B. (2015). Hydrothermal minerals within impact craters in amazonian-aged terrains on mars. Paper presented at the *Lunar and Planetary Science Conference, , 46* 2061.

Turner, S. M., Bridges, J. C., Grebby, S., & Ehlmann, B. L. (2016). Hydrothermal activity recorded in post Noachian□aged impact craters on mars. *Journal of Geophysical Research:Planets, 121*(4), 608-625.

Valencia, D., O'Connell, R. J., & Sasselov, D. (2006). Internal structure of massive terrestrial planets. *Icarus, 181*(2), 545-554.

van Boekel, R., Min, M., Leinert, C., Waters, L., Richichi, A., Chesneau, O., . . . Graser, U. (2004).The building blocks of planets within the 'terrestrial'region of protoplanetary disks. *Nature, 432*(7016), 479-482.

Van Hoolst, T., Baland, R., & Trinh, A. (2016). The diurnal libration and interior structure of enceladus. *Icarus, 277*, 311-318.

Vance, S., Hand, K., & Pappalardo, R. (2016). Geophysical controls of chemical disequilibria in europa. *Geophysical Research Letters,*

Vance, S., Bouffard, M., Choukroun, M., & Sotin, C. (2014). Ganymede′ s internal structure including thermodynamics of magnesium sulfate oceans in contact with ice. *Planetary and Space Science, 96*, 62-70.

Vance, S., & Brown, J. M. (2013). Thermodynamic properties of aqueous MgSO 4 to 800MPa at temperatures from− 20 to 100° C and concentrations to 2.5 molkg− 1 from sound speeds, with applications to icy world oceans. *Geochimica Et Cosmochimica Acta, 110*, 176-189.

Vance, S., Harnmeijer, J., Kimura, J., Hussmann, H., DeMartin, B., & Brown, J. M. (2007).Hydrothermal systems in small ocean planets. *Astrobiology, 7*(6), 987-1005.

Volcanism, B. (1981). Basaltic volcanism on the terrestrial planets. *Peragamon.New York, 1286*

Wagner, F., Tosi, N., Sohl, F., Rauer, H., & Spohn, T. (2012). Rocky super-earth interiors-structure and internal dynamics of CoRoT-7b and kepler-10b. *Astronomy & Astrophysics, 541*, A103.

Waite Jr, J. H., Lewis, W., Magee, B., Lunine, J., McKinnon, W., Glein, C., . . . Westlake, J. (2009). Liquid water on enceladus from observations of ammonia and 40Ar in the plume. *Nature, 460*(7254), 487-490.

Waite, J. H.,Jr, Combi, M. R., Ip, W. H., Cravens, T. E., McNutt, R. L.,Jr, Kasprzak, W., . . . Tseng, W. L. (2006). Cassini ion and neutral mass spectrometer: Enceladus plume composition and structure. *Science (New York, N.Y.), 311*(5766), 1419-1422. doi:311/5766/1419 [pii]

Wang, Y., Wen, L., & Weidner, D. J. (2013). Composition of mars constrained using geophysical observations and mineral physics modeling. *Physics of the Earth and Planetary Interiors, 224*, 68-76.

Wang, D. T., Gruen, D. S., Lollar, B. S., Hinrichs, K. U., Stewart, L. C., Holden, J. F., . . . Ono, S. (2015). Methane cycling. nonequilibrium clumped isotope signals in microbial methane. *Science (New York, N.Y.), 348*(6233), 428-431. doi:10.1126/science.aaa4326 [doi]

Weiss, L. M., & Marcy, G. W. (2014). The mass-radius relation for 65 exoplanets smaller than 4 earth radii. *The Astrophysical Journal Letters, 783*(1), L6.

Wordsworth, R. D., Forget, F., Selsis, F., Millour, E., Charnay, B., & Madeleine, J. (2011). Gliese 581d is the first discovered terrestrial-mass exoplanet in the habitable zone. *The Astrophysical Journal Letters, 733*(2), L48.

Wunder, B., Wirth, R., & Gottschalk, M. (2001). Antigorite: Pressure and temperature dependence of polysomatism and water content. *European Journal of Mineralogy, 13*(3), 485-495.

Yellappa, T., Chetty, T., Tsunogae, T., & Santosh, M. (2010). The manamedu complex: Geochemical constraints on neoproterozoic suprasubduction zone ophiolite formation within the gondwana suture in southern india. *Journal of Geodynamics, 50*(3), 268-285.

Young, G. M. (2013). Precambrian supercontinents, glaciations, atmospheric oxygenation, metazoan evolution and an impact that may have changed the second half of earth history. *Geoscience Frontiers, 4*(3), 247-261.

Yu, Z., Robinson, P., & McGoldrick, P. (2001). An evaluation of methods for the chemical decomposition of geological materials for trace element determination using ICP□MS. *Geostandards Newsletter, 25*(2□3), 199-217.

Zolotov, M. Y. (2007). An oceanic composition on early and today's enceladus. *Geophysical Research Letters, 34*(23)

Zsom, A., Seager, S., De Wit, J., & Stamenković, V. (2013). Toward the minimum inner edge distance of the habitable zone. *The Astrophysical Journal, 778*(2), 109.